ELEVATED MOIST LAYERS – EXPLORING A BLINDSPOT IN THE GLOBAL SATELLITE OBSERVING SYSTEM

Dissertation
with the aim of achieving a doctoral degree
at the Faculty of Mathematics, Informatics and
Natural Sciences Department of Earth Sciences
at Universität Hamburg

Submitted by

Marc Prange
Hamburg, 2022

Department of Earth Sciences

Date of Oral Defense:

Reviewers:

Members of the Examination Commission:

Prof. Dr. Stefan A. Buehler
Dr. Manfred Brath
Prof. Dr. Bjorn Stevens
Prof. Dr. Eleanor Frajka-Williams
Prof. Dr. Lars Kutzbach

Chair of the Subject Doctoral Comittee
Earth System Sciences:

Prof. Dr. Hermann Held

Dean of the Faculty MIN:

Prof. Dr.-Ing. Norbert Ritter

ABSTRACT

I investigate the capability of passive infrared (IR) satellite observations to resolve elevated moist layers (EMLs), which denote significant mid-tropospheric anomalies of water vapor in the tropics. EMLs are thought to emerge from melting-level detrainment of moist air from deep convective cells. They can span over several 100 km around the convective cell's usually dry environment, significantly altering the spatial structure of radiative heating, which may have implications on convective aggregation and climate feedbacks. Up to now, there have only been some measurement campaign based case studies dedicated to EMLs, leaving many unknowns about frequency of occurence and variability in strength, spatial extend or lifetime. Passive satellite observations of hyperspectral IR instruments used to retrieve vertical profiles of water vapor globally on a 12 km resolution may contribute towards closing these knowledge gaps about EMLs. However, the starting point of my work is defined by the findings of Stevens et al. (2017), which suggest fundamental limitations in the ability of passive satellite observations to resolve EMLs.

In a first study, I setup a model-based retrieval based on simulated satellite observations to reproduce the results of the EML case study of Stevens et al. (2017) to understand what may cause the apparent EML blindspot and find a way to resolve it. When running the retrieval with a similar configuration as Stevens et al. (2017) I am able to reproduce the absence of the EML in the retrieved humidity profile. I find that errors in the retrieved water vapor profile correlate with errors in the retrieved temperature profile in a way that they cancel out radiatively in the water vapor band, making the EML difficult to detect in the satellite observation. However, by extending the used spectral ranges to a broader range of channels sensitive to water vapor and by adding independent temperature information from channels sensitive to CO_2, I find that errors in both temperature and water vapor retrievals can be reduced and the EML can be resolved well. I conclude that EMLs do not denote an inherent blindspot for passive satellite observations.

To more quantitatively assess the ability of satellite retrievals to resolve EMLs, I introduce a new method for identifying EMLs and characterising them in terms of strength, vertical thickness and height. When applying the method to results of my model-based retrieval run on 1288 tropical ocean atmospheres, I find that it captures about 80 % as many EMLs as the reference data and underestimates EML strength by 17 % and EML thickness by 15 %. This indicates a good capability of the retrieval to resolve EMLs, but should rather be viewed

as an upper bound of what is possible to resolve when using real satellite observations.

In a second study, I evaluate the ability of two operational satellite retrieval products based on hyper-spectral IR observations of the IASI (Infrared Atmospheric Sounding Interferometer) and AIRS (Atmospheric Infrared Sounder) instruments. In addition, I evaluate the ability ERA5 reanalysis data to capture EMLs. I do so by collocating the three datasets within 50 km in space and 30 minutes in time with 2146 radiosondes launched over the course of 4 years on Manus Island in the Western Pacific warm pool, a region where EMLs occur particularly often. By applying the method introduced in my first study, I find that ERA5 captures the EMLs most reliably among the investigated datasets, showing no significant biases in EML characteristics when smoothing the radiosonde humidity profiles by a 1 km moving average. The IASI and AIRS retrievals capture 79 % and 92 % as many EMLs as collocated ERA5 data, respectively, indicating slightly worse but also a generally good reliability in capturing EMLs. The IASI retrieval shows strongest smoothing among the investigated datasets with EML thickness being overestimated by about 82 % compared to collocated radiosonde data. The AIRS retrieval underestimates EML height by on average 1.3 km, which I hypothesize to be caused by a technical issue in the vertical coordinate assignment of the retrieval data.

Finally, I quantify the usefulness of the different operational data products to investigate the effect of EMLs on radative heating rates and associated radiatively driven subsidence. Firstly, I find based on the radiosonde reference data that EML associated subsidence is on the order of 2.6 hPa hour^{-1}, which is significant compared to mean meso-scale subsidence rates on the order of 1 hPa hour^{-1} observed during the EUREC4A field campaign. ERA5 and IASI retrievals underestimate EML associated subsidence by 39 % and AIRS retrievals by about 80 %, indicating limited usefulness of these datasets to asses the dynamical impact of EMLs. However, my overall findings yield the conclusion that operational satellite and reanalysis products are already useful for illuminating some of the unknowns about EMLs and motivate further research on the dynamical role of EMLs in their meso-scale environment in the future.

ZUSAMMENFASSUNG

Ich untersuche die Fähigkeit von passiven infrarot (IR) Satellitenbeobachtungen, gehobene Schichten erhöhter Feuchte (EMLs) aufzulösen, die signifikante mitteltroposphärische Anomalien des Wasserdampfs in den Tropen darstellen. Man nimmt an, dass EMLs durch das Ausscheren feuchter Luft aus hohen konvektiven Zellen in der Höhe des Schmelzpunktes entstehen. Sie können sich über mehrere 100 km um die normalerweise trockene Umgebung der konvektiven Zelle erstrecken und die räumliche Struktur der Strahlungserwärmung erheblich verändern, was Auswirkungen auf Aggregation von Konvektion un Klima-Rückkopplungen haben kann. Bisher gab es nur einige auf Messkampagnen basierende Fallstudien, die sich mit EMLs befassen, so dass viele Unbekannte über die Häufigkeit des Auftretens und die Variabilität in Stärke, räumlicher Ausdehnung oder Lebensdauer von EMLs bestehen. Passive Satellitenbeobachtungen mit hyperspektralen IR Instrumenten, welche global vertikale Profile des Wasserdampfs bei einer räumlichen Auflösung von 12 km messen, könnten dazu beitragen, diese Wissenslücken über EMLs zu schließen. Der Ausgangspunkt meiner Arbeit liegt in den Ergebnissen von Stevens et al. (2017), die auf grundlegende Einschränkungen bei der Fähigkeit passiver Satellitenbeobachtungen, EMLs aufzulösen, hindeuten.

In einer ersten Studie habe ich ein modellbasiertes retrieval auf der Grundlage simulierter Satellitenbeobachtungen aufgesetzt, um die Ergebnisse der EML-Fallstudie von Stevens et al. (2017) zu verstehen und eine Ursache für den vermeintlichen blinden Fleck gegenüber EMLs zu finden und falls möglich eine Lösung. Wenn ich das retrieval mit einer ähnlichen Konfiguration wie Stevens et al. (2017) durchführe, bin ich in der Lage, das Fehlen der EML im Feuchteprofil des retrievals zu reproduzieren. Ich stelle fest, dass Fehler im Wasserdampfprofil des retrievals mit Fehlern im Temperaturprofil des retrievals so korrelieren, dass sie sich in der Strahlung in der Wasserdampfbande ausgleichen und die EML in der Satellitenbeobachtung schwer zu erkennen ist. Durch die Ausweitung der verwendeten Spektralbereiche auf weitere Wasserdampf empfindliche Kanäle und durch Hinzufügen unabhängiger Temperaturinformationen aus CO_2 empfindlichen Kanälen, stelle ich fest, dass die Fehler im retrieval von Temperatur und Wasserdampf reduziert werden und die EML gut aufgelöst werden kann. Ich schließe daraus, dass EMLs keinen grundlegenden blinden Fleck für passive Satellitenbeobachtungen darstellen.

Um die Fähigkeit von Satellitenmessungen, EMLs aufzulösen, quantitativer zu untersuchen, führe ich eine neue Methode zur Identifizierung und Charakterisierung von EMLs in Bezug auf Stärke, vertikale Dicke und Höhe ein. Bei der Anwendung der Methode auf die

Ergebnisse meines modellbasierten retrievals für 1288 Atmosphären über tropischen Ozeanen stelle ich fest, dass das retrieval etwa 80 % so viele EMLs erfasst wie die Referenzdaten und die EML Stärke um 17 % und die EML Dicke um 15 % unterschätzt. Dies deutet auf eine gute Fähigkeit des retrievals hin, EMLs aufzulösen. Die Ergebnisse sollten aber eher als Obergrenze dessen angesehen werden, was bei der Verwendung echter Satellitenbeobachtungen möglich ist.

In einer zweiten Studie untersuche ich die Fähigkeit zweier operationeller Satelliten retrievals, die auf hyperspektralen IR Beobachtungen der Instrumente IASI (Infrared Atmospheric Sounding Interferometer) und AIRS (Atmospheric Infrared Sounder) basieren. Darüber hinaus bewerte ich die Fähigkeit der ERA5-Reanalyse, EMLs zu erfassen. Dazu vergleiche ich die drei Datensätze in einem Abstand von 50 km im Raum und 30 Minuten in der Zeit mit 2146 Radiosonden, die im Laufe von vier Jahren auf der Insel Manus im Westpazifik gestartet wurden, einer Region, in der EMLs besonders häufig auftreten. Durch Anwendung der in meiner ersten Studie vorgestellten Methode stelle ich fest, dass ERA5 die EMLs unter den untersuchten Datensätzen am zuverlässigsten erfasst und keine signifikanten Abweichungen der EML Eigenschaften zeigt, wenn die Feuchte Profile der Radiosonden durch einen gleitenden 1 km Mittelwert geglättet werden. Die IASI und AIRS retrievals erfassen jeweils 79 % bzw. 92 % so viele EMLs wie die kollokierten ERA5 Daten, was auf eine etwas schlechtere, aber auch allgemein gute Zuverlässigkeit bei der Erfassung von EMLs hindeutet. Das IASI retrieval zeigt die stärkste Glättung unter den untersuchten Datensätzen, wobei die EML Dicke im Vergleich zu kollokierten Radiosonden um etwa 82 % überschätzt wird. Das AIRS retrieval unterschätzt die EML Höhe um durchschnittlich 1,3 km, was meiner Hypothese nach auf ein technisches Problem bei der vertikalen Koordinatenzuweisung der retrieval Daten zurückzuführen ist.

Zuletzt quantifiziere ich die Nützlichkeit der verschiedenen operationellen Datenprodukte, um die Auswirkungen von EMLs auf die Strahlungsheizraten und das damit verbundene strahlungsbedingte Absinken von Luftmassen zu untersuchen. Zunächst stelle ich anhand der Radiosonden-Referenzdaten fest, dass das EML bedingte Absinken in der Größenordnung von 2,6 hPa Stunde^{-1} liegt, was im Vergleich zu Beobachtungen der mittleren mesoskaligen Vertikalgeschwindigkeiten während der EUREC4A Feldkampagne in der Größenordnung von 1 hPa Stunde^{-1} signifikant ist. ERA5 und IASI retrievals unterschätzen das EML assoziierte Absinken um 39 % und AIRS retrievals um etwa 80 %, was darauf hindeutet, dass diese Datensätze nur begrenzt geeignet sind, um die dynamischen Auswirkungen von EMLs zu beurteilen. Meine Gesamtergebnisse lassen jedoch den Schluss zu, dass operationelle Satelliten- und Reanalyseprodukte bereits nützlich sind, um einige der Unbekannten über EMLs zu beleuchten,

und motivieren weitere Forschung zur Rolle von EMLs für die Dynamik in ihrer mesoskaligen Umgebung.

PUBLICATIONS

In this section, I give an overview of the scientific publications I was involved in as first author or co-author during the time of my PhD.

FIRST AUTHOR

During my PhD, I produced the following publications as first author. They are included in the Appendices. Note that at the time of writing, the second study is still in review (Prange et al., 2022a).

Prange, Marc, Manfred Brath, and Stefan A. Buehler (2021). "Are elevated moist layers a blind spot for hyperspectral infrared sounders? A model study." In: *Atmospheric Measurement Techniques* 14.11, pp. 7025–7044. DOI: https://doi.org/10.5194/amt-14-7025-2021.

Prange, Marc, Stefan A. Buehler, and Manfred Brath (2022). "How adequately are elevated moist layers represented in reanalysis and satellite observations?" In: *Atmospheric Chemistry and Physics*. DOI: https://doi.org/10.5194/egusphere-2022-755.

MAJOR CONTRIBUTION

I applied the collocation procedure to all observational datasets and did the formal analysis of those datasets to produce all observation-based results presented in the study. I produced Figures 1, 2, 3 and 5 and wrote Sect. 6.

Buehler, Stefan A., Marc Prange, John Mrziglod, Viju O. John, Martin Burgdorf, and Oliver Lemke (2020). "Opportunistic Constant Target Matching—A New Method for Satellite Intercalibration." In: *Earth and Space Science* 7.5. DOI: 10.1029/2019EA000856.

I conducted the initial flight phase segmentation for the HALO research flights during EUREC^{4}A and led the following group efforts to produce a stand-alone flight segment dataset. The flight segment dataset is introduced by Konow et al. (2021a) and available on Zenodo (Prange et al., 2020).

Konow, Heike et al. (2021). "EUREC4A's HALO." In: *Earth System Science Data* 13.12, pp. 5545–5563. DOI: 10.5194/essd-13-5545-2021.

Prange, Marc, Max Ringel, Geet George, Lutz Hirsch, Tobias Kölling, Heike Konow, Theresa Lang, and Theresa Mieslinger (2020). "EUREC4A: HALO flight phase separation: Awesome Albatross." en. In: DOI: 10.5281/zenodo.3906507.

For calibration efforts of the HIRS satellite instrument using observations of the moon, I setup a procedure for finding moon intrusions in HIRS deep space view data and filtering methods to find the most relevant cases. I produced Fig. 1 for the publication of Burgdorf et al. (2020).

Burgdorf, Martin J., Thomas G. Müller, Stefan A. Buehler, Marc Prange, and Manfred Brath (2020). "Characterization of the High-Resolution Infrared Radiation Sounder Using Lunar Observations." In: *Remote Sensing* 12.9, p. 1488. DOI: https://doi.org/10.3390/rs12091488.

MINOR CONTRIBUTIONS

I participated in the EUREC^{4}A field campaign where I fulfilled several different tasks. I was responsible for launching dropsondes from the HALO aircraft during two research flights, conducted calibration procedures for the HAMP instrument onboard of HALO, helped with radiosonde launches on Barbados, took care of data distribution during the campaign, presented the weather bulletin for the on-site crew on one day and was involved in outreach activities for local schools on Barbados.

Stevens, B. et al. (2021). "EUREC^{4}A." In: *Earth System Science Data Discussions* 2021, pp. 1–78. DOI: 10.5194/essd-2021-18. URL: https://essd.copernicus.org/preprints/essd-2021-18/.

For my efforts of conducting the flight phase segmentation for HALO I had the pleasure of working closely with Geet George, who published the overview paper of the EUREC^{4}A dropsonde data (George et al., 2021a). In the paper, the flight segmentation data is used rigerously to provide a first overview of the dropsonde data and provide higher level products.

George, Geet et al. (2021). "JOANNE: Joint dropsonde Observations of the Atmosphere in tropical North atlaNtic meso-scale Environments." In: *Earth System Science Data* 13.11, pp. 5253–5272. DOI: 10.5194/essd-13-5253-2021.

For satellite calibration efforts of microwave instruments using the moon, I provided code to process meta-data that looks for deep space view observations where the satellite viewing direction was particularly close to the moon (Burgdorf et al., 2021).

Burgdorf, M. J., S. A. Buehler, and M. Prange (2021). "Calibration and Characterization of Satellite-Borne Microwave Sounders With the Moon." In: *Earth and Space Science* 8.7. DOI: 10.1029/2021EA001725.

For efforts to verify thermo-physical models of the brightness temperature of asteroids or minor bodies like the moon using satellite-based infrared observations of the HIRS instrument, I provided methods to find moon intrusions in the HIRS data. I produced Fig. 1 of the study of Müller et al. (2021).

Müller, T. G., M. Burgdorf, V. Ali-Lagoa, S. A. Buehler, and M. Prange (2021). "The Moon at thermal infrared wavelengths: a benchmark for asteroid thermal models." In: *Astronomy and Astrophysics* 650, A38. DOI: https://doi.org/10.1051/0004-6361/202039946.

ACKNOWLEDGEMENTS

I believe it is fair to say that the PhD for the most part is an individual project with the aim of developing the skills of conducting your own research. However, I learned that this does in no sense imply that one has to feel isolated - not even in COVID times - since you sit in the same boat with many peers and find a lot of people helping and cheering for you along the way.

I would like to thank my supervisor Stefan A. Bühler for shaping my scientific education from the start of my Bachelor Thesis to the end of my PhD. I am very grateful for the trust he gave me over these years and also the scientific support and encouragements when I needed it. I also want to thank my supervisor Manfred Brath for always being there as a first point of contact when I felt stuck on anything and being super approachable. Thank you also to Cathy Hohenegger for reliably and efficiently steering us through the panel meetings as panel chair, making sure that I am on track. I also want to thank my previous supervisor Martin Burgdorf, who guided my first scientific endeavors during my Bachelor and Master Thesis and is a joy to work with to date. I also want to thank Oliver Lemke for the friendliest and most patient technical guidance over the years I could imagine. I also want to thank our server thunder for staying alive over the course of 6 years of me processing buggy code and just now shutting down when I am at the finish line.

I would like to thank the UTH community, in particular Theresa Lang and Lukas Kluft, for focused scientific discussions about what shapes the humidity in the upper troposphere. Our rounds gave the early period of my PhD at least a bit more structure and actually felt like a good place for informal discussions about what the heck our results want to tell us. In the same sense I want to thank the RATM community, in particular Manfred Brath, Jon Petersen, Florian Römer and Lorena Kowalczyk for making Friday afternoons pass by a lot quicker.

I want to thank all my friends and family who backed me up over the last years with fun activities to get the mind in the right place when it was needed. This involved many park beers, climbing activities (indoor and outdoor), great hikes crossing entire islands, cycling and kayaking trips, some virtual game nights and more. In particular, I want to thank my parents and my brother Jan, who I know always has my back if it counts and who feels basically like a very good brother to me. I also want to thank my guitar teacher Bernhard, not only for the great guidance in my guitar endeavors, but also for his generally caring attitude and some extra hours of good

talks. Without everyone's reassurance and welcome distractions my path would have felt a lot more stony.

I am very thankful for the rich opportunities I was given in the limited time of no COVID restrictions to visit workshops, conferences and in particular the EUREC^{4}A measurement campaign. These events were always big boosts in motivation for my work and made me realize that being in science means being around open, friendly and genuinely interested people. Within this community it feels like no coincidence to find persons that have meaningful and positive impact in your life.

Talking about friendly and caring persons, I can not exclude the people working in the scientific administration, in particular at the offices of the IMPRS and the Meteorological Institute. Thank you for helping out with administrative issues and whatever the everyday office life confronts you with.

CONTENTS

I UNIFYING ESSAY 1

1 MOTIVATION 3

2 IS THERE A MOIST LAYER BLINDSPOT IN SATELLITE OBSERVATIONS? 7
- 2.1 Hyperspectral Infrared Observations . . . 7
- 2.2 Conceptualisation of the moist layer blindspot . . . 9
- 2.3 Demonstration of the moist layer blindspot and how to resolve it . . . 10

3 REPRESENTATION OF MOIST LAYERS IN OPERATIONAL RETRIEVAL PRODUCTS 14
- 3.1 Moist layers during EUREC^{4}A . . . 14
- 3.2 Moist layer reference dataset from Manus Island . . . 17
- 3.3 Moist layer identification and characterisation . . . 18
- 3.4 Comparison of moist layer characteristics . . . 20
- 3.5 Moist layers' effect on meso-scale dynamics . . . 21

4 SUMMARY AND CONCLUSION 24

II APPENDIX 27

A ARE ELEVATED MOIST LAYERS A BLIND SPOT FOR HYPERSPECTRAL INFRARED SOUNDERS? A MODEL STUDY 29
- A.1 Introduction . . . 32
  - A.1.1 Previous moist layer retrievals . . . 33
- A.2 The retrieval . . . 36
  - A.2.1 Spectral setup . . . 36
  - A.2.2 Retrieval quantities . . . 38
  - A.2.3 Optimal estimation algorithm . . . 38
  - A.2.4 The forward model and representation of IASI . 38
  - A.2.5 A priori assumptions . . . 39
- A.3 Definition and characterisation of moisture anomalies . 42
- A.4 Case study of a moist layer retrieval . . . 43
  - A.4.1 Importance of temperature information to retrieve a moist layer . . . 45
  - A.4.2 Retrieval resolution . . . 49
- A.5 Retrieval performance . . . 51
  - A.5.1 Reference dataset and retrieval error . . . 52
  - A.5.2 Smoothing error . . . 53
- A.6 Retrieval of moisture anomalies . . . 55
  - A.6.1 Moisture anomaly characteristics . . . 56
  - A.6.2 Implications of moisture anomalies for the heating rate profile . . . 57
- A.7 Summary and conclusions . . . 60
- A.8 Appendix . . . 63

A.8.1 Temperature averaging kernels 63
B HOW ADEQUATELY ARE ELEVATED MOIST LAYERS REPRESENTED IN REANALYSIS AND SATELLITE OBSERVATIONS? 65
B.1 Introduction 68
B.2 Data 69
B.2.1 GRUAN radiosondes 70
B.2.2 ERA5 71
B.2.3 IASI L2 Climate Data Record 71
B.2.4 CLIMCAPS-Aqua L2 product 72
B.2.5 Collocation procedure 73
B.3 Climatological mean 74
B.4 Moisture anomaly identification and characterisation . 77
B.5 Comparison of moisture anomaly characteristics 78
B.5.1 All-sky 79
B.5.2 Clear-sky 82
B.6 Moist layers' radiative implications on the dynamics . 84
BIBLIOGRAPHY 91

Part I

UNIFYING ESSAY

In this essay I first motivate my specific research questions by introducing their scientific background and context in current literature. I then summarize the main contents of my two studies in terms of specific scientific motivation, methods and results. Finally, I summarize the main conclusions of my research and discuss how my results advanced the scientific field.

1 MOTIVATION

Water in the Earth's atmosphere is a uniquely powerful species. In its vaporised phase it absorbs radiation throughout the infrared spectrum and makes up about 50 % of the natural greenhouse effect (Schmidt et al., 2010). As water vapor is a strong infrared absorber it also efficiently emits infrared radiation, parts of which are directly lost to space. This mostly water vapor driven infrared radiative flux towards space cools the atmosphere by about 2 K day^{-1} throughout the mean tropical free troposphere (Jeevanjee and Fueglistaler, 2020b). To obtain an energetically balanced state in the tropics, this radiative cooling is balanced by the release of latent heat when water vapor condenses to cloud droplets within convective cells, a state that is commonly referred to as radiative-convective-equilibrium (RCE). RCE is a prime example for how water shapes the mean state of the atmosphere through its radiative and thermodynamic interactions.

Manabe and Wetherald (1967) were the first to make an RCE–based prediction of the future climate, taking into account the important effect of the water vapor feedback by assuming a fixed vertical relative humidity (RH) structure. Their prediction of a 2 K increase in surface temperature due to a doubling of CO_2, referred to as equilibrium climate sensitivity (ECS), remains close to state-of-the-art climate model predictions. However, it has become clear that more knowledge about feedback processes is required to reduce uncertainty in current ECS estimates that range between 2.6 to 3.9 K at 66 % confidence (Sherwood et al., 2020). In particular, the response of clouds to a warming climate contributes strongly to the remaining uncertainty. Understanding these cloud feedbacks constitutes a complex research objective because of the diversity of cloud types that vary in their radiative effect on the atmosphere and also because processes on scales of microns to thousands of kilometers are involved in cloud formation (Zelinka et al., 2017).

A key cloud formation process is atmospheric convection. It occurs when the atmosphere becomes sufficiently unstable for air parcels to start bubbling up the atmospheric column. Depending on properties of the large-scale environment, convection can manifest in different ways. In the inter-tropical convergence zone (ITCZ) near the equator, sea surface temperatures are high and surface winds converge resulting in deep convective clouds that reach up to the tropopause. In the sub-tropics, the free troposphere is stabilized and dried by subsiding airmasses, limiting convection to the boundary layer, resulting in shallow cumulus clouds. In recent years, the spatial organisation

of both deep and shallow cloud fields has gotten increased attention because organisation can affect the large scale mean humidity and cloud fraction, both of which are directly linked to the radiative balance of the atmosphere (Bony et al., 2017; Muller et al., 2022; Wing et al., 2020). Hence, to constrain uncertainties in cloud feedbacks, we need to understand under what circumstances cloud fields tend to organise in specific patterns or aggregate to clusters and what states will be favored in the future climate.

A mechanism thought to drive both deep and shallow convective aggregation is a radiatively driven shallow circulation that feeds near surface moist air into the convective cell while drying its environment through subsidence. The circulation is driven by enhanced radiative cooling in the vicinity of the convective cell due to an abrupt decrease of moisture from the boundary layer to the free troposphere. There is robust evidence for this mechanism to play a key role in both shallow convective aggregation (Naumann et al., 2019; Schulz et al., 2021; Schulz and Stevens, 2018) and deep convective aggregation (Dingley et al., 2021; Muller and Bony, 2015; Muller et al., 2022; Wing et al., 2017). However, the boundary layer in the convective cell's vicinity can only cool to space effectively when the atmosphere aloft is sufficiently dry, a condition that is not necessarily satisfied.

Previous studies based on in-situ measurement campaign data showed evidence of the systematic occurence of mid-tropospheric moist layers in the vicinity of deep convective cells (Johnson et al., 1996; Stevens et al., 2017; Villiger et al., 2022). I refer to these layers as elevated moist layers (EMLs). EMLs are thought to be a consequence of enhanced stability near the melting level at around 5 km altitude, causing detrainment of moist air into the convective cell's environment. A schematic overview of such a scenario is depicted in Figure 1.1. EMLs can strongly affect the vertical structure of radiative cooling by shifting the altitude of most effective cooling to space from the boundary layer top to the mid-troposphere as indicated by the red arrows in Fig. 1.1. The upward directed IR radiation from the boundary layer top is mostly balanced by downward radiation from above due to the abundance of water vapor in the presence of an EML. The EML top, however, is able to radiate energy effectively to space, causing strong cooling at the EML top since there is only little water vapor above.

The described changes EMLs induce in the spatial structure of radiative cooling affect the radiatively driven flow that is thought to maintain and aggregate the convection. This flow is indicated by the green arrow in Fig. 1.1 that reaches from the boundary layer top along the surface to feed air into the deep convective cell. This mechanism may break in the presence of an EML since the boundary layer becomes less effective at cooling radiatively. However, the strong cooling at the EML top yields subsidence in the lower free troposphere

(green arrow beneath EML) that may drive a similar return flow into the convective cell as the shallow circulation. While it is clear that EMLs have significant implications for the described mechanisms of maintenance and aggregation of convective systems, and thereby on cloud feedbacks, it is not clear how exactly their impact plays out.

Besides case studies based on in-situ observations from measurement campaigns, EMLs have not been studied extensively, leaving many unknowns, for example about their frequency of occurence, their lifetime or how they vary in strength and horizontal extend. Perhaps contributing to this gap is the fact that EMLs are difficult to observe in satellite-based retrievals, possibly denoting a blindspot for passive satellite observations (Stevens et al., 2017). Satellites enable a consistent global and long-term sampling of the atmosphere that might allow for addressing the mentioned unknowns about EMLs. Hence, the research objective I address in my first study attached in Appendix A lies in establishing whether EMLs can in principle be captured in satellite retrievals and to setup a framework of assessing to which degree EMLs can be resolved. My second study attached in Appendix B revolves around the question of how EMLs are represented in existing operational satellite retrieval products and reanalysis data. In addition I conduct a first quantification of the effect of EMLs on the meso-scale dynamics and evaluate the suitability of the different operational datasets to quantify the EMLs' dynamical impact. In the following essay I give an overview of the scientific background of my studies, the methodologies I deploy and summarize my findings.

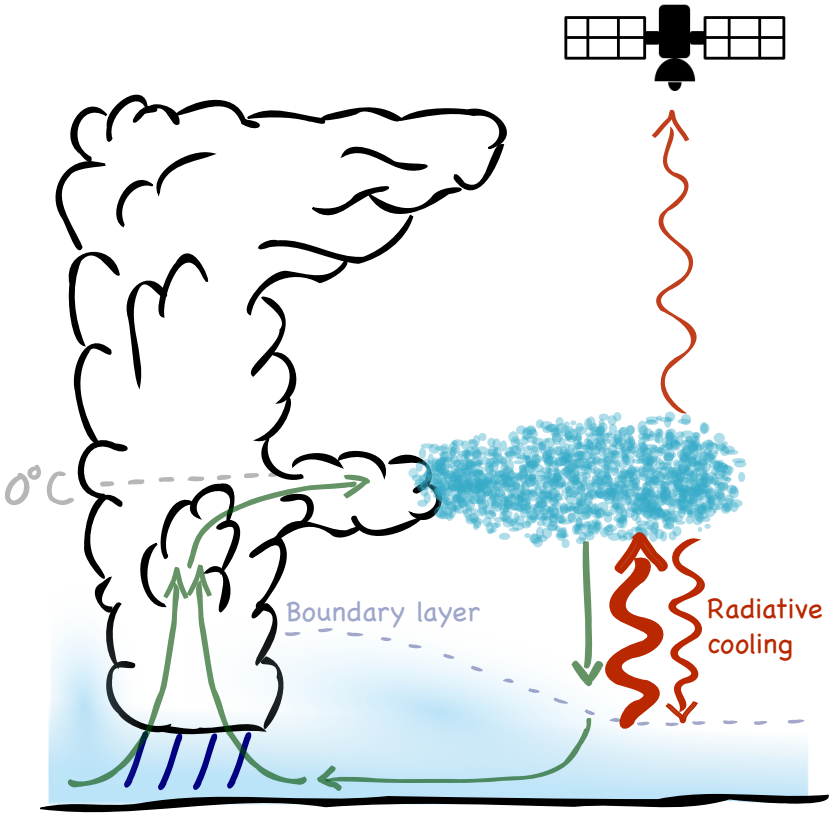

Figure 1.1: Schematic depiction of the typical meso-scale environment of an EML (area with blue circles). A deep convective cloud detrains moist air near the melting level (0 °C) into its environment, yielding an EML. Radiative cooling is indicated by curved red arrows at altitudes of strong humidity gradients, where arrow thickness is proportional to temperature at which radiation is emitted. Humidity of the boundary layer is indicated by blue shading. Green arrows indicate radiatively driven flow that may contribute to the maintenance of the convection.

2

IS THERE A MOIST LAYER BLINDSPOT IN SATELLITE OBSERVATIONS?

In this section I will first give a brief introduction to the observing principles of passive satellite observations and discuss their observing capabilities, in particular of hyperspectral infrared (IR) sounders. This will frame the initial research question about the possibility of an inherent EML blindspot for passive satellite observations, the concept of which I discuss in the second subsection. Finally, I summarize the findings of my first publication where I reproduce the EML blindspot and present a way to resolve it.

2.1 HYPERSPECTRAL INFRARED OBSERVATIONS

Satellite based remote sensing instruments offer rich spatiotemporal observational sampling of key atmospheric variables such as the vertical structure of temperature and water vapor. Information about atmospheric quantities is obtained indirectly through measurements of electro-magnetic radiation escaping Earth's atmosphere. On its path from the Earth's surface to the satellite's sensor atmospheric absorption significantly alters the spectrum of outgoing longwave radiation.

To conceptualize how the radiation reaching the satellite sensor is affected by atmospheric absorption it is useful to think of the radiation as originating from a distinct atmospheric depth that depends on the absorption strength and the amount of the absorber. The stronger the absorption and the higher the amount of the absorber the less deep the layer the radiation is emitted from. Since absorption strength is mostly known for atmospheric molecules and stored in databases like HITRAN (High-resolution Transmission Molecular Absorption Database, Gordon et al., 2017), the satellite measurement can be used to learn about the amount of the absorber in the atmosphere.

Since absorption strength is highly wavenumber dependent, in particular in the infrared spectral range, the radiation measured by the satellite at different wavenumbers originates from different atmospheric depths. The intensity of the radiation emitted from a certain atmospheric depth depends on the temperature of the emitting layer. If the temperature is known, measuring spectra of infrared radiation gives insight into vertical profiles of atmospheric constitution. Alternatively, temperature information can be deduced from the satellite observation if the atmospheric concentration of the relevant absorber at the specific wavelength is known. For example, CO_2 is a species with a well characterised atmospheric concentration, allowing for the

deduction of temperature information from CO_2 sensitive spectral ranges.

Hyperspectral infrared sounders are designed to cover a large range of wavenumbers at a high spectral resolution, yielding dense information content about atmospheric constitution and temperature. They achieve this by deploying a Michelson interferometer that – broadly speaking – seperates incoming radiation into two beams that are recombined at altered phases and hence produce an interferogram that can be measured and Fourier transformed into spectral radiances. For brevity, I refer to Physics textbooks for more detailed descriptions of the working principles of such instruments (e.g. Hariharan, 2007).

The hyperspectral IR sounders used in this work are the Infrared Atmospheric Sounding Interferometer (IASI) and the Atmospheric Infrared Sounder (AIRS). They sample the thermal IR spectrum between 645 cm^{-1} and 2760 cm^{-1} at 0.25 cm^{-1} spectral resolution. Within this spectral region various atmospheric species have absorption features, yielding information about their atmospheric concentration. In particular, water vapor shows absorption features throughout almost the entire IR spectrum due to its asymmetric molecular structure and associated modes of molecular vibration and rotation. The vibrational ν_2 absorption band around 1595 cm^{-1} (6.3 μm) shows increasing water vapor absorption from the band edge at around 1190 cm^{-1} to the band center. Satellite observations made in this spectral region yield information about the water vapor concentration throughout the troposphere.

Despite the richness of water vapor lines in the IR spectrum, the vertical resolution of water vapor retrievals is limited. This is because there is ambiguity in inverting the spectral radiances into estimates of water vapor concentration, which denotes an inherently ill-posed problem. To still conduct the inversion, sophisticated methods to obtain some best estimate of the atmospheric state are required.

Here, I follow the framework of the optimal estimation method (OEM). For brevity, I will only give a qualitative overview of the method here and introduce some more technical aspects important for my work in Sect. 2.3. For a thorough description of the method I refer to the textbook of Rodgers (2000). At its core, the OEM method assumes the atmospheric state to be represented by a multivariate Gaussian variable that can be described by a mean and a standard deviation. The atmospheric state is represented by a vector that describes the vertical structure of the atmosphere in terms of temperature and constitution. The atmospheric variability is represented by a block covariance matrix. Given some prior assumptions about the atmospheric state and its variability, the method deploys a radiative transfer model to simulate top of atmosphere spectra for a given atmospheric state. By minimising a cost function that balances devia-

tions of the estimated atmospheric state from the prior and the simulated spectrum of the estimated atmospheric state from the observed satellite spectrum, the method finds an optimal estimation of the atmospheric state. This state is considered the *retrieval*.

A useful byproduct from conducting the radiative transfer simulations when deploying the OEM method are vertical weighting functions that describe the sensitivity of the satellite spectrum to slight deviations in the retrieved atmospheric variables. These vertical weighting functions are often used to estimate the instrument's vertical resolution. For hyperspectral IR sounders the vertical resolution is found to be on the order of 1.5 km for water vapor throughout the free troposphere (Lerner, 2002; Schneider and Hase, 2011; Smith and Barnet, 2020). EMLs denote significant mid-tropospheric humidity structures with vertical extends between 1 and 3 km (Johnson et al., 1996; Stevens et al., 2017; Villiger et al., 2022). Hence, according to generic weighting function based etimates of the hyperspectral IR instrument's vertical resolution, EMLs should be detectable. However, in the next subsection I will discuss an additional observational challenge that is special about EMLs and not captured in the vertical weighting functions.

2.2 CONCEPTUALISATION OF THE MOIST LAYER BLINDSPOT

Stevens et al. (2017) present a case study of a strongly pronounced EML that was observed by dropsondes from the HALO (High Altitude Long Range) aircraft during the NARVAL-2 (Next Generation Remote Sensing for Validation Studies) measurement campaign that took place in August 2016 in the vicinity of Barbados. They present collocated satellite retrieval results based on IASI, finding that the EML is not captured at all by the retrieval. This finding marks the starting point of my first research project, where I address the question of whether there is an inherent limitation in the satellite instrument's capability to resolve EMLs or whether EMLs can in principle be captured.

Besides the satellite instrument's vertical resolution being limited, as discussed in the last subsection, there are factors that additionally constrain the instrument's observational capability. For example, clouds present optically thick objects to IR sounders, denying the instrument to gather information about the atmosphere beneath the cloud top. Another example of an additional error source is the spectral interference of absorption lines that can cause ambiguity in the interpretation of observed spectra (Sussmann and Borsdorff, 2007). When trying to estimate the concentration of one species, spectral interference with another species that is not well characterised will cause errors in the estimation of the first species. In case of an EML, I suggest that a special kind of interference is at play that makes EMLs

difficult to observe, namely between water vapor and temperature. This is a special kind of interference because temperature is not an absorption species. However, not knowing the temperature structure well induces errors in estimating the water vapor structure since both determine the spectral radiance observed in the water vapor bands as discussed qualitatively in Sect. 2.1.

My initial hypothesize is that unaccounted for temperature inversions that are typically present at the EML top induce errors in the water vapor retrieval and thereby reduce EML detectability. The increased water vapor of the EML shifts the emission layer observed by the satellite upward, where temperatures are usually lower, reducing the emitted spectral radiance observed by the satellite. However, in the presence of a temperature inversion, the reduction in spectral radiance is partly negated by the increased temperature with height in the emission layer. If the retrieval system has no prior knowledge about the temperature inversion, then this described mechanism will shade the spectral signal of the EML, limiting its detactability. In the next subsection, I summarize the findings of my first study that address how the interference of temperature and water vapor signals can cause the EML blindspot by deploying a model-based retrieval case study using the same EML scenario as Stevens et al. (2017).

2.3 DEMONSTRATION OF THE MOIST LAYER BLINDSPOT AND HOW TO RESOLVE IT

In my first study (Appendix A) I show that EML detectability by hyperspectral IR sounders is limited when relying on information only from the water vapor band as done by Stevens et al. (2017). I do so by reproducing the EML case study of Stevens et al. (2017) in a model-based retrieval setup. In this context, "model-based" refers to the fact that instead of real satellite observations I use a radiative transfer model to simulate the satellite observations. This has the benefit that I can isolate sources of error by excluding uncertainties that would inherently be part of real satellite observations. Such uncertainties are for example in the concentrations of trace gases such as CH_4 or N_2O that interfere with absorption lines of H_2O or uncertainties associated with cloudiness. For the radiative transfer simulations I use the line-by-line model ARTS (Atmospheric Radiative Transfer Simulator Buehler et al., 2018), which is a particularly accurate type of radiation model used as reference for more approximative but computationally quicker radiation schemes (Pincus et al., 2020). ARTS includes a module to conduct optimal estimation based retrievals, the concept of which I described briefly in Sect. 2.1 and in more detail in Appendix A. This method was also deployed in the study of Stevens et al. (2017) where the EML could not be retrieved. In the following, I introduce the main assumptions I make within my retrieval setup

and then summarize the results of my two most revealing retrieval scenarios.

In an optimal estimation retrieval setup, the atmospheric state is assumed to be a multivariate Gaussian variable that can be described by a mean and a standard deviation. Hence, I introduce prior knowledge about the atmospheric state that is independent of the information from the satellite measurement, in terms of an "a priori" state vector and a covariance matrix. I do so for the surface temperature, the temperature profile and the profile of water vapor, which denote my retrieval quantities. I define this a priori knowledge by making use of different datasets and assumptions. For the humidity profile I use a tropical mean profile of the FASCOD (Fast Radiative Signature Code) dataset (Anderson et al., 1986) and conduct the retrieval in units of logarithmic volume mixing ratio (VMR), which makes the variable's distribution more Gaussian. I assume to know the surface temperature precisely and apply a moist adiabatic temperature lapse rate starting from the surface up to 100 hPa and I fit a mean stratospheric temperature profile above to obtain the a priori temperature profile. For the tropics, a moist adiabatic temperature profile is a reasonable approximation (Sobel and Bretherton, 2000). The resulting a priori profiles are shown as blue lines in Fig. 2.1.

To represent the variability of the atmosphere around the mean state, I calculate covariance matrices for temperature and water vapor profiles. For water vapor, I deploy the method of Schneider and Hase (2011), who set the diagonal elements of the matrix to unity (note the log-transformation of the water vapor variable) and assume a correlation length to calculate the off diagonal elements. For temperature, I calculate the diagonal elements of the covariance matrix based on a set of tropical ocean short range forecasts from the ECMWF IFS (European Center for Medium Range Weather Forecast Integrated Forecast System) model provided by Eresmaa and McNally (2014). I make the idealized assumption that other atmospheric species and variables other than the three retrieval quantities are perfectly known, in particular O_3, CH_4 and N_2O. Further details about the exact retrieval setup can be found in Appendix A.

In my retrieval experiments shown in Fig. 2.1, I isolate the effect of choosing different spectral ranges from the IASI spectrum. Usually, retrievals do not use the full spectral range available because computational costs become high and information is redundant between channels. Stevens et al. (2017) chose a quite limited spectral region sensitive to water vapor between 1193 to 1223 and 1251 to 1253 cm^{--1}. When running my retrieval with this spectral setup I obtain the results shown in the first row of Fig. 2.1. I find that the EML is not resolved in the retrieved state, similar to the results of Stevens et al. (2017). I also find significant errors in the retrieved mid-tropospheric temperature profile in the layer of the EML, where temperature is

underestimated by the retrieval. As conceptually outlined in the previous section, underestimated temperature and humidity balances in the radiative signal in the water vapor band, yielding low costs in the spectral term of the optimal estimation cost function, although errors in the retrieved atmospheric state may be large.

The idea of the second retrieval scenario shown in the second row of Fig. 2.1 is to introduce more water vapor information by using the spectral range between 1190 to 1400 cm^{-1} suggested by Schneider and Hase (2011) and in particular independent temperature information from the CO_2 band between 645 to 800 cm^{-1}. Spectra of CO_2 mainly contain information about temperature because CO_2 is a well quantified compound in the atmosphere. Applying this setup results in a well resolved EML and temperature profile, even capturing the temperature inversion located at the EML top. Hence, although EMLs present a non-trivial vertical structure to resolve by satellite observations, I conclude that there is no inherent EML blindspot. As a next step, I investigate how operational retrieval products perform in capturing EMLs based on different reference datasets.

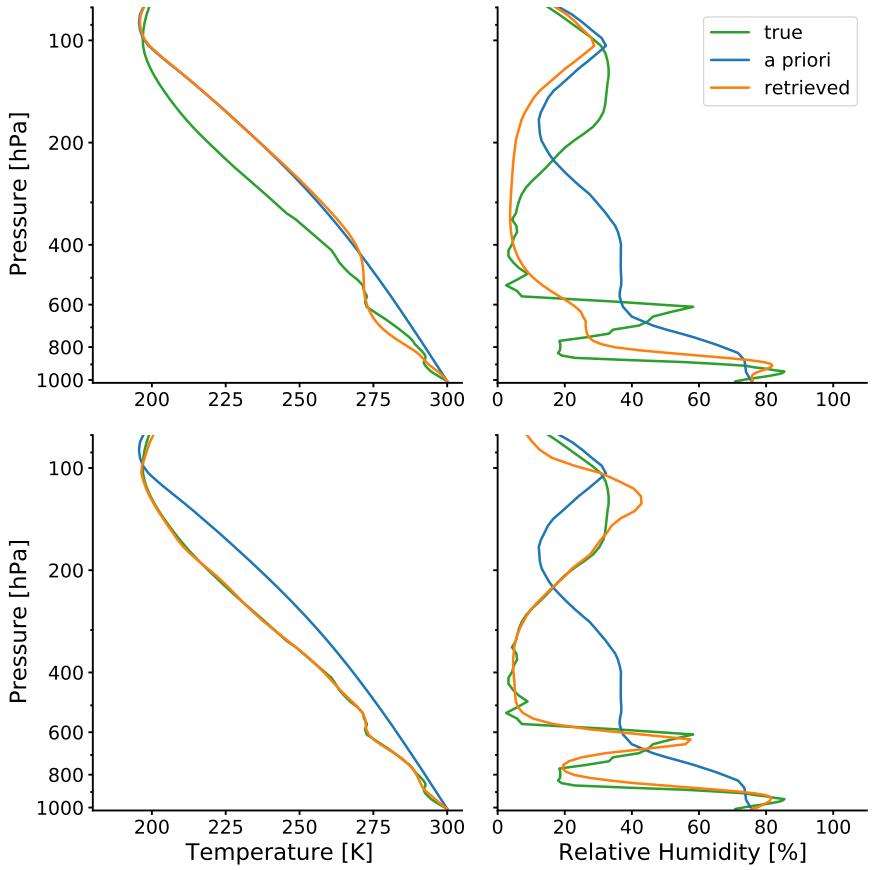

Figure 2.1: Profiles of temperature and humidity for two retrieval scenarios based on NARVAL-2 dropsonde profiles on August 12th 2016 denoted as "true" (green lines). The first retrieval scenario (first row) uses the same spectral setup as Stevens et al. (2017), reproducing the absence of the EML in the retrieved profile (orange line). The second retrieval (second row) uses a wider spectral range of H_2O lines and additional temperature information from the CO_2 band, yielding a well resolved EML in the retrieval.

3

REPRESENTATION OF MOIST LAYERS IN OPERATIONAL RETRIEVAL PRODUCTS

I showed in my first study that EMLs do not pose an inherent blindspot for satellite-based hyperspectral IR observations in an idealized model-based setup. As a next research project, I address how well operational satellite retrieval products are able to capture EMLs. For that purpose a robust database with suitable reference data denotes an important premise. In the following, I discuss the suitability of two reference datasets that I considered for this task. First, I evaluate the usefulness of dropsonde data from the EUREC^{4}A (Elucidating the role of clouds–circulation coupling in climate) measurement campaign. Then I introduce more long-term reference data from Manus Island where 2146 radiosondes where launched over the course of 4 years. Finally, I introduce a method I deploy rigorously in my first and second study to identify and quantify moist layers, allowing for a statistical assessment of EML representation in different datasets and also an evaluation of their dynamical impact.

3.1 MOIST LAYERS DURING EUREC^{4}A

EUREC^{4}A was an immense multi-national measurement campaign that took place on and around Barbados in January and February of 2020 to address urging questions about the response of trade wind clouds to warming, which are thought to contribute significantly to the intermodel spread in estimates of climate sensitivity (Bony et al., 2015; Stevens et al., 2021). Several research aircraft, ships and autonomous vehicles with a variety of observing systems were deployed to capture the physical state of the tradewind atmosphere and ocean. In particular, the research aircraft HALO was used to fly circles of about 200 km diameter while launching 12 dropsondes per circle. A research flight was typically composed of 6 circles and a diversion towards the East, into the upstream region of the trades. With 15 conducted research flights, a total of 895 dropsondes were launched from the HALO aircraft. In addition, 320 dropsondes were launched by the Lockheed WP-3D Orion N43-RF aircraft (P3) run by the National Oceanic and Atmospheric Administration (NOAA) to constitute a total number 1215 dropsonde-based soundings during EUREC^{4}A, which are accesseble and published under the dataset name JOANNE (Joint dropsonde Observations of the Atmosphere in tropical North atlaNtic meso-scale Environments, George et al., 2021a).

With the spatial and temporal coverage of the meso-scale atmospheric environment in the trades and its fine vertical resolution, JOANNE constitutes an interesting reference dataset to conduct satellite retrieval evaluation. However, for my purpose, the usefulness of the dataset strongly depends on the number of observed EMLs during the EUREC⁴A period. Johnson et al. (1996) show based on 10 year Northwestern Caribbean sounding data that melting level associated stable layers that may yield EMLs are rather expected to occur during the summer months, while EUREC⁴A was conducted during the winter months. Also the EML case study of Stevens et al. (2017) was conducted based on summer month data from NARVAL-2. Hence, the premise to find a lot of EML cases during EUREC⁴A was not optimal.

Nonetheless, some cases of increased mid-tropospheric humidity were observed during EUREC⁴A, two of which were for example investigated in more detail by Villiger et al. (2022). They show that one occurence on the 14th of February 2020 can be linked to melting level associated outflow of deep convection over South America, making it a typical EML scenario that fits the conceptual picture of Fig. 1.1. However, for this exact day there are no collocations between satellite overpasses and JOANNE data available.

In Fig. 3.1 I show cases of enhanced mid-tropospheric humidity on three days of available JOANNE data where simultaneous (within 50 km and 30 minutes) observations of IASI and AIRS retrieval products are available (EUMETSAT, 2022; Smith and Barnet, 2020). The AIRS L2 product is found to capture the moisture structures reasonably well, albeit that very sharp gradients are missed due to inherently limited vertical resolution of the satellite data as discussed in Sect. 2.1. It is also remarkable how within the mid-tropospheric moist layers on the 24th of January and the 11th of February the AIRS L2 product shows strong variability between the collocated scenes (shaded areas), indicating that the retrieval distinguishes differently pronounced moisture levels. The IASI retrieval shows only few collocations and generally a worse agreement with the dropsonde profiles compared to the AIRS product.

Although the found moist layer scenarios during EUREC⁴A are interesting to explore and give a first impression of what the operational retrieval products are capable of, they remain quite limited to very few cases. To allow for a more quantitative assessment of how retrieval products are able to capture EMLs I decided to choose a more long-term reference dataset that suits my specific purpose better than the EUREC⁴A data. In the following, I describe this reference dataset in more detail, introduce a new method to quantify EMLs and summarize the main results of my second study.

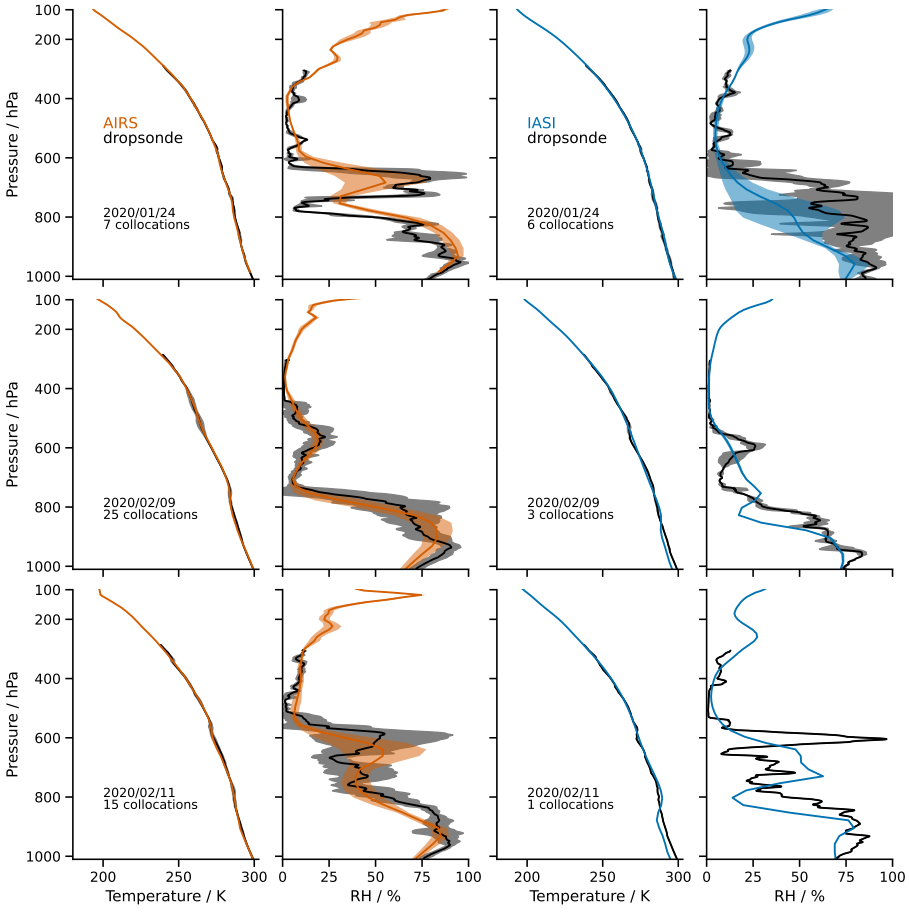

Figure 3.1: Profiles of temperature and humidity for cases of enhanced mid-tropospheric humidity where there are collocated observations of AIRS/IASI and JOANNE dropsondes.

3.2 MOIST LAYER REFERENCE DATASET FROM MANUS ISLAND

With EUREC^{4}A data not appearing to be the most suitable test ground of assessing the representativeness of EMLs in satellite data, in particular for IASI, I decided to look for a more fitting refrerence dataset. The two main criteria for this dataset are firstly that EMLs are well represented in the sampled atmospheric cases and secondly that there are simultaneous observations of the satellites I am interested in. With the EMLs' close association to deep convection, it appeared plausible to choose a region where such events occur frequently such as the Western Pacific warmpool. This region was also subject of previous studies reporting the robust occurence of mid-tropospheric stable and moist layers as well as enhanced cloudiness based on measurement campaign data of TOGA COARE (Tropical Ocean - Global Atmosphere Coupled Ocean Atmosphere Respsonse Experiment), which took place over 4 months from November 1992 to February 1993 (Johnson et al., 1996, 1999; Mapes and Zuidema, 1996; Zuidema, 1998). In addition, Romps (2014) show that the vertical humidity structure in this region shows a mid-tropospheric maximum in the mean based on ERA-Interim data, a clear sign of a strong climatological signal of EMLs.

The second criterion of selecting a suitable reference dataset is that it matches up well with overpasses of the satellites I am interested in. Given that the Western Pacific warmpool region is centered around the equator I can make use of the fact that IASI is situated on satellites with sun-synchronous orbits, meaning that they have fixed local equator crossing times. For the MetOp satellites carrying IASI this crossing time is 09:30 am/pm. The globally standardized launch times of radiosondes are 00 and 12 UTC, which means that the local launch times vary across the globe. The Western Pacific warmpool region has local time zones that make the standardized radiosonde launches matchup well with overpasses of IASI. In particular, Manus Island is located at UTC+10 hours, meaning that radiosondes are launched at 10 am/pm local time, implying only a temporal offset of 30 minutes to IASI overpasses.

On Manus Island radiosondes were launched from 2011 to 2014 on a daily basis as part of the GRUAN (Global climate observing system Reference Upper Air Network) program. As part of my second study I collocated the radiosonde data from Manus Island with the IASI Level 2 climate data recod (CDR) produced by EUMETSAT and also with ERA5 reanalysis data within 50 km and 30 minutes to assure direct comparability. I find 648 and 1921 collocated humidity profiles for the IASI L2 CDR and ERA5 data with reference to GRUAN soundings, respectively. For the AIRS retrieval product, the dataset unfortunately shows almost no collocations due to the satellite's local crossing time at 01:30 am/pm when not a lot of radiosondes are

launched on Manus Island. However, as I show in Sect. 3.4, ERA5 can be used as another suitable reference to evaluate the AIRS retrieval against.

To evaluate the representation of EMLs in the collocated datasets, I deploy a method that I introduced in my first study to identify EMLs and characterise them by means of their vertical position, their thickness and their strength. In the following, I introduce this method and summarize the main conclusions I draw from applying it in my second study.

3.3 MOIST LAYER IDENTIFICATION AND CHARACTERISATION

To effectively evaluate the representation of EMLs in the different data products I want to consider hundreds of collocated cases as described in the previous section. To identify and quantitatively compare the EMLs in the different data products some dedicated methodology is required. In my first study I already introduced a method to achieve this. The method relies on the introduction of a reference humidity profile against which moisture anomalies can be identified.

A first naive approach of defining a reference humidity profile would be to take a climatological mean profile of the tropics. However, such a definition would not only be sensitive to the vertical moisture variability I am interested in, but also to constant-in-height biases that the datasets may be subject to. Hence, it is desirable to define the reference humidity profile in a more flexible way, where anomalies arise only due to vertical humidity variability. I try to achieve this by defining the reference humidity profile as a fit against the humidity profile of interest. For this I use a second order polynomial logarithmic fit in the profile of water vapor volume mixing ratio (VMR). Such a fit captures the major tropospheric vertical variability of the humidity profile without including secondary maxima, for example due to EMLs. This way, EMLs can be identified as positive water vapor anomalies in the mid-troposphere against the reference profile fit, as shown by the blue shading for an example of a radiosonde profile in Fig. 3.2a. Note that I only consider moisture anomalies that are fully captured in the pressure range between 900 to 100 hPa and that have a minimum vertical thickness of 50 hPa to avoid very small scale variabilities.

Having identified an EML as a water vapor anomaly against the reference profile, I quantify the EML in terms of three scalar metrics, namely the water vapor anomaly strength, thickness and height. The EML strength is defined as the vertical integral over the anomalous H_2O VMR, divided by the vertical thickness of the EML. The EML thickness is defined as the altitude difference between the upper and lower intersection of the humidity and reference humidity profiles. The EML height is defined as the altitude of the center of mass of the water vapor anomaly. This way, EMLs in the collocated datasets

can be identified and their characteristics in terms of EML strength, thickness and altitude can be compared quantitatively.

The model-based framework of my first study provided a good first testing ground for the new method since the reference state is known and can be compared directly to the retrieved state. Hence, I ran the retrieval on 1288 tropical ocean atmospheres from the short-range forecast output of the ECMWF IFS model (Eresmaa and McNally, 2014). I find that the retrieval captures about 80 % as many EMLs as present in the reference data and underestimates EML strength by 17 % and EML thickness by 15 %. These findings appear plausible since some degree of smoothing is expected in the retrieval, as more thoroughly discussed in Appendix A. In general, the findings indicate a good capability of the retrieval to capture EMLs and provide a first reference when applying the method to the operational data products with reference to GRUAN radiosondes.

Finally, I expand the EML characterisation method to enable a quantification of the EMLs' dynamical effect. As outlined in Sect. 1, EMLs are relevant atmospheric features because they significantly affect the meso-scale spatial structure of radiative heating. By cooling the mid-troposphere in the vicinity of convection, subsiding air motion is induced, which may yield a shallow circulation that feeds moist air into the convective cell, favoring convective aggregation as sketched in Fig. 1.1. Hence, I am particularly interested whether the way EMLs are represented in the investigated datasets is sufficient to capture the EMLs' impact on radiative cooling and the radiatively induced subsidence. For this purpose, I calculate the radiative heating rates based on the collocated profiles of humidity and temperature using the radiative transfer model RRTMG (Rapid Radiative Transfer Model for GCMs, Mlawer et al., 1997) through its implementation in the radiative convective equilibrium model konrad (Kluft and Dacie, 2020). I then make use of the identified EMLs and quantify the EML-associated heating rates and radiatively driven subsidence rates ω_{rad} as indicated for an example in Fig. 3.2b and d. To obtain the EML-associated subsidence I divide the EML averaged heating rate by the EML averaged static stability s as shown in equations B.2 and B.1, where Q is the radiative heating rate, T the temperature, Θ the potential temperature and p pressure.

In the next section, I first summarize my findings about EML strength, thickness and height in the different operational retrieval and reanalysis datasets with reference to GRUAN radiosondes. In Sect.3.5 I summarize my findings about the representativeness of the EMLs' dynamical impact in terms of radiatively driven subsidence in the different operational datasets.

$$\omega_{rad} = -\frac{Q}{s} \tag{3.1}$$

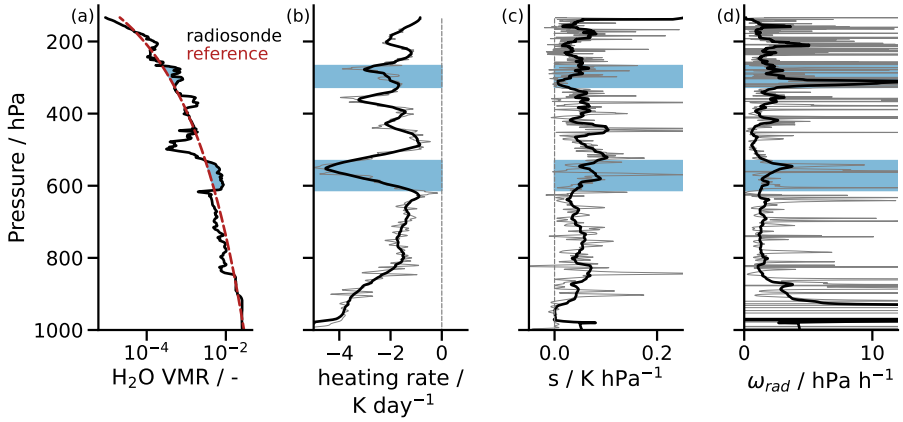

Figure 3.2: GRUAN sounding from 2012-15-02 at 12 UTC of (a) H_2O volume mixing ratio (VMR), (b) longwave heating rate, (c) static stability and (d) radiatively driven vertical velocity. The dashed red line in (a) is the reference humidity profile against which EMLs are identified, which are highlighted by blue shaded regions. Thin gray lines in (b), (c) and (d) indicate raw data and thick lines 500 m moving averages to visually remove some strong fluctuations.

$$s = -\frac{T}{\Theta}\frac{d\Theta}{dp} \tag{3.2}$$

3.4 COMPARISON OF MOIST LAYER CHARACTERISTICS

The first major result of my second study revolves around the quantification of how EMLs are represented in operational IASI and AIRS retrievals and in ERA5 reanalysis data. For that purpose, I quantify the EMLs of the collocated datasets in terms of the strength, thickness and height as described in the previous subsection. In the following, I summarize my main findings for each dataset while referring to the manuscript attached in Appendix B for the figures and a more detailed discussion.

A first indicator of a dataset's capability to capture EMLs is the number of identified EMLs when applying the method described in the previous section. I find that ERA5 captures about 99% as many EMLs as the collocated radiosonde reference data, indicating a good capabilty of ERA5 to capture free tropospheric vertical moisture variability. Comparing EML characteristics of ERA5 to GRUAN, I find that moist layers are on average 50 % weaker and 28 % thicker than moist layers in collocated radiosonde data. I find that these biases can be eliminated by applying a 1 km moving average to the radiosonde humidity profiles and then conducting the EML characterisation, indicating an effective vertical resolution of about 1 km of ERA5 humidity

profiles. Besides the limited vertical resolution there appear to be no significant limitations in ERA5's capability to capture EMLs.

The IASI retrieval dataset captures only about 75 % as many EMLs as collocated radiosonde data, indicating a more limited capability to capture free tropospheric vertical moisture variability than ERA5. Identified EMLs are also 53 % weaker and 85 % thicker than those in the collocated radiosonde data. Contrary to ERA5, these biases can not completely be removed by vertically smoothing the radiosonde profiles. In particular, EML thickness remains biased by about 30 % when applying a 1 km moving average, indicating additional error sources than smoothing in the IASI retrieval data in terms of capturing EMLs.

Since I find ERA5 to capture EMLs well, I decide to rather use ERA5 as reference data for the AIRS retrieval dataset than GRUAN radiosondes because the number of closely collocated cases between AIRS and GRUAN is very limited . The AIRS retrieval captures about 92 % as many EMLs as collocated ERA5 data, indicating more free tropospheric humidity variability than the IASI retrieval. In addition, EMLs are 26 % stronger and only 5 % thicker than those in ERA5. However, I find a significant bias in EML height of 1.3 km towards lower altitudes in the AIRS retrieval compared to ERA5. This explains the enhanced strength of AIRS EMLs because moisture anomalies tend to be stronger in the lower troposphere where absolute values of water vapor are higher. Nonetheless, the AIRS retrieval captures vertical moisture variability well as is also apparent in the examples of the EUREC^{4}A dropsonde collocations shown in Fig. 3.1. I speculate that the bias in EML height is likely caused by a technical issue of the retrieval's height coordinate assignment. I see no fundamental reason from an information content perspective for why the retrieval should create such a significant systematic deviation in the vertical position of the moisture anomalies. Concluding, I suggest that this bias is traced in more detail by the AIRS retrieval product team.

3.5 MOIST LAYERS' EFFECT ON MESO-SCALE DYNAMICS

A first step towards quantifying the representation of EMLs in the different operational data products was to quantify the EMLs themselves as summarized in the previous section. In addition, I want to quantify the representation of EMLs in terms of their impact on the meso-scale dynamics, which is what makes them relevant in their environment. EMLs are thought to influence meso-scale dynamics through their effect on the spatial structure of radiative heating as outlined in Sect. 1. Enhanced mid-tropospheric radiative cooling induces subsidence, which may drive a shallow circulation, favoring convective aggregation. Hence, the final part of my second study revolves around quantifying the moist layer associated cooling and sub-

sidence rates as captured by the different datasets using the methodology introduced in Sect. 3.3. Here, I summarize my findings about the EML-associated subsidence, as calculated through Eq. B.2, which among my results is the quantity most closely describing the EMLs' effect on the dynamics.

Based on GRUAN radiosonde data, I find that EML-associated subsidence ranges between 1.5 to 4 hPa hour^{-1} with a mean of about 2.6 hPa hour^{-1}. To put these values into some perspective, I compare them to novel meso-scale subsidence observations based on JOANNE dropsonde data from the EUREC^{4}A field campaign. Using the method of Bony and Stevens (2019), dropsonde profiles along the 200 km diameter circle flown by the HALO aircraft can be used to derive circle-integrated profiles of horizontal divergence. Using mass continuity, horizontal divergence can be translated into estimates of the vertical pressure velocity ω, some first EUREC^{4}A averaged results of which are presented by Stevens et al. (2021). They find that free tropospheric meso-scale subsidence on the mean is on the order of 1 hPa hour^{-1}, indicating that EML-associated subsidence as derived from GRUAN radiosondes denotes a significant deviation from the mean.

Although useful as a first comparison of order of magnitude, I want to point out that comparability of the EMLs I characterise in the moist, deep convective environment of Manus Island to EUREC^{4}A observations situated in the dry subsiding region of the trades may be limited. The two factors controlling EML-associated subsidence are EML-associated radiative cooling and static stability as shown by Eq. B.2. On the one hand, the generally more moist free troposphere near Manus Island reduces the effectiveness of cooling to space by the EMLs, limiting EML-associated subsidence compared to EMLs in the trades. On the other hand, the free troposphere of the trades may be more stably stratified due to the dry adiabatic warming associated with the large-scale subsidence compared to the deep convective region. This would cause increased EML-associated subsidence near Manus Island compared to the trades. It is not clear at this stage, which effect may be more significant in determining the effect of EMLs on subsidence in different regions, something that may be investigated by applying my methodology to different regions in the future.

Besides assessing the magnitude of EML-associated subsidence, which from comparison to EUREC^{4}A data appears significant, I am interested in how the IASI and AIRS retrieval products and ERA5 reanalysis data are able to capture it. Although ERA5 showed quite promising results in terms of capturing EML characteristics, I find that ERA5 underestimates the mean EML-associated subsidence by 38 % compared to collocated GRUAN radiosonde data. This bias results predominantly from overestimated static stability within the EMLs in ERA5. For the IASI retrieval I find a similar bias in EML-

associated subsidence, but underestimated radiative cooling in the EMLs has a larger contribution than for ERA5. For the AIRS retrieval product I find that EML-associated subsidence is underestimated by 43 % compared to collocated ERA5 data. Given that ERA5 already showed a 38 % bias against GRUAN, the bias identified for AIRS sticks out strongly among the investigated datasets. This is due to both underestimated EML-associated radiative cooling and overestimated static stability. I hypothesize that the underestimation of EML height in the AIRS retrieval, as described in the previous section, partly explains these biases. A lower EML height may reduce EML-associated radiative cooling because more water vapor will be above the EML, making it less efficient at cooling to space. It would be interesting to see how EML-associated subsidence is represented in the AIRS retrieval product when the root of the bias in EML height is found and resolved.

4

SUMMARY AND CONCLUSION

In the presented work I assess how Elevated Moist Layers (EMLs) are captured by satellite-based hyperspectral infrared (IR) observations and ERA5 reanalysis. EMLs are significant mid-tropospheric moisture anomalies that typically occur in the vicinity of deep convection. EMLs have only been studied based on a limited number of cases in measurement campaign data although they may have significant implications for meso-scale dynamics and possibly climate feedbacks due to their strong effect on the spatial structure of radiative heating (Johnson et al., 1996; Stevens et al., 2017; Villiger et al., 2022). This marks a gap which may be filled by making use of satellite observations that provide consistent and long-term global sampling and hence could contribute to a more complete picture of EMLs. However, the starting point of my work is denoted by the fundamental question of whether EMLs can actually be resolved by satellite observations or whether they may denote an inherent blindspot as suggested by the findings of Stevens et al. (2017).

In my first study I setup a model-based optimal estimation retrieval that is similar to the one deployed by Stevens et al. (2017). The retrieval is setup for satellite observations of the IASI (Infrared Atmospheric Sounding Interferometer) instrument, which provides a wealth of water vapor information with an estimated vertical resolution of 1.5 km in the free troposphere (Lerner, 2002; Schneider and Hase, 2011) and hence should in principle be capable of resolving EMLs. By reproducing the EML retrieval case study of Stevens et al. (2017) in my model-based retrieval I show that the absence of the EML in the retrieved water vapor profile can be traced to the deployed spectral setup. When relying on a limited number of channels only from the water vapor band, interfering errors in the retrieval of the non-trivial temperature structure associated with an EML yield the absence of the EML in the retrieved water vapor profile. By running the retrieval with an altered spectral setup, using a broader range of channels from the water vapor band an adding independent temperature information from the CO_2 band, I find that the EML can be resolved well. This is confirmed in case studies of increased mid-tropospheric water vapor during the EUREC^{4}A field campaign, where I compare operational retrieval products to collocated dropsonde measurements. Hence, to answer my first research question, there appears to be no inherent EML blindspot for passive satellite observations.

Having shown that EMLs can in principle be captured, I wanted to more quantitatively assess the capabilities and limitations of satellite retrievals to resolve EMLs. For that purpose I introduced a new

method for identifying and characterising EMLs in terms of their strength, vertical thickness and height. The method also allows for quantifying the EML-associated radiative heating and subsidence rates, which are interesting quantities to assess the dynamical impact of EMLs. The method is easy to apply to large humidity profile datasets and enables a statistical comparison of the named moist layer characteristics between satellite retrievals and reference data. Applying this method to my model-based retrieval for a large reference dataset of 1288 tropical ocean atmospheres in my first study, I find that EMLs in the retrieval dataset are about 17 % weaker and 15 % more thick than EMLs in the reference dataset. This indicates a generally good capability of the retrieval to resolve EMLs since some degree of smoothing is expected. The model-based results of my first study establish a useful reference to compare the performance of operational satellite products against, which I evaluate in the following work.

In my second study I assessed the capability of operational retrieval products of the IASI and AIRS (Atmospheric Infrared Sounder) instruments and ERA5 reanalysis data to resolve EMLs. I first evaluated the usefulness of dropsonde data from the EUREC^{4}A measurement campaign as reference, but found that there is only a limited number of EML cases that collocate well in space and time with the overpassing satellites. Instead, I decided to use a 4 year radiosonde dataset from Manus Island in the Western Pacific warmpool as reference, which matches up well with IASI overpasses and contains a lot of EML cases due to the abundance of deep convective events in this region.

Among the investigated datasets, I find that ERA5 captures EMLs most reliably, a first indicator of which is that it captures about 99 % as many EMLs as the reference radiosonde data. When smoothing the radiosonde data with a 1 km moving average, I find no significant biases in EML strength, thickness and altitude to collocated ERA5 data, indicating that ERA5 captures EMLs well on a 1 km vertical scale. Although the retrieval datasets also capture the majority of EMLs, they show some more significant biases than ERA5. The IASI retrieval shows the least amount of EMLs among the investigated datasets with only 75 % as many as the collocated radiosonde data. In addition, EMLs are about 85 % more thick in the IASI retrieval compared to the radiosonde data, indicating strong smoothing. The AIRS retrieval captures 92 % as many EMLs as collocated ERA5 data, indicating a good capability to resolve vertical humidity structures. The major drawback of the AIRS retrieval is an underestimated EML height of 1.3 km, which is likely a technical issue of the vertical coordinate assignment in the retrieval algorithm.

Finally, I investigate the dynamical impact of EMLs through the subsidence they induce by enhancing radiative cooling. I find that EML-associated subsidence is on the order of 2.6 hPa hour^{-1}, which

is significant compared to meso-scale vertical velocity estimates from the EUREC^{4}A field campaign, which are on the order of 1 hPa hour^{-1} (Stevens et al., 2021). Although ERA5 showed more promising capabilities in resolving the EMLs than IASI retrievals, I find that both datasets underestimate EML-associated subsidence by 39 %. This is because ERA5 shows more significant biases in EML-associated static stability than the IASI retrieval. The AIRS retrieval shows a 43 % underestimated EML-associated subsidence compared to ERA5, which is caused by both underestimated radiative cooling and overestimated static stabilities. This bias may partly be attributed to the underestimated EML height since more water vapor above the EMLs reduces the effectiveness of the cooling.

With my studies I provide new scientific insights for satellite retrieval algorithms to enable a good representation of EMLs. I do so on the one hand by suggesting a cause for the apparent EML blindspot in the case study of Stevens et al. (2017) and proposing a solution to resolve the EML. On the other hand I provide a quantitative picture of the representation of EMLs in operational satellite retrievals and ERA5 reanalysis data, which can be used to diagnose issues in the retrieval algorithms and act on them. In addition, I show that EMLs are associated with significant radiatively induced subsidence, which may have implications for convective aggregation and climate feedbacks. Hence, I suggest that studying the role of EMLs for the dynamics of their meso-scale environment denotes a relevant research question in the future.

Part II

APPENDIX

A

ARE ELEVATED MOIST LAYERS A BLIND SPOT FOR HYPERSPECTRAL INFRARED SOUNDERS? A MODEL STUDY

This chapter contains a paper that has been published in *Atmospheric Measurement Techniques* as Prange et al. (2021a):

Prange, Marc, Manfred Brath, and Stefan A. Buehler (2021). "Are elevated moist layers a blind spot for hyperspectral infrared sounders? A model study." In: *Atmospheric Measurement Techniques* 14.11, pp. 7025–7044. DOI: https://doi.org/10.5194/amt-14-7025-2021.

CONTRIBUTIONS I setup the optimal estimation retrieval in ARTS, conducted the retrieval simulations, evaluated the results and wrote the manuscript. MB helped with setting up the retrieval in ARTS and together with SAB majorly contributed to the hypothesis on what may cause the EML blindspot and how to resolve it. MB and SAB also provided input on the structure of the manuscript and feedback on the text.

Are elevated moist layers a blind spot for hyperspectral infrared sounders? A model study

Marc Prange[1,2], Manfred Brath[1], Stefan A. Buehler[1]

[1] *Universität Hamburg, Faculty of Mathematics, Informatics and Natural Sciences, Department of Earth System Sciences, Meteorological Institute, Hamburg, Germany*
[2] *International Max Planck Research School on Earth System Modelling, Hamburg, Germany*

ABSTRACT

The ability of the hyperspectral satellite based passive infrared (IR) instrument IASI to resolve Elevated Moist Layers (EMLs) within the free troposphere is investigated. EMLs are strong moisture anomalies with significant impact on the radiative heating rate profile and typically coupled to freezing level detrainment from convective cells in the tropics. A previous case study by Stevens et al. (2017) indicated inherent deficiencies of passive satellite based remote sensing instruments to resolve an EML. In this work, we first put the findings of Stevens et al. (2017) into the context of other retrieval case studies of EML-like structures, showing that such structures can in principle be retrieved, but retrievability depends on the retrieval method and the exact retrieval setup. To approach a first more systematic analysis of EML retrievability, we introduce our own basic Optimal Estimation (OEM) retrieval, which for the purpose of this study is based on forward modelled (synthetic) clear-sky observations. By applying the OEM retrieval to the same EML case as Stevens et al. (2017) we find that a lack of independent temperature information can significantly deteriorate the humidity retrieval due to a strong temperature inversion at the EML top. However, we show that by employing a wider spectral range of the hyperspectral IR observation, this issue can be avoided and EMLs can generally be resolved. We introduce a new framework for the identification and characterisation of moisture anomalies, a subset of which are EMLs, to specifically quantify the retrieval's ability of capturing moisture anomalies. The new framework is applied to 1288 synthetic retrievals of tropical ocean short-range forecast model atmospheres, allowing for a direct statistical compar-

ison of moisture anomalies between the retrieval and the reference dataset. With our basic OEM retrieval, we find that retrieved moisture anomalies are on average 17 % weaker and 15 % thicker than their true counterparts. We attribute this to the retrieval smoothing error and the fact that rather weak and narrow moisture anomalies are most frequently missed by the retrieval. Smoothing is found to also constrain the magnitude of local heating rate extremes associated with moisture anomalies, particularly for the strongest anomalies that are found in the lower to mid troposphere. In total, about 80 % of moisture anomalies in the reference dataset are found by the retrieval. Below 5 km altitude, this fraction is only on the order of 52 %. We conclude that the retrieval of lower to mid tropospheric moisture anomalies, in particular of EMLs, is possible when the anomaly is sufficiently strong and its thickness is at least on the order of about 1.5 km. This study sets the methodological basis to more comprehensively investigate EMLs based on real hyperspectral IR observations and their operational products in the future.

A.1 INTRODUCTION

The vertical structure of tropospheric water vapor is an important driver for dynamical processes due to its effect on the radiative heating profile. In particular, Muller and Bony (2015) found that the spatial variability of the radiative heating profile gives rise to spatial self-aggregation of convection, which is thought to be a key factor for uncertainties in climate projections (Bony et al., 2015; Mauritsen and Stevens, 2015). A contributing phenomenon to the spatial variability in radiative heating profiles are moisture inversions in the tropical lower to mid free troposphere, so called Elevated Moist Layers (EMLs). To our best knowledge, EMLs were first identified by Haraguchi (1968) over the tropical eastern Pacific and independently by Ananthakrishnan and Kesavamurthy (1972) over India. A first systematic connection of these EMLs to the freezing level was brought to attention by Johnson et al. (1996), who formally distinguished between the commonly referred to trade wind inversion between 2 and 3 km (Cao et al., 2007) and another stable layer aloft that manifests during summer months just below the freezing level. Both, the trade wind inversion and the stable layer at the freezing level are capable of trapping moisture beneath and forming strong vertical humidity gradients. The stable layer around the freezing level has recently been brought to attention again within the framework for assessing the tropical lower tropospheric moisture budget introduced by Stevens et al. (2017).

While the general role of EMLs within their meso-scale environment has not yet been assessed conclusively, there are conceptual ideas about the emergence of EMLs and their impact on meso-scale atmospheric dynamics. Johnson et al. (1996) and Stevens et al. (2017) both hypothesise that EMLs preferably emerge in the vicinity of moist convective cells that penetrate the freezing level, where enhanced stability leads to detrainment of the saturated air. Stevens et al. (2017) further highlight the stabilising effect of glaciation above the freezing level within the initial convective cell on the environment, which further impedes nearby convection from penetrating the freezing level, leading to increased cloudiness and moisture. Studies investigating vertical modes of cloudiness in the tropics further support the idea of preferred convective detrainment near the freezing level (Johnson et al., 1999; Posselt et al., 2008; Zuidema, 1998). Following the findings of Muller and Bony (2015), EMLs may also contribute to the maintenance and aggregation of convection via the strong vertical gradient they induce in the radiative heating profile. The strong cooling at the EML top induces subsidence and horizontal mass convergence, while near the surface a mass divergence is induced. The mass divergence near the surface in the vicinity of convection may act to maintain the convection.

Stevens et al. (2017) conducted an observational case study of an EML present during the NARVAL-2 (Next Generation Remote Sensing for Validation Studies) measurement campaign. One method they deployed was a satellite retrieval analysis based on passive microwave and hyperspectral infrared (IR) observations, both of which showed poor performance in capturing the EML structure, suggesting that EMLs present a somewhat fundamental blind spot for passive satellite observations.

We start out by providing additional scientific context to the findings of Stevens et al. (2017) by briefly reviewing the results of other hyperspectral IR retrieval studies that investigated EML-like cases in Sect. A.1.1. In Sect. A.2, we introduce our own basic Optimal Estimation (OEM) retrieval setup that we extensively use later on to investigate a physical cause for missing the EML structure and to attempt a first quantitative and comprehensive analysis of moist layer retrievability. This study is based on forward modelled (synthetic) observations to reduce the complexity of error sources (e.g. by collocation uncertainty, clouds, forward modelling errors) and to rather assess inherent limitations in resolving vertical moisture structures with hyperspectral IR observations. Section A.3 introduces a framework for identifying and characterising moisture anomalies, which we use to specifically quantify the retrieval's ability to the capture the moisture anomalies' vertical position, their thickness and their strength. In Sect. A.4 we first apply our OEM retrieval to the EML scenario discussed by Stevens et al. (2017) to assess whether the strong temperature inversion at the EML top, when not properly resolved, is capable of masking the EML in the humidity retrieval. We want to note that we do not aim to reproduce the results of Stevens et al. (2017), but discuss a possible physical reason for their found EML blindspot. Then the retrieval is applied to forward simulated (synthetic) IASI observations based on an ensemble of 1288 clear-sky atmospheric profiles over the tropical ocean, which are part of the ECMWF diverse profile database introduced by Eresmaa and McNally (2014). Based on that, the absolute retrieval error and the smoothing error are quantified statistically in Sect. A.5. Based on the framework introduced in Sect. A.3 for identifying and characterising moisture anomalies, the retrieval's ability to capture the moisture structures of the test dataset and their footprint on the heating rate profile is assessed in Sect. A.6. The results are summarized and final conclusions are drawn in Sect. A.7.

A.1.1 *Previous moist layer retrievals*

Since mid-tropospheric moist layers are no uncommon phenomenon in the tropics (Johnson et al., 1996), they have shown up in hyperspectral IR retrieval case studies in the past. Although none of these

studies were explicitly dedicated towards a comprehensive and quantitative analysis of retrieving EMLs, they still give a qualitative impression of the possibilities and limitations in resolving these features based on various retrieval methods and give some context to the results of Stevens et al. (2017).

A particularly performant and versatile retrieval approach was introduced by Smith et al. (2012) that is based on Empirical Orthogonal Function (EOF) regression and combines a clear-sky and cloud trained retrieval to allow for retrievals above clouds and below thin or broken clouds. The method is commonly referred to as Dual Regression (DR) retrieval. In a case study of retrieving temperature and humidity profiles in the eye of hurricane Isabel in 2003, Smith et al. (2012) demonstrate the retrieval's ability to capture the general tropospheric moisture structure in the presence of shallow cumulus clouds that go along with a vertically extended EML between 850 to 550 hPa. However, no highly resolved reference soundings are available for this case study. Weisz et al. (2013) further elaborate on the DR retrieval methodology, with particular focus on cloud top height retrieval and they present some additional case studies for clear-sky and cloudy scenes. The NCEP (National Center for Environmental Prediction) GDAS (Global Data Assimilation System) analysis product is used as a reference for the retrieved profiles and particularly large deviations are found for the clear-sky case, where a less pronounced moist layer is not resolved by the retrieval in the mid troposphere.

Latest advances in the DR retrieval with regard to vertical resolution are presented by Smith and Weisz (2018), who try to account for the effect that the regression tends to alias the retrieval towards the mean state of the test data base, supressing vertical variability. They do so by applying their DR retrieval to forward simulated spectra of NCEP GDAS analysis, the resulting profiles of which are used to dealias the observational retrieved profiles. Smith and Weisz (2018) show in a case study that the DR retrieval by itself is not able to resolve a significant mid tropospheric moist layer, but the dealiasing method allows to resolve it's general structure. For this study a well collocated radiosonde serves as reference.

Another EML retrieval case study is conducted by Zhou et al. (2009), who use a slightly different retrieval scheme than the previously introduced DR method. While Zhou et al. (2009) also apply an EOF regression retrieval with clear-sky and cloudy specific regression coefficients in a first step, they additionally apply a physical OEM retrieval in a second step. The retrieval is applied to IASI observations from the Joint Airborne IASI Validation Experiment (JAIVEx), where dedicated collocations between in-situ soundings and IASI onboard MetOp-A were achieved. A particularly well collocated dropsonde profile shows a strongly pronounced EML between 3 to 6 km altitude,

which the IASI retrieval is able to capture well, given the expected smoothing error due to limited vertical resolution. It may well be that the additional physical retrieval step is what makes the difference in being able to retrieve an EML, when compared to the previously discussed results of the DR retrieval. This is supported by results of Calbet et al. (2006) who investigated the ability of different retrieval algorithms implemented in the EUMETSAT (European Organisation for the Exploitation of Meteorological Satellites) IASI L2 processor to resolve vertical moisture and temperature structures based on AIRS (Atmospheric Infrared Sounder) data. In particular, Calbet et al. (2006) use a collocated clear-sky radiosonde that shows a mid tropospheric moist layer. While the EOF regression retrieval shows no hint of the moist layer, the iterative physical retrieval scheme is able to resolve the structure quite well.

As a final reference, Chazette et al. (2014) investigated EUMETSAT's IASI L2 product performance based on collocated ground based Raman lidar observations from two field experiments. The comparison is done for clear-sky conditions and from ground up to about 6 km altitude. Some significant vertical moisture variability, including moist layers, is captured by the lidar in the mid troposphere in several cases, but appears to not at all be resolved by the IASI retrieval. In their conclusions, Chazette et al. (2014) report that the IASI L2 processor would be complemented by microwave sounder data from the MetOp instrument suite in a future version, in particular to improve vertical resolution. We can confirm that this has been implemented to the current IASI L2 processor (EUMETSAT, 2017), but we are not aware of a dedicated followup study on retrievability of the vertical moisture structure.

From this discussion of mid tropospheric moist layer retrieval case studies we conclude that such atmospheric features do not generally appear to pose a blindspot for hyperspectral IR observations. While purely EOF regression based methods seem to systematically struggle to resolve non-trivial moisture structures, OEM based methods show clear capabilities of resolving them. Hence, the absence of the strongly pronounced EML investigated by Stevens et al. (2017) in their OEM retrievals rather motivates a re-investigation of the exact retrieval setup that was applied rather than be interpreted as a consequence of inherent limitations in passive remote sensing observations. By applying the basic OEM retrieval scheme introduced in the next section to synthetic IASI observations of the dropsonde profiles discussed by Stevens et al. (2017) we want analyse whether temperature induced errors act as a plausible physical cause for the absence of the EML in the retrieval in Sect. A.4.

A.2 THE RETRIEVAL

Extracting atmospheric state variables such as the temperature or concentrations of atmospheric constituents from passive satellite observations generally poses an under-constrained inverse problem. Sophisticated methods are required to regularise the problem, some of which were already mentioned in the previous section. The OEM approach showed the most promising results for resolving non-trivial moisture structures in the studies discussed in Sect. A.1.1, but was also used for the missed EML case of Stevens et al. (2017). This motivates the introduction of our own OEM retrieval setup to more systematically assess possibilities and limitations in resolving EMLs. Note that we do not aim our retrieval to be particularly performant or as versatile as operational retrieval schemes (**Eumetsat2017**; Berndt et al., 2020; Smith and Barnet, 2020). Instead, we use the retrieval as a tool to assess basic moist layer retrievability on a low level of complexity. The formalism used in this work strongly follows the comprehensive framework introduced by Rodgers (2000). Within the next subsections the technical implementation of the retrieval setup used in this study is introduced.

A.2.1 *Spectral setup*

The retrieval setup of this study aims at resolving the vertical structure of water vapor in the troposphere, with particular focus on EML scenarios. The rotational-vibrational water vapor absorption band centered around 6.25 µm (1594.78 cm^{-1}) (see Fig. A.1) offers rich vertically distributed information. We use all IASI channels in the range between 1190 to 1400 cm^{-1}, following the work of Schneider and Hase (2011), who demonstrated the suitability of this spectral range for retrieving profiles of water vapor and its secondary isotopologues.

The spectral signal of water vapor depends not only on the atmospheric water vapor itself but also on the temperature, surface emissivity and temperature, methane and nitrous oxide. Schneider and Hase (2011) and Borger et al. (2018) concurrently found that temperature induced errors can yield up to 15 % relative error for the lower to mid tropospheric H_2O retrieval, which is significant compared to other sources of error, such as interfering species. Therefore, unresolved temperature features may falsely be interpreted as water vapor signals. We assume that this is particularly relevant for EML scenarios because the strong vertical humidity gradients typically go along with temperature inversions. To reduce this error, we add independent temperature information to the retrieval from the spectral range between 645 to 800 cm^{-1}, which is part of the CO_2 absorption band centred around 15 µm (666.67 cm^{-1}). The shading in Fig. A.1 indicates the H_2O degrees of freedom calculated as the

trace of the averaging kernel matrix when only each respective channel is used (Rodgers, 2000). It is apparent that water vapor absorption is significant throughout most of the thermal IR spectrum, yielding DOF values close to unity . Blue shading indicates where water vapor independent information can be extracted from the spectrum, which is desirable to maximize temperature information content. Note that channels are highly redundant, so DOFs of individual channels do not add up. The total DOF for water vapor in the used channel set is approximately 12.9, for temperature 23.5 and for surface temperature 0.99. Interestingly, Fig. A.1 visually shows that the shortwave CO_2 band is associated with less water vapor interference in its flank between around 2200 to 2300 cm^{-1} than the longwave CO_2 band. However, due to known daytime dependent non-LTE associated biases and a worse signal to noise ratio in the shortwave channels of IASI (Clerbaux et al., 2009; Matricardi et al., 2018; Razavi et al., 2009), we only use the longwave CO_2 channels.

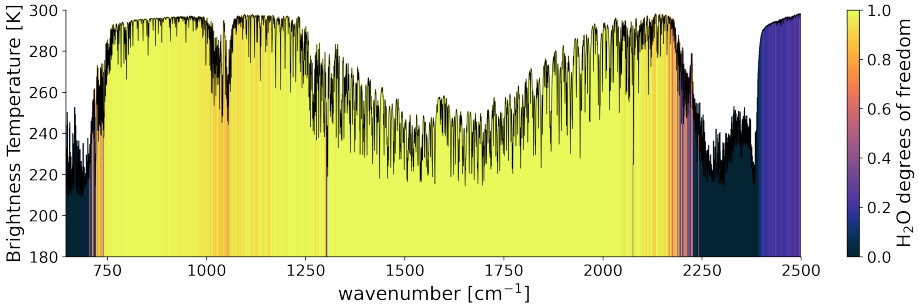

Figure A.1: Forward simulated spectrum in the spectral range of the IASI instrument. Colors denote the water vapor information content of individual channels calculated as the trace of the averaging kernel matrix when only each respective channel is used. Hence, the colored shading does not account for redundancy of information between channels, but simply conveys where water vapor absorption is significant.

To assure that the radiative background of the surface is represented well in the retrieval, 5 window channels are added to the spectral setup that have been identified by Boukachaba et al. (2015) as suited window channels. The channels are located at wavenumbers 901.5 cm^{-1}, 942.5 cm^{-1}, 943.25 cm^{-1}, 962.5 cm^{-1} and 1115.75 cm^{-1}. The complete spectral setup encompasses 1464 channels.

As a final note on the channel selection, the aim with our retrieval is not to make it computationally efficient, but to use it as a tool to explore the limitations in resolving vertical moisture features with IASI. Hence, we do not employ any channel selection method, although we are aware of the rich literature in this context (Chang et al., 2020; Collard, 2007; Fourrié and Rabier, 2004; Fourrié and Thépaut, 2003; Martinet et al., 2013, among others).

A.2.2 *Retrieval quantities*

The quantities targeted for retrieval in this study are the profiles of water vapor volume mixing ratio ($\vec{VMR}_{H_2O}$), temperature ($\vec{T}$) and the surface temperature (T_s). They are represented by the retrieval state vector :

$$\vec{x} = \begin{pmatrix} \log(\vec{VMR}_{H_2O}) \\ \vec{T} \\ T_s \end{pmatrix} \tag{A.1}$$

The water vapor profile is retrieved in natural logarithmic units, which is favourable for two reasons. Firstly, VMR_{H_2O} is a quantity that ranges over several orders of magnitude from a few percent near the surface to $O(10^{-6})$ in the upper troposphere and above, which is numerically inconvenient for the optimisation algorithm. Secondly, the transformation to logarithmic units avoids the possibility of physically implausible negative VMR values.

The major interfering trace gas species in the chosen spectral region that are not part of the retrieval state vector $\vec{x}$ are CH_4 and N_2O. Based on the error budget analysis conducted by Schneider and Hase (2011) it is not expected that these species are significant sources of error compared to errors in the temperature profile. Hence, for simplicity, we include CH_4 and N_2O in the absorption setup, but use fixed profiles and do not retrieve them.

A.2.3 *Optimal estimation algorithm*

Besides the state vector depicted in Eq. A.1, our OEM setup includes profiles of other atmospheric absorption species, namely N_2, N_2O, CH_4, O_2, CO_2 and O_3 as fixed forward model parameters. To account for nonlinearity, an iterative Levenberg-Marquardt (LM) solver (Levenberg, 1944; Marquardt, 1963) is used, which as input, besides the (synthetic) spectrum needs a priori and measurement covariance matrices, an a priori state vector and Jacobians, calculated for each iteration step by a forward model. We follow the notation introduced by Rodgers (2000), who provides an elaborate description of the procedure.

A.2.4 *The forward model and representation of IASI*

The radiative transfer model used in this study is version 2.5.0 of the Atmospheric Radiative Transfer Simulator (ARTS). A comprehensive and compact description of ARTS is provided by Eriksson et al. (2011) and Buehler et al. (2018) and more documentation can be found

on the ARTS website (https://www.radiativetransfer.org). Here, only the features that are directly relevant for the conducted retrieval calculations are presented.

ARTS calculates the emitted radiation and its transmission through a given atmospheric state on a line-by-line basis. Spectral line data were taken from the HITRAN (High Resolution Transmission) molecular spectroscopic database (Gordon et al., 2017) and continuum absorption of water vapor, oxygen, nitrogen and CO_2 are represented by the MT_CKD model for continuum absorption (Mlawer et al., 2012).

The radiative transfer simulations are conducted as monochromatic pencil beams on a frequency grid with a resolution of 0.25 cm^{-1}, which coincides with the spectral sampling interval of IASI. The obtained spectra are then convolved with a Gaussian weighting function with a Full Width at Half Maximum (FWHM) of 0.5 cm^{-1} to mimic the spectral response function of IASI. These technical specifications are taken from Coppens et al. (2019). Gaussian noise with a standard deviation of 0.1 K is added to the forward simulated spectra to represent the radiometric noise of IASI within the spectral range used in this study (Clerbaux et al., 2009). The sensor is assumed to be in 850 km altitude and to have a nadir viewing direction. The atmospheric cases simulated are limited to clear-sky and are above ocean surfaces, where the surface emissivity in the spectral region covered by IASI is assumed to be 1.

The ARTS internal OEM module, which is part of ARTS as of version 2.4.0, is used to conduct the actual retrieval calculations.

A.2.5 *A priori assumptions*

The a priori assumptions about the atmospheric state are defined as the knowledge about the state prior to the measurement. Although the true state is always known within the frame of this model study, the a priori knowledge is chosen based on information that would also be available in the situation of a real measurement. The a priori knowledge is represented by an a priori state vector $\vec{x}_a$ and a covariance matrix $\mathbf{S}_a$. For the definition of the a priori state the tropical mean atmospheric state from the profile database of Anderson et al. (1986) is used as a basis, which from now on will be referred to as tropical FASCOD (Fast Radiative Signature Code) atmosphere.

Where not stated otherwise, the a priori surface temperature is assumed to be the true surface temperature with an added Gaussian noise of 1.5 K. The Gaussian noise aims to simulate the accuracy of a real a priori surface temperature estimate, which can for example be obtained from AVHRR (Advanced Very High Resolution Radiometer), which together with IASI is part of the MetOp satellite's payload. Here, 1.5 K is a conservative assumption for tropical ocean surfaces since uncertainties in AVHRR sea surface temperature data records

are typically an order of magnitude lower, e.g. estimated at 0.18 K in the dataset of Merchant et al. (2019).

The a priori temperature profile is assumed to be moist adiabatic up to around 100 hPa. The a priori surface temperature is used as a starting point for the moist adiabat. A moist adiabatic tropospheric temperature profile is a reasonable assumption because the temperature lapse rate is mostly set to be moist adiabatic within the tropics by deep convection and by the homogenisation of the temperature field by gravity waves due to the lack of a Coriolis force (Sobel and Bretherton, 2000). Around 100 hPa and above, the moist adiabat is relaxed to the tropical FASCOD atmosphere with a hyperbolic tangent weighting function to represent the tropopause and the atmosphere above. The a priori VMR_{H_2O} profile is defined by combining a fixed relative humidity profile (RH) and the a priori temperature profile by using the relation:

$$VMR_{H_2O} = \frac{RH\, e_s(T)}{p} \tag{A.2}$$

The fixed tropical FASCOD RH profile is used and the equilibrium pressure of water vapor $e_s(T)$ is calculated based on the a priori temperature profile. p is the atmospheric pressure in a given altitude. $e_s(T)$ is calculated as the equilibrium pressure over water for temperatures above the triple point and over ice for temperatures more than 23 K below the triple point. For intermediate temperatures the equilibrium pressure is computed as a combination of the values over water and ice according to the IFS documentation (ECMWF, 2018).

The a priori assumption about the variability of the retrieval quantities is encoded by $\mathbf{S}_a$, which consists of blocks for each retrieval quantity. For the surface temperature, a variance of 100 K^2 is assumed. The diagonal elements of the temperature profile block of $\mathbf{S}_a$ (Fig. A.2b) are calculated based on tropical ocean profiles from the database provided by Eresmaa and McNally (2014), which is based on the ECMWF IFS forecast model with a focus on a broad sampling of temperature profiles. The nondiagonal elements are calculated based on a correlation length that linearly increases from 2.5 km at the surface to 10 km at and above the tropopause.

For the water vapor covariances (Fig. A.2c), the approach of Schneider and Hase (2011) is adapted, where the diagonal elements of the log-scale water vapor covariances are set to 1 in the troposphere and linearly reduce to 0.25 within the stratosphere. An adjustment made here is that below 2 km, which is a crude estimate for the boundary layer height above ocean surfaces, the diagonal value linearly decreases to 0.1 at the surface. This better represents the generally fixed moisture structure near the tropical ocean surface. The nondiagonal elements are calculated based on the same correlation length approach as for the temperature covariances.

An additional constraint about the atmospheric variability is introduced by filling in values for the cross-covariances between the three retrieval quantities. The diagonals of the cross covariance blocks are calculated as the product of the diagonals of the two respective covariance blocks, multiplied with a scale factor that exponentially decreases from 1 at the surface to $1/e$ in a given altitude. This altitude is chosen to be 100 m for the cross covariance between surface temperature and temperature to represent the dependence of the atmospheric temperature on the surface temperature. Between temperature and water vapor the altitude is chosen to be 1000 m to represent the dependence of water vapor on temperature within the boundary layer, where the water vapor content is mainly constrained by the saturation pressure, which is mainly a function of temperature. The nondiagonal elements of the cross-covariances are calculated with the same correlation length approach as for temperature and water vapor. Figure A.2(a) shows the resulting cross-covariance matrix, which only has significant values within the boundary layer.

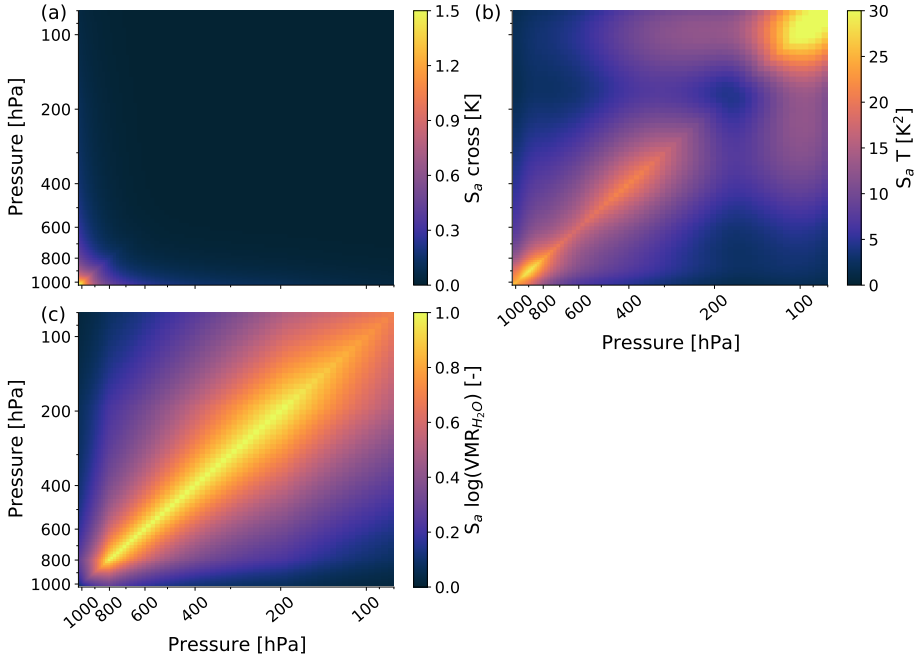

Figure A.2: Covariance matrices of $\log(\mathrm{VMR}_{\mathrm{H_2O}})$ (c), temperature (b) and the cross-covariance matrix between water vapor and temperature (a) used for the retrieval in this study. Each of these matrices constitutes a block within the full covariance block matrix $\mathbf{S}_a$. Note that it is sufficient to show only one cross-covariance matrix block, since $\mathbf{S}_a$ is block symmetric.

A.3 DEFINITION AND CHARACTERISATION OF MOISTURE ANOMALIES

This section introduces a quantitative framework to identify and characterise EMLs. This framework aims to provide an intuitive description of moisture anomaly features through a number of scalar moisture anomaly characterisation metrics and allows for a more targeted evaluation of retrieval results in Sect. A.4 and A.6.

At the core of this moisture anomaly identification method is the definition of a reference humidity profile, against which the anomalies occur. There are several ways a reference profile can be constructed and the suitability of a definition depends on the aim of the analysis. For example, a simple climatological mean profile may be a suited reference if one is interested in the mean anomaly (e.g. the bias) of a test dataset of humidity profiles. However, for the purpose of this study it is not of interest whether a humidity profile is generally rather moist or dry, but instead only anomalous vertical variability of humidity is of interest. This is because the vertical moisture variability is what manifests as a footprint on the heating rate profile (Q) and thereby affect the vertical stability or even yield vertical motion (Albright et al., 2020).

To capture moisture anomalies closely related to the vertical moisture variability, the reference profile is constructed by least-square fitting a quadratic function to the $\log(\mathrm{VMR}_{H_2O})$ profile of the troposphere up to 100 hPa. A quadratic function is preferable over a linear function because in many cases the VMR_{H_2O} profile shows large scale non-exponential variability which should not interfere with the more small-scale anomalies we want to characterise. The following function is used as the reference water vapor profile:

$$\log(\mathrm{VMR}_{H_2O,\mathrm{ref}}) = az^2 + bz + c \tag{A.3}$$

The humidity at the surface is represented by $\mathrm{VMR}_{H_2O,\mathrm{ref}}(z = 0) = \exp(c)$ and is fixed to the surface value of the actual humidity profile. The altitude z is used as a height coordinate for fitting because compared to pressure it has the benefit that $z = 0$ at the surface. The coefficients a and b are determined by least-square fitting to the logarithm of the humidity profile between the surface and 100 hPa because the assumed relation becomes less valid closer to the tropopause. After calculating the reference profile, moisture anomalies can be identified and characterised.

To visualise the moisture anomaly identification and characterisation procedure, we show an atmospheric scenario in Fig. A.3 that includes an EML as an example. The EML associated structures include a distinct moisture inversion (increase of VMR_{H_2O} with height) with maximum humidity at around 650 hPa. Temperature inversions

at the EML top and at the distinct drop of moisture at around 900 hPa are also present (not shown).

Figure A.3(b) shows the close relation between the vertical humidity structure and the net heating rate Q (longwave + shortwave), which is calculated with the radiative transfer model RRTMG (Rapid Radiative Transfer Model for GCMs, Mlawer et al., 1997) through its implementation in the radiative convective equilibrium model *konrad* (Kluft and Dacie, 2020). Q is calculated for all conducted retrievals throughout this study to assess whether the vertical humidity structure is captured in a way in which also Q is represented well.

The blue and orange shading associated with moist and dry anomalies depicted in Fig. A.3 visualises that by definition layers of positive and negative moisture anomalies alternate in the vertical. Each such layer can be viewed as a moisture anomaly object, which we characterise by means of the scalar metrics introduced in Table 1. These metrics include the vertical bounds of the moisture anomaly in terms of altitude (z_{bot} and z_{top}), the difference of which denotes the anomaly's thickness (Δz_{anom}). The anomaly height (z_{anom}) is defined as the mean over the anomaly's height interval, weighted by the anomalous humidity within the altitude bounds. Finally, the anomaly strength (s_{anom}) is defined as the mean anomalous $\mathrm{VMR}_{\mathrm{H_2O}}$ within the anomaly's vertical bounds. We only consider positive (moist) anomalies that are fully captured in the pressure range between 100 and 900 hPa, e.g. the positive anomalies at the very top and bottom of Fig. A.3 are neglected (grey shading) to avoid tropopause and boundary layer related anomalies.

A.4 CASE STUDY OF A MOIST LAYER RETRIEVAL

In this section the retrieval introduced in Sect. A.2 is applied to synthetic IASI observations of the dropsondes that sampled the EML discussed by Stevens et al. (2017). This case study is of particular interest because the found EML blindspot of Stevens et al. (2017) contradicts the results of other OEM based studies discussed in Sect. A.1.1. Here we first want to specifically assess the importance of temperature information for properly resolving the moisture structure in an EML scenario. While in general it is well known that the humidity retrieval depends on the quality of the assumed or retrieved temperature profile, we argue that for EMLs this effect is of particular relevance. In a next step, the averaging kernels for the EML scenario and a mean tropical ocean atmosphere are compared to estimate the retrieval's vertical resolution and its dependence on the atmospheric state.

Table 1: Characterisation metrics of moisture anomalies, their definitions and short descriptions. $\mathrm{VMR}_{\mathrm{H_2O,ref}}$ denotes the reference water vapor profile.

Metric	Definition	Description
Bounds	z_{bot}, z_{top}	Lower and upper altitude bounds of the anomaly.
Thickness	$\Delta z_{\mathrm{anom}} = z_{\mathrm{top}} - z_{\mathrm{bot}}$	Altitude interval of the anomaly.
Strength	$s_{\mathrm{anom}} = \frac{1}{z_{\mathrm{top}} - z_{\mathrm{bot}}} \int_{z_{\mathrm{bot}}}^{z_{\mathrm{top}}} (\mathrm{VMR}_{\mathrm{H_2O}} - \mathrm{VMR}_{\mathrm{H_2O,ref}})\, \mathrm{d}z$	Mean anomalous $\mathrm{VMR}_{\mathrm{H_2O}}$ within the anomaly.
Height	$z_{\mathrm{anom}} = \frac{\int_{z_{\mathrm{bot}}}^{z_{\mathrm{top}}} z(\mathrm{VMR}_{\mathrm{H_2O}} - \mathrm{VMR}_{\mathrm{H_2O,ref}})\, \mathrm{d}z}{\int_{z_{\mathrm{bot}}}^{z_{\mathrm{top}}} (\mathrm{VMR}_{\mathrm{H_2O}} - \mathrm{VMR}_{\mathrm{H_2O,ref}})\, \mathrm{d}z}$	Weighted mean altitude of the anomaly.

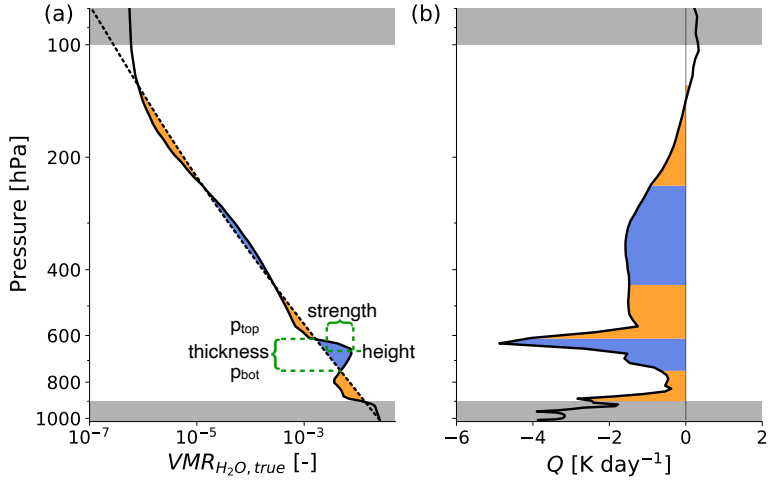

Figure A.3: Humidity profile (a) of an atmospheric case with a strong EML and the associated net heating rate (longwave + shortwave) profile (b). The reference humidity profile used to identify humidity anomalies is depicted as the dashed line in (a). Layers of moist anomalies are highlighted by blue shading, dry anomalies by orange shading. Anomalies that intersect with the grey shaded regions are excluded to restrict anomalies to the free troposphere. The green lines and brackets conceptually display the definition of moisture anomaly characteristics from Table 1 for the strong positive anomaly at around 650 hPa.

A.4.1 *Importance of temperature information to retrieve a moist layer*

We assess the possiblity whether a lack of independent temperature information can cause the EML to not be resolved by running our retrieval in slighlty altered setups. Each row of panels in Figure A.4 represents a variation of the retrieval. The setup introduced in Sect. A.2 is used for the first row and serves as a basis for the other two setups. We refer to this setup as retrieval setup 1. Retrieval setup 2 (Fig. A.4, second row) only deviates from retrieval setup 1 by using the more narrow spectral region that was used by Lacour et al. (2012) and Stevens et al. (2017), which is limited to 1193 to 1223 and 1251 to 1253 cm^{-1}. Retrieval setup 3 (Fig. A.4, third row) only deviates from retrieval setup 2 by omission of the temperature retrieval and instead setting the a priori temperature to the true reference state. The profiles that the synthetic observations are based on are denoted as "true" and the same for all retrieval setups. Based on these profiles, forward simulated synthetic IASI observations are calculated, synthetic Gaussian noise is added (see Sect. A.2.5) and the retrieval is performed. As a technical note, we extrapolate the dropsonde profiles (launched at about 350 hPa) into the upper troposphere and above by fitting a tropical mean atmospheric state (Anderson et al., 1986). We fit these profiles onto a 137 level vertical pressure grid of the ECMWF IFS

model atmospheres that also come with an associated altitude grid (Eresmaa and McNally, 2014).

As a note on comparability of our results to Stevens et al. (2017), we want to be cautious. There are several differences in the exact way the retrieval is setup, e.g. in the assumed a priori states and covariances, the iteration scheme (Gauss-Newton vs. LM) and also the radiative transfer model (Atmosphit vs. ARTS). Besides, our study is conducted in a synthetic framework, since we aim to assess the retrieval of EMLs more fundamentally than the discussed case studies did up to now. With this in mind, we tried to seek out a retrieval feature of the study of Stevens et al. (2017) that is capable of masking the EML in our setup. This feature is the used spectral region that is closely tied to the temperature information content as we want to show in the following.

Looking at the retrieval results of Fig. A.4, the EML structure is found to be resolved well with retrieval setup 1 while retrieval setup 2 misses the EML almost completely, comparable to the results of Stevens et al. (2017). We hypothesize that the missing EML with retrieval setup 2 is caused by the fact that with the limited spectral setup, there is no sufficient independent temperature information available for the retrieval to separate the moisture from the temperature signal, causing large retrieval errors in both quantities. While other previous retrieval studies deliberately try to account for this issue by deploying either a simultaneous retrieval approach (Irion et al., 2018; Smith et al., 2012; Weisz et al., 2013) or a sequential retrieval approach (Smith and Barnet, 2019, 2020; Susskind et al., 2014), we want to highlight the importance of doing so, specifically in an EML scenario.

We find that the large water vapor and temperature errors obtained with retrieval setup 2 around the EML altitude compensate radiatively. While the underestimated humidity at the EML altitude yields an increased spectral radiance in the used water vapor band due to a lower emission height associated with a higher emission temperature, the underestimated temperature yields a decreased spectral radiance. Since this compensation leads to comparatively low y-costs in the OEM scheme, it explains why retrieval setup 2 finds an optimal solution that is associated with relatively large retrieval errors in both temperature and water vapor.

We introduce retrieval setup 3 to exclude the possibility that resolving the EML with retrieval setup 2 is simply limited by vertical resolution of the moisture retrieval, e.g. limited humidity information content. The retrieval results of retrieval setup 3 show that with a perfect prior temperature profile also the limited spectral range is sufficient to resolve the general EML structure, albeit with reduced EML amplitude. Hence, the EML blindspot of retrieval setup 2 and possibly of Stevens et al. (2017) is a consequence of the ambiguity

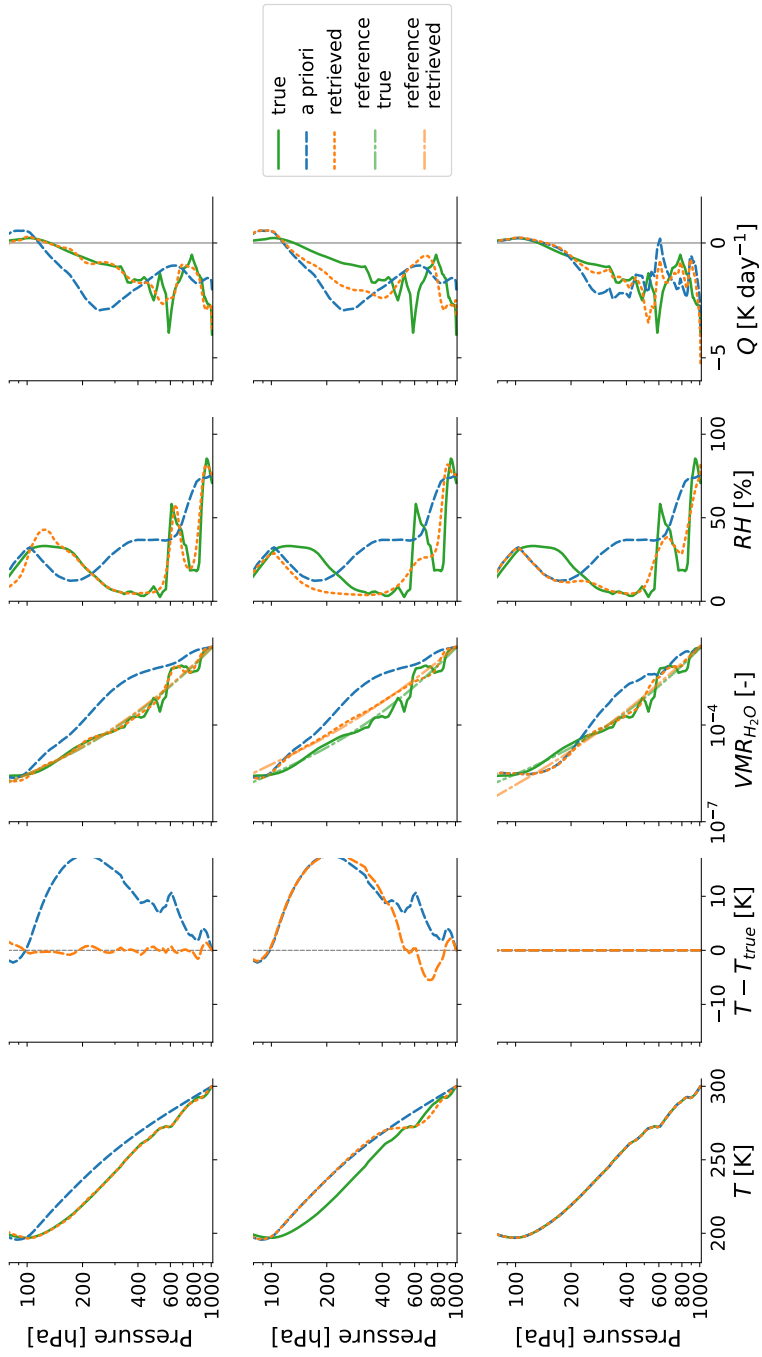

Figure A.4: Columns show profiles of temperature (T), temperature differences of a priori and retrieved state to the true state, VMR_{H_2O}, relative humidity (RH) and net heating rates (Q) for the dropsonde profiles that sampled the EML discussed by Stevens et al. (2017) (labeled as "true" here). Displayed are the true states that are used as a basis for the forward modelled synthetic IASI observation, the a priori states of the retrieval and the retrieved states. The VMR_{H_2O} reference profiles defined in Sect. A.3 are also depicted. Rows show retrieval results based on different retrieval setups that are introduced in the text.

that lies in the limited spectral range with respect to temperature and water vapor.

To exemplify the concept of the moisture anomaly identification and characterisation method introduced in Sect. A.3 we apply the procedure to this case study and present the derived EML characteristics for each of the different retrieval setups in Table 2. To identify the EML centered around 650 hPa in the true and retrieved profiles in Figure A.4 we introduce the respective reference profiles against which positive VMR_{H_2O} anomalies can be identified. While retrieval setup 1 and 3 yield a moisture anomaly that can be characterised by our method and compared to the characteristics of the true EML, retrieval setup 2 does not show a positive moisture anomaly around 650 hPa.

Table 2 shows that the EML in the true state is centered around 3.6 km altitude and has a vertical extent of 2.3 km. Retrieval setup 1 captures these characteristics reasonably well while retrieval setup 3 shows a strongly overestimated EML thickness of about 3.7 km, reflecting stronger smoothing caused by the limited spectral range used in this setup. Both retrieval setups show a slightly increased EML height when compared to the true state of about 200 m for reasons we can only speculate on. We could see this being a systematic effect caused a less pronounced effect of smoothing at the EML bottom due to higher optical density than aloft. Since the atmosphere is optically more dense near the surface, smoothing may smear the EML over a larger altitude interval at the top than at the bottom, positively biasing the EML altitude in the retrieval.

Table 2: Moisture anomaly characteristics of the EML shown in Fig. A.4. This table is analogous to Table 1, where the exact definitions of the different metrics are explained. The EML characteristics displayed here are calculated for the true state and the retrieval results of retrieval setup 1 and 3, corresponding to upper and lower rows of Fig. A.4, respectively. Retrieval setup 2 does not feature a moisture anomaly object as defined in Sect. A.3.

Metric	Variable name	True state	Retrieval setup 1	Retrieval setup 3
Bounds	z_{bot}, z_{top}	2.5 km, 4.8 km	3.0 km, 5.1 km	2.3 km, 6.0 km
Thickness	Δz_{anom}	2.3 km	2.1 km	3.7 km
Strength	s_{anom}	$2.8 \cdot 10^{-3}$	$2.2 \cdot 10^{-3}$	$1.1 \cdot 10^{-3}$
Height	z_{anom}	3.6 km	3.8 km	3.8 km

While the EML strength s_{anom} may appear as the least trivial moisture anomaly characteristic, being without units due to its defini-

tion based on VMR_{H_2O}, it becomes more intuitive when values are put into relation to each other. The true EML strength of $2.8 \cdot 10^{-3}$, which reflects the mean anomalous VMR_{H_2O} within the EML, is about about 30 % greater than the EML strength derived from retrieval setup 1 and about 2.5 times greater than the EML strength derived from retrieval setup 3. This reflects the notion that while retrieval setup 1 is able to resolve the EML well, retrieval setup 3 yields a strongly smoothed EML that is significantly less pronounced than its true counterpart.

We conclude that while the EML investigated by Stevens et al. (2017) does not appear to pose a general blind spot for hyperspectral IR satellite observations, we are able to find a retrieval configuration that reproduces a similar result as theirs. The deciding property of that configuration is the lack of independent temperature information, which in an EML scenario can yield radiatively compensating errors in temperature and water vapor. With retrieval setup 1 on the other hand, we present a retrieval setup that is able to capture both temperature and humidity profiles well, including the EML, which is in line with other OEM based moist layer case studies (Calbet et al., 2006; Zhou et al., 2009).

A.4.2 *Retrieval resolution*

With OEM, a more quantitative estimation of vertical retrieval resolution can easily be deduced by aid of the averaging kernel matrix $\mathbf{A}$ (Rodgers, 2000). The rows of $\mathbf{A}$ describe the response of the retrieved state to a perturbation in the true state, taking into account the specifications of the observing system. The averaging kernels presented here are based on the spectral setup and a priori assumptions introduced in Sect. A.2.

Several previous studies showed IASI averaging kernels for mean atmospheric states (Lerner, 2002; Schneider and Hase, 2011; Smith and Weisz, 2018). Here we want to highlight the dependence of vertical resolution on the atmospheric state by contrasting the averaging kernels of a tropical mean atmosphere to the reference EML case discussed in the previous subsection. Smith and Barnet (2020) also considered the dependence of $\mathbf{A}$ on the atmospheric state, which they find can be quite severe. In contrast to their more general study, we want to focus on comparing the variability of $\mathbf{A}$ with respect to a well characterised mean and EML state. While we focus on discussing the water vapor averaging kernels in this section, similar conclusions can be made about the temperature averaging kernels which are appended in Appendix A.8.1.

Figures A.5(a) and (c) depict the rows of the H_2O averaging kernel matrix as colored lines for two different atmospheric setups. The more blue lines correspond to kernels closer to the surface, while the more yellow lines correspond to kernels higher up in the atmosphere.

Figures A.5(a) and (b) are based on an average tropical ocean atmosphere, namely the tropical FASCOD atmosphere introduced in Sect. A.2.5. Figures A.5(c) and (d) only differ in their base atmospheric state by the introduced EML, as described in Sect. A.3. The vertical width of a kernel is a measure of the retrieval's vertical resolution in a specific height, which is shown in terms of Full Width at Half Maximum (FWHM) of the respective kernels in Fig. A.5(b) and (d). A measure for the retrieval's ability to detect and respond to a water vapor disturbance in the true state in a given height is the measurement response, which is defined as the sum over all kernel rows and depicted as the black line in Fig. A.5(a) and (c). Values close to unity indicate that the retrieval is sensitive to disturbances in the true profile (Rodgers, 2000).

The averaging kernels of the mean tropical ocean atmosphere in Fig. A.5(a) expectably show a very smooth behaviour with height and the deduced vertical resolution is similar to that of Smith and Weisz (2018), e.g. it is on the order of 1.5 km throughout the free troposphere between around 200 to 800 hPa. In the upper troposphere ($p \lesssim 200$ hPa) a significant decrease in vertical resolution is found. In the boundary layer, the vertical resolution does not appear to diminish, but to improve, which is in agreement with Smith and Weisz (2018). However, we find this to be misleading because the shape of the averaging kernels associated with these altitudes is distorted due to the strong signal of the surface, not allowing for a robust calculation of the FWHM. Rather than the FWHM, the measurement response is a more informative measure of the retrieval's sensitivity to disturbances in the boundary layer. For the tropical ocean atmosphere, the measurement response is close to unity throughout most of the free troposphere and shows a sharp decrease within the boundary layer, indicating limited sensitivity to water vapor disturbances in the true state only in the boundary layer.

The EML has a significant impact on all averaging kernels in the lower and mid troposphere as shown in Fig. A.5(c) and (d). Around the humidity maximum at the EML top the averaging kernels show distinct peaks, which are caused by the strong radiative signal associated with the EML. The EML signal is so strong that it also affects the more sensitive channels that usually sample higher altitudes and therefore decreases the vertical resolution from about 1.5 km to 2.5 km between the EML top and about 200 hPa compared to the tropical mean atmosphere. As the moisture decreases beneath the EML humidity maximum, a clear reduction in vertical resolution down to about 2.5 km at around 800 hPa is found, indicating a more limited ability to resolve additional moisture features beneath the EML. This state dependence of the averaging kernel reflects the nonlinear nature of the retrieval problem and the limited expressiveness of the vertical resolution deduced with this method. Retrievability of a moisture fea-

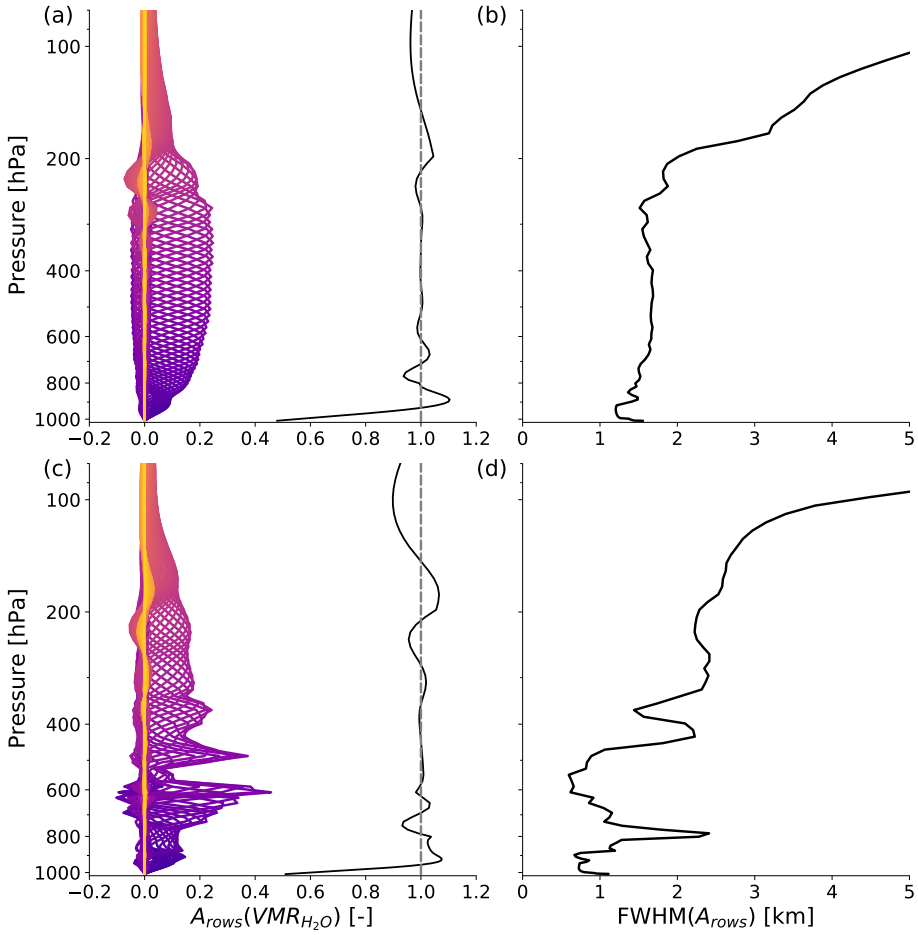

Figure A.5: (a) and (c) show rows of the water vapor averaging kernel matrix ($A_{\text{rows}}(\text{VMR}_{\text{H}_2\text{O}})$) as colored lines and their sum as a black line, which denotes the measurement response. The rather blue lines correspond to kernels closer to the surface, the more yellow lines correspond to kernels in higher altitudes. (b) and (d) show the FWHM of the averaging kernel rows, which is a measure for the vertical resolution of the observing system. (a) and (b) are based on a mean tropical ocean atmosphere, specifically the tropical FASCOD atmosphere. The atmospheric setup used for (c) and (d) differs only by the introduction of EML features, as described in Sect. A.3.

ture not only depends on its vertical extent, but on the atmospheric state it is embedded in. This motivates the statistical analysis presented in the next section of analysing the retrieval's performance with regard to its ability of capturing moisture anomalies as introduced in Sect. A.3.

A.5 RETRIEVAL PERFORMANCE

After the exemplified investigation of an EML case in the previous section, the retrieval performance is now assessed based on a larger

test dataset. The major aim with this section is to first assess the validity of our simple retrieval setup, before using the synthetic retrieval dataset in the next section to showcase some of the possibilities with our new method for identifying and characterising moisture anomalies introduced in Sect. A.3. In the following, we first introduce the test dataset and investigate the vertical distribution of the retrieval error in temperature and water vapor. Afterwards, the smoothing error, which is an intrinsic source of error for a given observing system and a set of a priori assumptions, is calculated and discussed in the context of the overall retrieval error.

A.5.1 *Reference dataset and retrieval error*

The retrieval is applied to tropical ocean atmospheres (between 30° S to 30° N) that are part of the ECMWF IFS diverse profile database made available by Eresmaa and McNally (2014). The database consists of 25,000 short-range forecasts, which are divided into five even subsets that focus on representing diversity in a particular atmospheric quantity, such as temperature, specific humidity or precipitation. For the purpose of this work, only the tropical ocean atmospheres of the subset that focuses on a diverse sampling of specific humidity is considered. This yields a total number of 1599 atmospheric setups, for 1288 of which the retrieval converges to a solution. The following analysis is based on these converged cases.

A statistical overview of the variability of temperature and humidity profiles covered by the tropical ocean dataset is provided in Fig. A.6(a), (b) and (c). The temperature profiles show very limited variability, as is typical for tropical ocean regions. However, despite this very smooth appearance of the vertical temperature structure, the individual profiles do include significant temperature inversions, for example the very prominent inversion in about 2 km height in the trade wind region (not shown). The humidity profiles show weak variability within the boundary layer, where the ocean acts as a humidity source and humidity is mostly set by the saturation vapor pressure controlled by temperature. The median RH is about 82 % at the surface and reaches its maximum in about 500 m height in the transition to the shallow cloud layer. In the free troposphere, the typical "C" shape structure of the RH profile is followed (Romps, 2014). An interesting feature in the 75th and 90th percentiles of the RH profiles is the presence of positive RH anomalies in the layer between around 500 and 700 hPa, indicating moisture anomalies that may be tied to the freezing level.

Figures A.6(d), (e) and (f) show an overview of the retrieval's deviations from the reference dataset, from now on referred to as the retrieval error. In the context of these figures, the term bias refers to a difference of the median values of the retrieved and the true datasets.

The temperature profile shows a positive bias close to the surface, which we attribute to the limited signal from these heights in the satellite observation. The negative bias near the surface in RH is associated with this positive temperature bias and with the slightly negative VMR_{H_2O} bias near the surface. Between around 900 to 700 hPa the VMR_{H_2O} and RH biases are positive, while the temperature bias is slightly negative. This positive moisture bias in the lower troposphere is associated with an increased variability of the error, particularly towards strong positive errors that indicate an overestimation of moisture in the lower troposphere by the retrieval. This may be caused by the typical hydrolapse that is coupled to the trade inversion in the trade wind regions, which can in its sharpness not be captured by the retrieval.

In the mid troposphere between about 700 to 300 hPa, which is where typical EMLs are expected, no significant temperature or humidity biases are found. A positive skewness in the VMR_{H_2O} error distribution towards strong positive errors is found, indicating that positive errors in retrieved VMR_{H_2O} are rare, but large compared to the negative errors that occur. As an explanation for this error pattern, we propose the idea that positive (moist) moisture anomalies tend to be captured with a slight underestimation in their strength, while occasionally strong negative (dry) moisture anomalies beneath are associated with a strong overestimation of moisture by the retrieval due to a lack of signal beneath a positive moisture anomaly (as shown in Fig. A.5). This could explain less frequent but strong positive retrieval errors and more frequent, but relatively weak negative errors that have a net bias close to zero.

In the upper troposphere errors in temperature and humidity are generally larger. We believe that this has two causes. Firstly, the a priori moist adiabatic temperature assumption becomes worse closer to the tropopause. Secondly, Fig. A.5 shows that there is only a weak radiative signal from the upper troposhere as indicated by strongly smoothed averaging kernels and a decreased vertical resolution. While this may be improved by adjusting the a priori assumptions for the upper troposphere and including even stronger absorption features of water vapor, the upper troposphere is no major concern of this study.

A.5.2 *Smoothing error*

Part of the retrieval error shown in Fig. A.6 can be attributed to the so called Smoothing Error (SE, Rodgers 2000). Given a specific observing system and a priori assumptions about the quantity to be observed, the SE is a source of error that can not be avoided without changing the observing system or a priori assumptions themselves. In the frame of the averaging kernel matrix, the SE expresses the error in

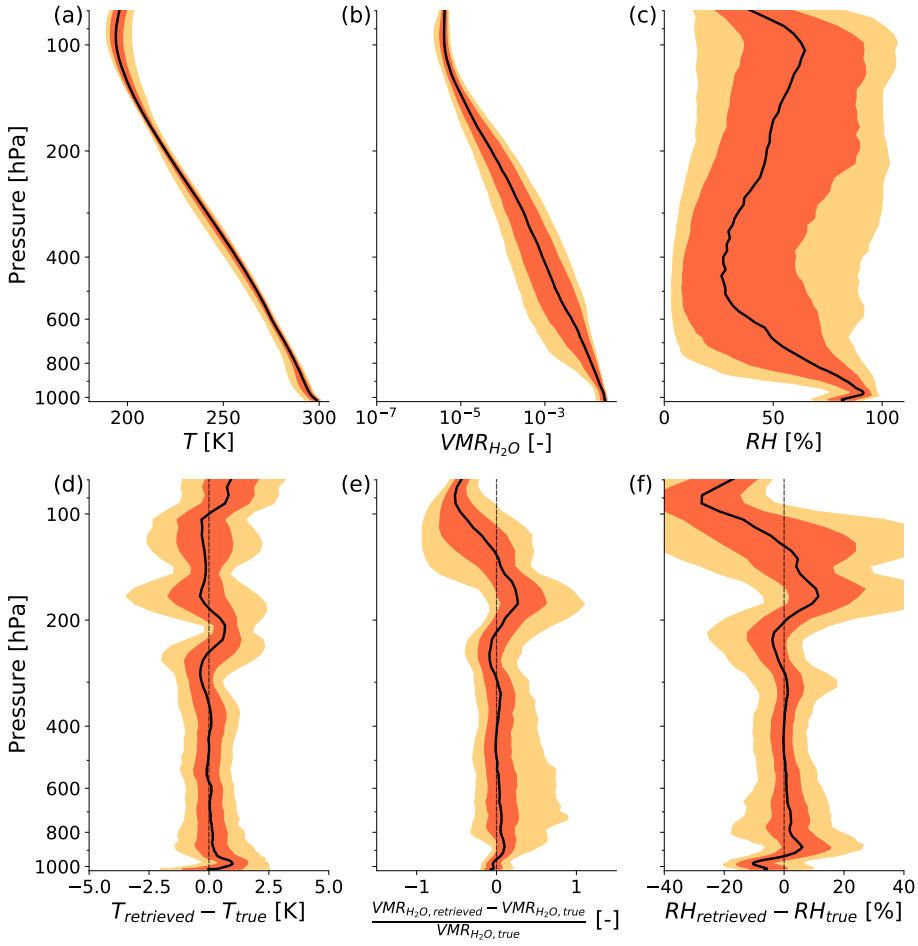

Figure A.6: (a), (b) and (c) give a statistical overview of temperature, VMR_{H_2O} and RH over 1288 tropical ocean model atmospheres from the dataset of Eresmaa and McNally (2014), upon which the retrieval is performed. Color scheming is based on Figure 5 of Eresmaa and McNally (2014), where bright orange indicates 10th and 90th percentiles, dark orange indicates 25th and 75th percentiles. The median is depicted by a solid black line. (e), (f), (g) show the respective statistics on the deviations of the retrieved to the true profiles. Note the exception of relative differences for VMR_{H_2O}, which is more suited for the dynamical range of this quantity.

the retrieval that is associated with the non-delta-function shape of the averaging kernel rows (see Fig. A.5) and the thereby limited ability to resolve vertical features. Here, it is calculated as

$$\vec{SE} = (\vec{x} - \vec{x}_a)(\mathbf{A} - \mathbf{I}_n) \tag{A.4}$$

where $\mathbf{I}_n$ denotes the identity matrix of order n and n is the number of vertical levels of the profile retrieval.

Figure A.7 shows the SE statistics associated with the retrieved temperature and humidity profiles of the tropical ocean dataset. The

median of the SE with respect to the temperature profile (SE(T)) is close to zero throughout most of the free troposphere, similar to the retrieval bias shown in Fig. A.6(d). The positive retrieval bias in temperature found near the surface is with smaller magnitude also found in SE(T), indicating that this pattern is caused by a systematically unresolved vertical feature. The variability of the temperature retrieval error found in Fig. A.6(d) in the lower and mid troposphere cannot be attributed to smoothing, since the variability in SE(T) is very small. In conclusion, this indicates that temperature error sources are unlikely to be caused by uncaptured vertical temperature variability, but rather vertically constant errors, which do not show up in SE(T). In the upper troposphere, SE(T) increases towards the tropopause where smoothing becomes the major contribution to the retrieval temperature error.

For the water vapor profile in the lower and mid troposphere, smoothing is a greater source of error than for the temperature profile (Fig. A.7b). While the median of the water vapor smoothing error ($SE(\log(VMR_{H_2O}))$) is low throughout the lower and mid troposphere, its variability (e.g. the shown percentile ranges) is on similar scale as the variability of the retrieval error shown in Fig. A.6(e). This indicates that a major contribution of error in the water vapor retrieval is to capture vertical variability. The distribution of $SE(\log(VMR_{H_2O}))$ in the mid troposphere also reflects the positive skewness that was found in the overall error in Fig. A.6(e). This is consistent with the previously described idea that this skewness is linked to the retrieval's ability of capturing vertical moisture anomalies. In the upper troposphere, the median $SE(\log(VMR_{H_2O}))$ increases to a similar magnitude as the retrieval error, while its variability even exceeds that of the retrieval error, indicating that other sources of error are compensating.

The SE(RH) statistics show the combined effect of the smoothing errors in temperature and humidity (Fig. A.7c). It is apparent that also in terms of RH the smoothing error has a strong contribution to the retrieval error in the lower and mid troposphere, similar to the VMR_{H_2O} error. In the upper troposphere the median SE(RH) is on the same order as the retrieval error, while its variability appears to be even stronger, following the behaviour found for $SE(\log(VMR_{H_2O}))$.

A.6 RETRIEVAL OF MOISTURE ANOMALIES

In this section the retrieval results for the previously introduced tropical ocean test dataset (Sect. A.5) are assessed with specific focus on the characteristics of moisture anomalies as introduced in Sect. A.3. First, the moisture anomaly characteristics of the tropical ocean dataset and of the retrieved dataset are compared to look for systematic limitations of the retrieval to resolve specific kinds of moisture

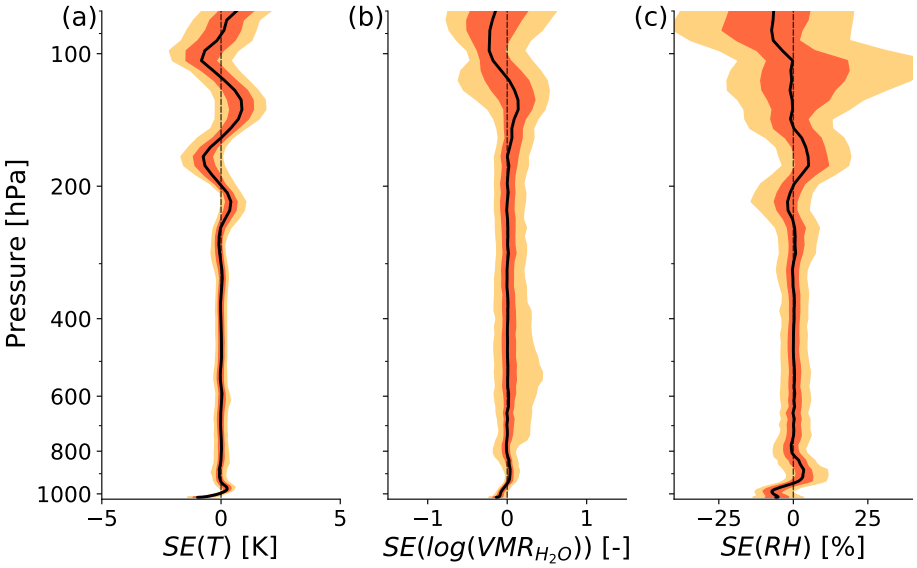

Figure A.7: Smoothing Error (SE) as calculated by Eq. A.4 of retrieved temperature (a), logarithmic VMR_{H_2O} (b) and RH (c) profiles over 1288 tropical ocean atmospheres. Lines and shadings are defined as in Figure A.6.

anomalies. Then, the impact of moisture anomalies on the heating rate profile is assessed and the retrieval's ability to capture this impact is investigated.

A.6.1 *Moisture anomaly characteristics*

Figure A.8 shows probability density distributions of the moisture anomaly characteristics (defined in Sect. A.3) for the tropical ocean dataset (green) and the associated retrieved dataset (orange). The dashed lines indicate the mean values of the respective distributions. The distributions of moisture anomaly height (z_{anom}) displayed in Fig. A.8(a) show that most moisture anomalies occur in the mid to upper troposphere, which is somewhat surprising since EMLs are typically thought to be coupled to the freezing level in around 5 km height (Johnson et al., 1996; Stevens et al., 2017). However, note firstly that strong EMLs and very slight moisture anomalies are treated evenly here. Secondly, the distributions reflect the statistics of the underlying dataset, which is based on the ECMWF IFS atmospheric model. This dataset appears as a suitable starting point to assess the retrieval's ability to capture moisture anomalies, however, the analysis of the dataset's moisture anomaly statistics themselves are not the focus of this study.

Figure A.8(a) shows a bias between true and retrieved z_{anom} of about 0.9 km, indicating that the found the z_{anom} biases in the case study of Sect. A.4 do indeed appear to be systematic and even greater in amplitude. Besides the earlier proposed cause of a varying effect of

smoothing with height, we believe this bias is also caused by a systematic underestimation of the fraction of moisture anomalies below 5 km altitude by the retrieval, while the fraction of anomalies above 10 km is overestimated. Only a fraction of about 52 % of the total number of moisture anomalies below 5 km in the reference dataset is captured by the retrieval. We attribute this deficiency to the fact that moisture anomalies are typically more narrow in the lower to mid troposphere than further aloft, as shown in Fig. A.9.

Figure A.9(a), (b) and (c) show the number of moisture anomalies of the reference dataset in the lower, mid and upper troposphere, respectively, as a function of anomaly width (Δz_{anom}) and separated into subsets of anomalies that either could or could not be retrieved. An anomaly of the reference dataset is considered retrieved, if there is a retrieved positive moisture anomaly with an anomaly height within the vertical bounds of the anomaly of the reference dataset. While it is apparent that the more narrow moisture anomalies are most frequently missed in all three altitude regions, this means a particular shortcoming for the retrieval between 0 to 5 km because cases with $\Delta z_{\text{anom}} \gtrsim 2\,\text{km}$ are especially rare. A technical cause for this is the fact that we exclude all anomalies that reach as close to the surface as 900 hPa (see Sect. A.3). However, the lower to mid troposphere also is subject of more small-scale variability due to its link to the boundary layer and low level convection, making it more prone for small scale moisture anomalies than the free troposphere aloft.

The distribution of the moisture anomaly strength (s_{anom}) depicted in Fig. A.8(b) has a similar dynamical range as VMR_{H_2O} since the anomalous VMR_{H_2O} scales with its absolute value. The distribution of s_{anom} of the retrieved dataset is overall shifted towards lower values yielding a negative bias of about $-8.2 \cdot 10^{-5}$ (17 %) against the reference dataset, which can mostly be attributed to the smoothing error of the retrieval. The smoothing error generally acts by a weakening and thickening of anomalies, which also partly explains the significant positive bias of about 0.4 km (15 %) in moisture anomaly thickness (Δz_{anom}) depicted in Fig. A.8(c). Another contributing effect towards the found biases in s_{anom} and Δz_{anom} is the fact that particularly weak and narrow moisture anomalies are more often completely missed by the retrieval as shown by Fig. A.9.

A.6.2 *Implications of moisture anomalies for the heating rate profile*

Moisture anomalies affect the heating rate profile by absorbing and emitting IR radiation. Because of the exponential decrease of water vapor with height, emission at the anomaly top is particularly efficient and can yield a strong local radiative cooling rate (see Fig. A.3). We consider this cooling effect to be the moisture anomaly's most prominent footprint on the heating rate profile. In the following, we

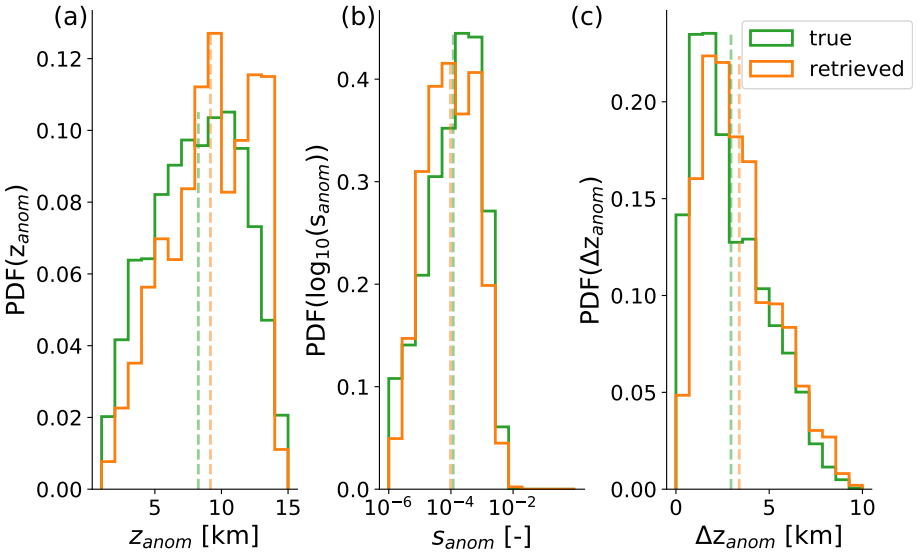

Figure A.8: Probability density functions (PDFs) of moisture anomaly characterstics of the tropical ocean reference dataset (denoted as "true") and the retrieved dataset.

quantify this cooling effect by considering the minimum heating rate within the vertical bounds of a moisture anomaly, $\min(Q_{anom})$. Since $\min(Q_{anom})$ is a scalar metric, it can intuitively be viewed as a function of moisture anomaly characteristics.

Figure A.10(a) and (b) show the joint frequency distributions of the moisture anomaly strength (s_{anom}) and $\min(Q_{anom})$ for the tropical ocean dataset and the retrieval dataset, respectively. Both datasets show a clear correlation between the two quantities, namely that stronger anomalies are associated with a stronger peak in radiative cooling. While moisture anomalies with $s_{anom} \lesssim 10^{-4}$ show similar minimum cooling rates down to about -2.5 K day^{-1} in both the reference and the retrieval dataset, larger differences between the two datasets are apparent for stronger anomalies. The reference dataset (Fig. A.10, a) shows $\min(Q_{anom})$ values between about -1 to -5 K day^{-1} for moisture anomalies with $s_{anom} \gtrsim 10^{-4}$, while the retrieval dataset barely shows any $\min(Q_{anom})$ values smaller than -3 K day^{-1}.

We hypothesise that the increased variability in $\min(Q_{anom})$ for $s_{anom} \gtrsim 10^{-4}$ in the reference dataset can be attributed to the variability in the exact vertical shapes of the moisture anomalies. Anomalies with a strong negative moisture gradient at their top yield a stronger minimum in radiative cooling, while more smooth anomalies are associated with a less pronounced radiative cooling peak. This effect introduces more variability in $\min(Q_{anom})$ the stronger the anomalies are. It also explains why retrieved moisture anomalies do not show as extreme $\min(Q_{anom})$ values as the reference dataset, since the vertical shape of retrieved anomalies is always bound by the smoothing error.

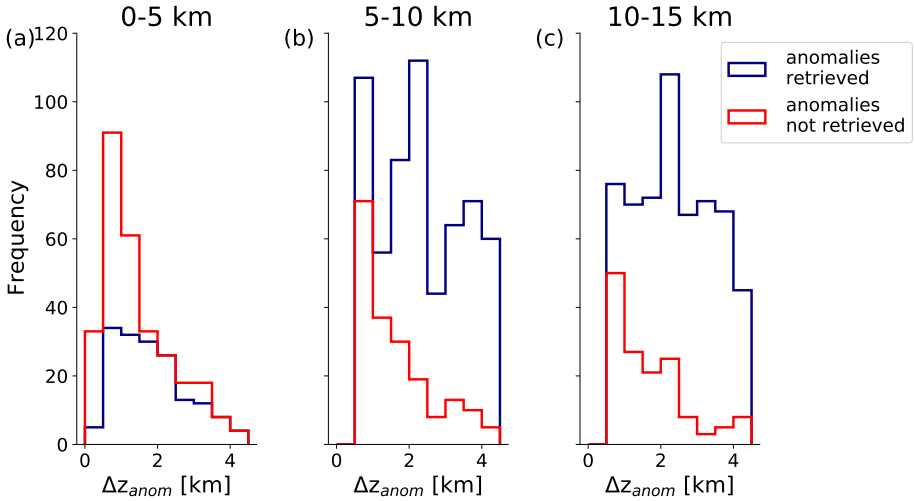

Figure A.9: Frequency distributions of moisture anomaly thickness of the tropical ocean reference dataset, split up into cases where a moisture anomaly could be retrieved and could not be retrieved. (a), (b), (c) reflect three altitude regions, namely the lower (0-5 km), mid (5-10 km) and upper (10-15 km) troposphere.

In the real world, much more extreme vertical moisture gradients associated with moisture anomalies can be observed than in the model based reference dataset used here. Albright et al. (2020) discuss an EML scenario over the Northern Atlantic Trades with a significant moisture drop that is associated with a minimum cooling rate of about 20 K day^{-1}. The results of Fig. A.10 indicate that while the retrieval is able to broadly distinguish between differently strong moisture anomalies and their associated heating rates, it is unable to properly represent such extreme cooling rate minima due to smoothing.

Figures A.10(c) and (d) show the joint frequency distributions of the moisture anomaly strength and height (z_{anom}). A clear relation between s_{anom} and z_{anom} is found in both datasets, namely that anomalies are weaker the higher up they are in the troposphere. We explain this by the dependence of s_{anom} on the absolute humidity, which decreases exponentially with height. Combining this with the relation found between anomaly strength and minimum heating rate, it is clear that the radiatively most significant moisture anomalies occur in the lower to mid troposphere. As pointed out in Sect. A.6.1 when discussing Fig. A.9, the retrieval has particular deficiencies in resolving the rather narrow lower to mid tropospheric moisture anomalies. It is now apparent that this deficiency is particularly relevant, since it affects the strongest and radiatively most significant moisture anomalies. However, the EML testcase investigated in Sect. A.4.1 shows that when the anomaly is relatively strong and the atmosphere aloft has a simple structure, also lower to mid tropospheric moisture anomalies can be retrieved well. It may be worth investigating different cases of

EMLs that are embedded in a more complex tropospheric humidity structure in the future.

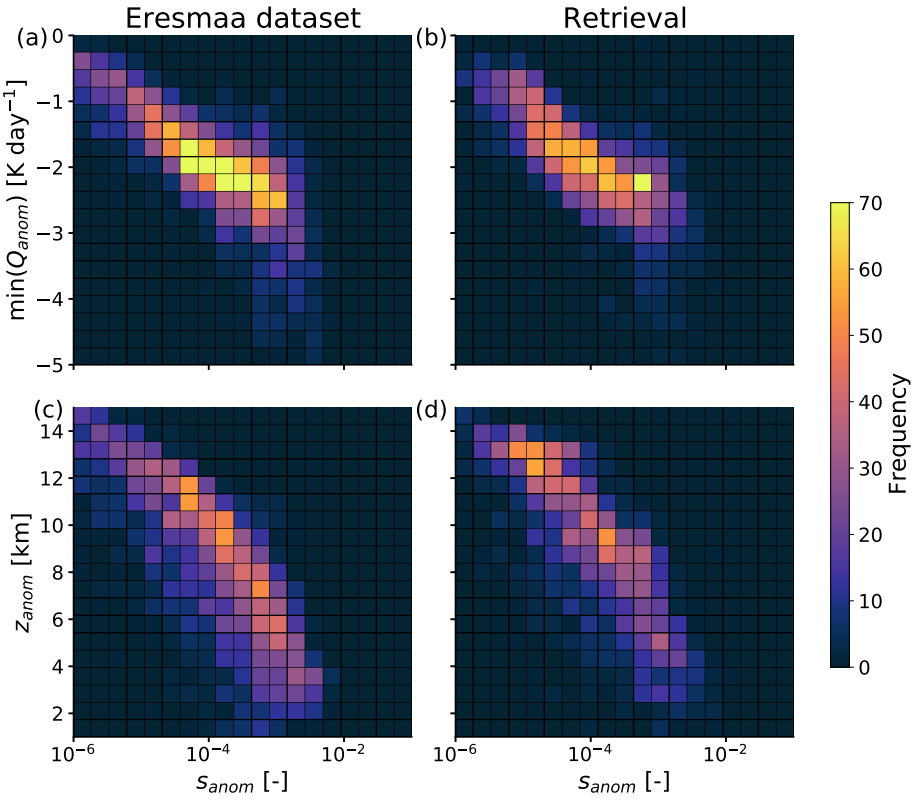

Figure A.10: (a) and (b) show the joint frequency distributions of anomaly strength and minimum heating rate within the anomaly layers of the reference dataset and the retrieved dataset, respectively. (c) and (d) show the joint frequency distributions of the anomaly strength and the anomaly height for the two respective datasets.

A.7 SUMMARY AND CONCLUSIONS

The question implicitly raised by the findings of Stevens et al. (2017), whether or not passive satellite retrievals are capable of resolving EMLs, is investigated based on a synthetic retrieval framework where the IASI instrument is represented by the forward model ARTS. An EML testcase based on dropsonde profiles from the NARVAL-2 measurement campaign (Konow et al., 2019) and a set of 1288 tropical ocean model atmospheres are used as input for the forward model and as a reference to evaluate the retrieval results against. The scenes are limited to clear sky.

To characterise an EML quantitatively (e.g. by strength, thickness and height), the concept of a moisture anomaly against a loosely fitted but clearly defined reference humidity profile is introduced. Following the ideas of Johnson et al. (1996) and Stevens et al. (2017) about

a coupling of EMLs to the freezing level, EMLs would in this framework constitute a subset of rather strong, vertically confined, lower to mid tropospheric positive moisture anomalies. However, for the scope of this work no clear specification of what distinguishes an EML from other moisture anomalies is attempted, which would require a more dedicated selection and analysis of the test dataset. Instead, the aim of this study is a first systematic evaluation EML retrievability based on hyperspectral IR observations.

Based on the EML case of Stevens et al. (2017), we show that with sufficient independent temperature and water vapor information, a combined retrieval of the moisture and temperature profiles and the surface temperature is capable of resolving the vertical EML structure. This result is in line with previous OEM based case studies of similar moisture structures (Calbet et al., 2006; Zhou et al., 2009). We show that limited independent temperature information can cause the EML to not be resolved by the retrieval due to compensating water vapor and temperature errors. We suggest this as a possible reason for the EML blindspot found by Stevens et al. (2017).

The EML signal for the IASI instrument is further characterised by the averaging kernel and the deduced vertical resolution, which is on the order of 1.5 km for an average tropical ocean atmosphere, which is in agreement with previous studies (Lerner, 2002; Smith and Weisz, 2018). However, in the presence of an EML, the strong signal from the EML top weakens the signal from below and introduces a strong gradient in vertical resolution from 0.5 km at the EML top to 3 km at the EML bottom. This state dependence of vertical resolution motivates a statistical approach to evaluate the retrieval's ability of resolving moisture anomalies in various atmospheric states.

When applying the retrieval to the tropical ocean test dataset, it is found that a large fraction of the absolute retrieval error in humidity can be attributed to smoothing. In particular in the transition region between the boundary layer and the free troposphere, the smoothing error introduces a bias to the retrieved humidity and temperature profiles, which is most likely connected to the sharp humidity drop associated with the stratified barrier between the moist boundary layer and the dry free troposphere in the trade wind region. In the free troposphere, say above 800 hPa, the retrieval shows no significant moisture bias, but a positively skewed error variability, indicating that moist anomalies are typically associated with smaller errors than dry anomalies. This is coherent with the idea that dry anomalies that occur beneath moist anomalies are prone to larger errors due to the reduced sensitivity of the satellite measurement below a moist anomaly.

The study is completed by a specific evaluation of the moisture anomaly retrievability based on the new characterisation method introduced in Sect. A.3. It is found that the retrieved moisture anoma-

lies are on average 17 % weaker and 15 % thicker than the anomalies of the reference dataset, which we attribute to smoothing and the fact that rather weak and narrow anomalies are missed by the retrieval more often. While overall about 80 % of the total number of moisture anomalies in the reference dataset are found by the retrieval, a systematic underrepresentation of anomalies below 5 km is found, where the retrieval only identifies about 52 % of the anomalies present in the reference dataset. Since it is shown that moisture anomalies in the lower to mid troposphere are typically the strongest and radiatively most significant, this issue may be quite significant.

The analysis of capturing the moisture anomalies' footprint on the heating rate profiles shows that the retrieval is able to capture the general relation between anomaly strength and minimum cooling rate. However, the retrieval shows a particular shortcoming in capturing the most extreme cooling rates associated with strong lower to mid tropospheric anomalies. We attribute this shortcoming to the retrieval's limited ability of resolving strong vertical moisture gradients that are necessary for the most extreme local cooling rates. Vertical moisture gradients in the real world can be a lot stronger than the ones available from the model test dataset (Albright et al., 2020), which means that retrieval errors with respect to peaks in the cooling rates can be large for rather extreme but realistic cases.

In summary, the retrieval result of the EML case study shows that hyperspectral IR satellite instruments are in principle capable of resolving a sufficiently strong EML in an otherwise simply structured atmospheric profile. The statistical evaluation of retrieved moisture anomaly characteristics shows that the retrieval is able to represent moisture anomlies of various thickness, height and strength. Significant shortcomings are found in the lower to mid troposphere where about half of the moisture anomalies are missed by the retrieval and with regard to capturing particularly strong vertical gradients, causing limitations to resolve extreme cooling rates. It would be interesting to apply a similar analysis to operational retrieval products, such as the IASI L2 product (EUMETSAT, 2017), the NUCAPS product (NOAA Unique Combined Atmospheric Processing System, Berndt et al. 2020) or the CLIMCAPS product (Community Long-term Infrared Microwave Combined Atmospheric Product System, Smith and Barnet 2020). The benefit of our new method for analysing moisture anomalies is that it allows for a direct statistical evaluation of the different product's capabilities to resolve EMLs and vertical humidity structures in general by being easy to apply to large datasets. As a next step we plan to apply our retrieval and evaluation techniques introduced in this work to real hyperspectral IR observations, with focus on EML-like cases that we identify based on dropsonde observations from the NARVAL and EUREC^{4}A (Stevens et al., 2021) measurement campaigns. This may also serve as a good first testbed

of data to assess operational products' capabilities to resolve the vertical moisture structures of interest.

A.8 APPENDIX

A.8.1 *Temperature averaging kernels*

Since we highlight the importance of sufficient independent temperature information to resolve the water vapor structure, Fig. A.11 shows the temperature averaging kernels and deduced vertical resolution based on the retrieval setup introduced in Sect. A.2.

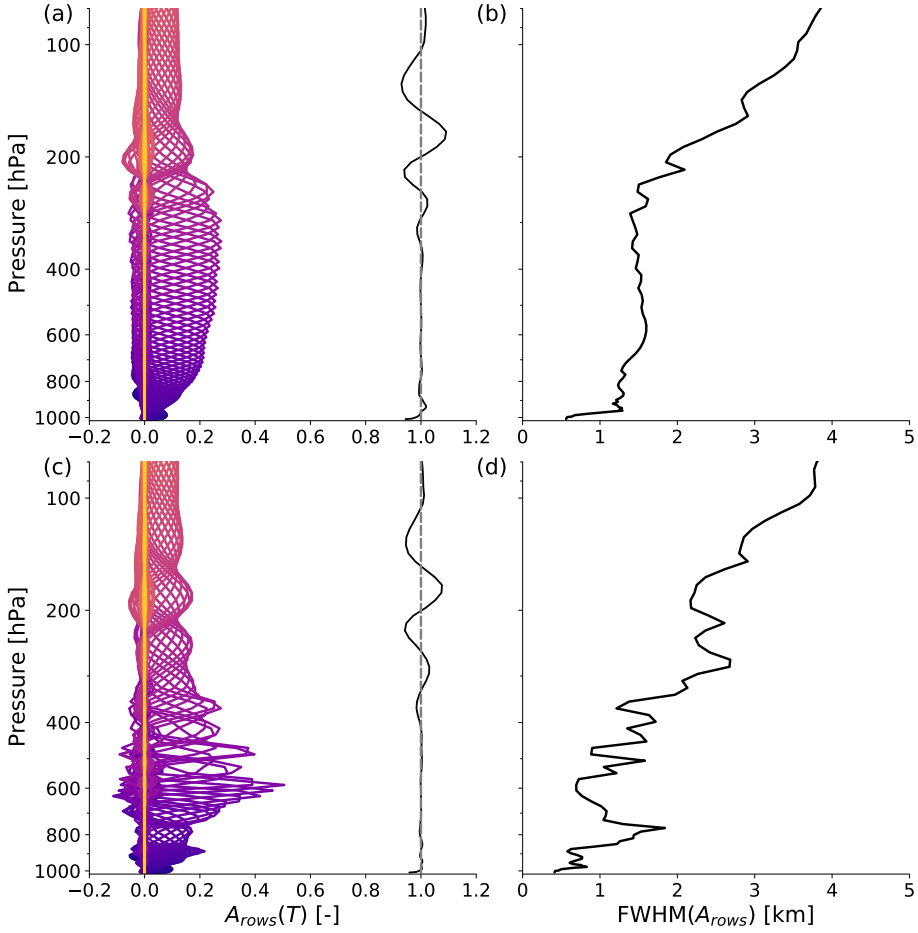

Figure A.11: Same as Fig. A.5, but for temperature.

Code availability The code for the radiative transfer model ARTS, which also includes the module that was used to conduct the OEM retrieval can be found at https://radiativetransfer.org.

Data availability The atmospheric profiles over tropical oceans that were used as a basis for the forward modelled IASI spectra and the spectra themselves are publicly available on Zenodo (Prange et al., 2021b). The atmospheric profiles are a subset of the ECMWF IFS diverse profile database published by Eresmaa and McNally (2014).

Author contributions MP conducted the radiative transfer and the retrieval calculations and prepared the manuscript. MB and SAB supervised the analysis of the retrieval results, contributed ideas to the manuscript and revised it.

Competing interests The authors declare that they have no conflict of interest.

Acknowledgements The authors would like to thank Simon Pfreundschuh, currently at Chalmers University of Technology, for his guidance on the OEM functionality of ARTS. The authors would like to thank Lukas Kluft, currently at the Max Planck Institute for Meteorology in Hamburg, for his guidance on the calculation of heating rates with konrad and for helpful discussions along with Theresa Lang, currently at Universität Hamburg (University of Hamburg). Finally, our thanks go to the ARTS radiative transfer community for their help with using ARTS.

Financial support This work was funded by the German Research Foundation (DFG) in project 'Elevated Moist Layers – Using HALO during EUREC4A to explore a blind spot in the global satellite observing system', project BU 2253/9-1, part of DFG priority programme HALO SPP 1294, project number 316646266. It also is a contribution to the DFG-funded Cluster of Excellence "CLICCS—Climate, Climatic Change, and Society" (EXC 2037, Project Number 390683824), and to the Center for Earth System Research and Sustainability (CEN) of Universität Hamburg.

B

HOW ADEQUATELY ARE ELEVATED MOIST LAYERS REPRESENTED IN REANALYSIS AND SATELLITE OBSERVATIONS?

This chapter contains a paper that is in review in *Atmospheric Chemistry and Physics* as part of a special issue on *Analysis of atmospheric water vapour observations and their uncertainties for climate applications*. It is available as Prange et al. (2022a) at:

Prange, Marc, Stefan A. Buehler, and Manfred Brath (2022). "How adequately are elevated moist layers represented in reanalysis and satellite observations?" In: *Atmospheric Chemistry and Physics*. DOI: https://doi.org/10.5194/egusphere-2022-755.

CONTRIBUTIONS I conducted the processing and the analysis of the data and wrote the manuscript. SAB and MB contributed majorly to the concept and outline of the study and provided useful feedback on earlier versions of the manuscript draft.

How adequately are elevated moist layers represented in reanalysis and satellite observations?

Marc Prange[1,2], Stefan A. Buehler[1], Manfred Brath[1]

[1] *Universität Hamburg, Faculty of Mathematics, Informatics and Natural Sciences, Department of Earth System Sciences, Meteorological Institute, Hamburg, Germany*
[2] *International Max Planck Research School on Earth System Modelling, Hamburg, Germany*

ABSTRACT

We assess the representation of Elevated Moist Layers (EMLs) in ERA5 reanalysis, the IASI L2 retrieval Climate Data Record (CDR) and the AIRS-based CLIMCAPS-Aqua L2 retrieval. EMLs are free tropospheric moisture anomalies that typically occur in the vicinity of deep convection in the tropics. EMLs significantly effect the spatial structure of radiative heating, which is considered a key driver for meso-scale dynamics, in particular convective aggregation. To our knowledge, the representation of EMLs in the mentioned data products have not been explicitly studied, a gap we address in this work. We assess the different datasets' capability of capturing EMLs by collocating them with 2146 radiosondes launched from Manus Island within the Western Pacific warmpool, a region where EMLs occur particularly often. We identify and characterise moisture anomalies in the collocated datasets in terms of moisture anomaly strength, vertical thickness and altitude. By comparing the distributions of these characteristics, we deduce what specific EML characteristics the datasets are capturing well and what they are missing. Distributions of ERA5 moisture anomaly characteristics match those of the radiosonde dataset quite well and remaining biases can be removed by applying a 1 km moving average to the radiosonde profiles. We conclude that ERA5 is a suitable reference dataset for investigating EMLs. We find that the IASI L2 CDR is subject to stronger smoothing than ERA5 with moisture anomalies being on average 13 % weaker and 28 % thicker than collocated ERA5 anomalies. The CLIMCAPS L2 product shows significant biases in its mean vertical humidity structure compared to the three other investigated datasets. These biases manifest as an

underestimation of mean moist layer height of about 1.3 km compared to the three other datasets, a general mid-tropospheric moist bias and an upper tropospheric dry bias. Biases found in the all-sky scenes do not change significantly when limiting the analysis to clear-sky scenes. We calculate radiatively driven vertical velocities ω_{rad} derived from longwave heating rates to estimate the dynamical effect of the moist layers. Moist-layer-associated ω_{rad} values derived from GRUAN soundings range between 2 to 3 hPa hour^{-1} while mean meso-scale pressure velocities from the EUREC^{4}A field campaign range between 1 to 2 hPa hour^{-1}, highlighting the dynamical significance of EMLs. Subtle differences in the representation of moisture and temperature structures in ERA5 and the satellite datasets create large relative errors in ω_{rad} on the order of 40 to 80 % with reference to GRUAN, indicating limited usefulness of these datasets to assess the dynamical impact of EMLs.

B.1 INTRODUCTION

The vertical structure of water vapor in the troposphere is a key driver for meso-scale processes, such as the development and maintenance of convective systems. In particular, it determines the vertical structure of radiative heating due to water vapor's strong ability to absorb and emit infrared (IR) radiation. The spatial structure of radiative heating in the vicinity of convection is capable of driving circulations that contribute to the maintenance of the convection (Muller and Bony, 2015; Muller et al., 2022; Schulz and Stevens, 2018; Wing et al., 2017). Hence, understanding the vertical structure of water vapor is key for our understanding of convective aggregation, which remains a large contributor of uncertainty to climate projections (Bony et al., 2015).

A common meso-scale phenomenon affecting the vertical humidity structure in the tropics are Elevated Moist Layers (EMLs) in the lower to mid-troposphere, which frequently occur either in the vicinity of deep convection or in association with extratropical dry air intrusions (Villiger et al., 2022). EMLs can extend horizontally over several hundred kilometers and have lifetimes of about a day (Johnson et al., 1996; Stevens et al., 2017). In the convection-dominated regions near the intertropical convergence zone (ITCZ), especially over the Western Pacific warmpool, EMLs are particularly common and manifest as a secondary maximum of relative humidity (RH) in the climatological profile near the melting level at around 5 km altitude (Romps, 2014).

It is important to capture EMLs in observational and reanalysis datasets, which serve as reference for modelling studies (Brands et al., 2013; Eyring et al., 2016; Ferraro et al., 2015; Jiang et al., 2012; Lang et al., 2021; Teixeira et al., 2014). In particular, Lang et al. (2021) highlight the importance of reducing uncertainties in clear-sky mid-tropospheric humidity in global storm resolving models that yield significant differences in the models' radiation budgets. Hence, having suitable global and longterm satellite and reanalysis datasets to assess such model differences is of great value.

In a case study, Stevens et al. (2017) found strong limitations of passive satellite based humidity retrievals to resolve an EML, suggesting a somewhat fundamental EML blindspot for such observations. This is particularly surprising for the advanced hyperspectral IR instruments such as AIRS (atmospheric infrared sounder) or IASI (infrared atmospheric sounding interferometer), which offer rich vertical information content about temperature and water vapor. In our recent study (Prange et al., 2021b), we found a physical explanation for the apparent EML blindspot, suggesting that the limited temperature information available with the particular retrieval setup deployed by Stevens et al. (2017) is responsible for the inability to resolve the EML

with IASI. In the same article, we showed that EMLs do not pose an inherent blindspot for hyperspectral IR retrievals based on simulated observations.

In this work we follow up our previous analysis with an evaluation of EMLs in operational hyperspectral IR retrieval products based on the IASI and AIRS instruments. With hyperspectral IR observations being a significant data contribution to reanalysis products (e.g. Cardinali, 2009; Dahoui et al., 2017) we also assess EMLs in ERA5 (ECMWF reanalysis v5). To our knowledge, EMLs have not been explicitly studied based on any of these data products. We address this gap in this study.

The Western Pacific warmpool region is particularly suited to study EMLs because of the frequent occurence of deep convection. Hence, as reference dataset we use the GRUAN (global climate observing system upper air network) radiosondes launched on Manus Island from 2011 to 2014. We collocate the datasets within 50 km in space and 30 minutes in time to make the data directly comparable. We first assess the mean profiles of humidity, temperature and static stability to quantify the mean atmospheric state in the study region for the different datasets. We then apply the moisture anomaly identification and characterization method of Prange et al. (2021b) to statistically quantify the EMLs of the collocated datasets. This method allows for a dedicated comparison of EML characteristics such as EML strength, thickness and height. It also enables a direct quantification of the moisture anomalies' effect on the radiative heating rate, the spatial structure of which is a key driver for the meso-scale dynamics of the atmosphere. We do this quantification by calculating moist-layer-associated radiatively driven vertical velocities, which we compare to meso-scale measurements of pressure velocities from the EUREC^{4}A (elucidating the role of clouds-circulation coupling in climate) field campaign (Stevens et al., 2021).

B.2 DATA

We investigate the vertical moisture characteristics of GRUAN radiosonde data, ERA5 reanalysis and of two satellite retrieval products based on the IASI and AIRS instruments. In the following, we highlight the most important properties of these datasets for the context of this work. This includes brief descriptions of the datasets' spatial and temporal sampling characteristics, a brief summary of their underlying algorithms and our own processing steps. Fig. B.1 provides a spatial overview of the research region and the typical sampling over one day. Note that one processing step we apply to all datasets, except GRUAN, is to filter out datapoints over land to assure homogeneous surface conditions.

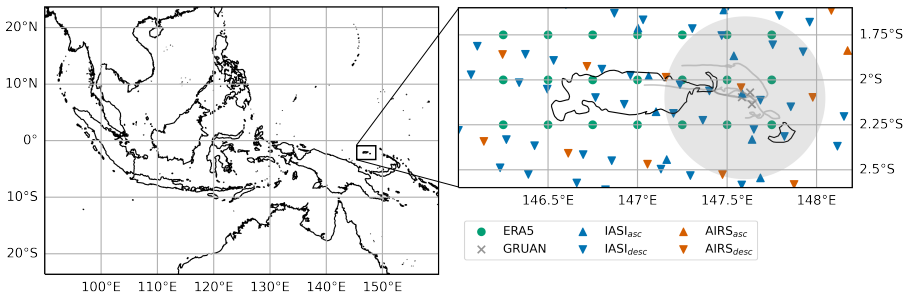

Figure B.1: Maps show the geographical location of Manus Island and spatial sampling over one day (2012-03-28) of the four investigated datasets. The satellite data is split into ascending and descending node data. Radiosonde pathways are shown as lines. Their mean position is indicated by gray crosses that are used as collocation locations. The transparent gray circle visually indicates the collocation radius of 50 km.

B.2.1 *GRUAN radiosondes*

The GRUAN (global climate observing system reference upper air network) measurement program consists of a network of about 30 quality controlled radiosonde measurement sites around the world to detect trends in essential climate variables such as temperature and humidity (Dirksen et al., 2014; Seidel et al., 2009). Here we pick out the GRUAN site on Manus Island, where radiosondes were launched from January 2011 to July 2014, run by the Atmospheric Radiation Measurement program (Ackerman and Stokes, 2003). This is a particularly suited reference dataset for the scope of our work for two reasons. Firstly, Manus Island is located at about 2° S in the Western Pacific warmpool, a region where EMLs are expected to occur frequently due to their link to deep convective events. Secondly, the standard radiosonde launch times at 0 and 12 UTC with a local time shift of UTC + 10 h turn out to coincide well with IASI overpasses at the fixed equator crossing time (ECT) of the MetOp satellites at around 9:30 local time.

The GRUAN sounding data used in this work is obtained from the RS92-GDP.2 data archive. Uncertainty estimates are 6 % for relative humidity (RH) and between 0.15 to 0.6 K for temperature depending on daytime and altitude (Dirksen et al., 2014). When binning the launch times of the full sounding dataset into hourly intervals, about 60 % of the soundings occur around the 0 and 12 UTC launch times. A significant anomaly in radiosonde launch times occured from 24 September 2011 to 31 March 2012 with launches every 3 hours as part of the DYNAMO campaign (Yoneyama et al., 2013).

As a first step of preparing the GRUAN sounding data for our processing, relative humidity values are transformed from being defined with respect to the saturation vapor pressure above water (GRUAN

standard) to a mixed phase approach as described by ECMWF (2018). We then linearly interpolate the sounding dataset to a fixed altitude grid ranging from 0 m at the surface to 15 km altitude at 10 m intervals. In case of missing values in the original data we interpolate over intervals of up to 100 m and leave the missing values for larger intervals. We then deduce H_2O volume mixing ratios (VMRs) from RH, temperature and pressure.

B.2.2 *ERA5*

We use the ECMWF Reanalysis v5 (ERA5) high resolution atmospheric data on a 31 km spaced horizontal grid, on 137 vertical levels and in hourly intervals. Detailed descriptions of spatial and temporal discretisation of ERA5 are provided in the overview paper and in the IFS (version Cy41r2) documentation (ECMWF, 2016; Hersbach et al., 2020).

We use a total of 21 ERA5 pixels around Manus Island as depicted in Fig. B.1. The data is originally stored on a T639 spectral grid or a reduced gaussian grid depending on the variable. We transform the grids of all variables to a 0.25 ° evenly spaced latitude/longitude grid using bilinear interpolation. We deduce H_2O VMR as our main humidity quantity from the specific humidity that is originally provided in ERA5. We deduce altitudes for each ERA5 profile by assuming a hydrostatic atmosphere and using the fixed pressure grid and the temperature profiles as input.

B.2.3 *IASI L2 Climate Data Record*

The IASI Level 2 retrieval dataset used in this work is called the "IASI All Sky Temperature and Humidity Profiles - Climate Data Record Release 1.1 - Metop-A and -B" and is provided by EUMETSAT (2022). We use only data from MetOp-A. We refer to this dataset as the IASI L2 CDR in the frame of this study. The dataset is aimed to be a consistently reprocessed longterm dataset based on the most recent version of the statistical piecewise linear regression (PWLR) EUMETSAT retrieval algorithm. The also available purely operational IASI L2 retrieval data is subject to significant jumps over the years due to algorithm updates (EUMETSAT, 2017). Since the algorithm of the period between 2011 to 2014 is not representative of today's standard, we use the reprocessed IASI L2 CDR.

Details about the IASI L2 CDR are provided in the product user guide (EUMETSAT, 2022). Here we summarize some of its main properties. The retrieval algorithm makes use of IASI spectra and radiances observed by the microwave sounders AMSU-A (Advanced Microwave Sounding Unit-A) and MHS (Microwave Humidity Sounder) onboard of the same satellite to also retrieve information about atmo-

spheric temperature and humidity in the presence of clouds. A retrieval pixel at nadir has a diameter of about 50 km and is made up of a 2×2 array of IASI pixels. To train the PWLR retrieval algorithm, global sensing data of 4 days of each month of the years 2015 and 2016 are matched with ERA5 temperature, humidity and ozone profiles on 137 vertical levels. Cloudy scenes are included in the training step of the algorithm to allow for the retrieval of atmospheric quantities in all-sky scenes. The retrieval is conducted on 137 atmospheric levels and an additional surface level. All-sky retrievals are conducted for atmospheric temperature and specific humidity profiles as well as for surface temperature and total column water vapor. A cloud fraction estimate is also provided based on AVHRR (Advanced Very High Resolution Radiometer) data that is integrated over the retrieval's field of view. The dataset also comes with uncertainty estimates for temperature and humidity profile retrievals that reflect the mean uncertainty of the surface level and the mid-troposphere (EUMETSAT, 2022). These uncertainties are provided in units of Kelvin in temperature and dew point temperature. As recommended in the user guide, we filter cases considered highly defective with uncertainties > 4 K. This filtering only removes about 1 % of data.

The only variable we add in our own processing is the height associated with the retrieval's vertical levels. For this purpose we assume a hydrostatic atmosphere and use profiles of pressure and temperature as input.

B.2.4 *CLIMCAPS-Aqua L2 product*

The CLIMCAPS-Aqua Level 2 product (Community Long-term Infrared Microwave Combined Atmospheric Product System) is based on AIRS spectra and AMSU-A radiances. The processing uses a sophisticated step-wise optimal estimation procedure following the formalism of Rodgers (2000) of various atmospheric quantities such as temperature, moisture, cloud heights and fractions and concentrations of trace gas species O_3, CO, CH_4, CO_2, HNO_3 and SO_2. The retrieval is conducted on about 50 km spatial pixels at nadir (150 km at scan edge). One pixel is referred to as field of regard (FOR) and is made up of 9 (3×3) AIRS field of views (FOVs). The retrieval procedure and a characterisation of retrieval errors are described by Smith and Barnet (2019). In an evaluation of the CLIMCAPS observing capability it is found that CLIMCAPS has sensitivity to multiple narrow tropospheric layers in temperature and humidity, a promising premise for our study (Smith and Barnet, 2020).

We limit our use of available CLIMCAPS variables to the retrieved surface temperature, temperature and humidity profiles, the total cloud fraction, the geopotential height and the respective quality control flags and error estimates. Temperature profiles are provided

on 100 fixed vertical pressure levels from the surface to the top of atmosphere, specific humidity on 66 levels from the surface to about 50 hPa. Since surface pressure is not a retrieval quantity and instead MERRA2 reanalysis surface pressures are used as input to the retrieval, we calculate surface values of humidity following the boundary layer adjustment procedure that is described in the CLIMCAPS science application guide (Smith et al., 2021). Surface values of humidity are important for our method of analysing moisture anomaly characteristics that is described in Sect. B.4.

The quality control flags are provided for each variable on all vertical levels. They subdivide the retrieval into "Best", "Good" and "Rejected" quality. We filter cases where the specific humidity quality control flag of the level closest to MERRA2 surface pressure is labeled "Rejected" and cases with more than 10 "Rejected" vertical levels in humidity between 900to to 100 hPa. These criteria are quite stringent as they filter about 90 % of the data. However, we do not aim to analyse data that is already flagged as being of deficient quality.

A significant difference between the IASI L2 product and the CLIMCAPS product lies in the estimation of the total cloud fraction and the way cloudy scenes are handled. While for the IASI L2 product, cloud fraction is estimated based on an independent instrument (AVHRR), CLIMCAPS estimates cloud fraction based on a subset of cloud sensitive AIRS channels. CLIMCAPS does so for each AIRS FOV and provides a derived FOR-integrated total cloud fraction, i.e. over 3×3 FOVs. To retrieve atmospheric quantities in cloudy conditions the CLIMCAPS and IASI retrieval products deploy conceptually different methods. While the IASI product attempts retrieval through the cloud, CLIMCAPS deploys a cloud clearing technique where information from the 3×3 AIRS FOV spectra are combined to represent the atmospheric state around the clouds throughout the total retrieval FOR. We specifically compare the retrievals' capabilities to resolve vertical moisture structures in all-sky and clear-sky conditions in Sect. B.5.1 and B.5.2.

B.2.5 *Collocation procedure*

We collocate the datasets pairwise in space and time to assure direct comparability of the investigated scenes. This is done using a collocation toolkit that is freely available as part of the "typhon" collection of Python functions for atmospheric science (`https://www.radiativetransfer.org/tools/`).

We conduct the collocation for four dataset pairs, namely ERA5/GRUAN, IASI/GRUAN, IASI/ERA5 and CLIMCAPS/ERA5. With GRUAN being the gold standard reference dataset, we use it as reference where sufficient collocations are available. The standard launch times at 12 UTC am/pm in conjunction with a local time difference on Manus of

UTC+10 h yield launches at local times of about 10 am/pm, matching up well with the IASI equator crossing time of about 09:30 am/pm. Unfortunately for the AIRS based CLIMCAPS retrieval, there is a systematic offset in GRUAN radiosonde launch time and the equator crossing time of the Aqua satellite at around 01:30 am/pm, yielding almost no collocations between GRUAN and CLIMCAPS. However, since we find ERA5 to represent EMLs reasonably well (see Sect. B.5.1), we use ERA5 as a reference for CLIMCAPS and as an additional reference for IASI.

As spatial and temporal collocation criteria we use 50 km and 30 minutes. These criteria are rather conservative since the EMLs of interest are meso-scale phenomena that can extend horizontally over several hundred kilometers and have lifetimes of about a day. The temporal criterion of 30 minutes is also chosen due to the expected 30 minute offset of IASI overpasses and regular radiosonde launches. In addition, 30 minutes assures temporal collocation with ERA5, which has hourly sampling. Since the spatial resolution of ERA5 is higher than the spatial collocation criterion of 50 km we usually find multiple pixels of ERA5 to matchup with another dataset. In these cases, we randomly select one of the matching pixels to assure that datapoints are only used once.

Applying these collocation criteria and the dataset specific filtering criteria described above we obtain 1921 ERA5/GRUAN collocations, 648 IASI/GRUAN collocations, 37491 IASI/ERA5 collocations and 2500 AIRS/ERA5 collocations.

B.3 CLIMATOLOGICAL MEAN

To get a first overview of the vertical structure of humidity and temperature in the vicinity of Manus Island and possible biases between the different datasets we take a look at the mean profiles over the four years of available data. Fig. B.2 shows (a) water vapor volume mixing ratio (H_2O VMR), (b) relative humidity (RH), (c) the deviation of potential temperature (Θ) from a moist adiabat and (d) the static stability calculated as

$$s = -\frac{T}{\Theta}\frac{d\Theta}{dp} \tag{B.1}$$

Higher values in s correspond to a more stable stratification.

Since all datasets can be collocated with ERA5 data, we base the analysis of the mean profiles on the collocation datasets with reference to ERA5 to assure good comparability. This leaves us with three different subsets of ERA5 data that collocate with the other respective data products. We investigated how the mean profiles of ERA5 vary among these subsets and find the variation to not be significant compared to differences between the data products (not shown). Hence,

for the ERA5 mean profiles depicted in Fig. B.2, we choose the collocations with reference to IASI since they contain the most cases.

The mean vertical humidity structure depicted in Fig. B.2a+b shows the typical moist conditions throughout the troposphere that are expected in a deep convective region. RH values rarely drop below 70 % in any of the datasets. A trimodal vertical RH structure is apparent in all datasets with maxima near the surface, in the mid-troposphere and near the tropopause. This vertical structure is in line with previous studies of the vertical distribution of humidity, clouds and detrainment in the ITCZ region (Johnson et al., 1996, 1999; Mapes and Zuidema, 1996; Posselt et al., 2008; Romps, 2014). Here, we target the mid-tropospheric humidity structure as the primary research object, where the presence of an RH maximum highlights the climatological significance of EMLs in our research region.

Comparing the mean RH profiles of the different datasets, the particular good agreement of ERA5 and IASI sticks out. Since the IASI L2 retrieval is trained based on ERA5 data, it is not surprising that the means of the two datasets are so similar. The additional good agreement with GRUAN shows that the datasets are not only self-consistent but also close to reference data. However, good agreement in the mean is not indicative of the datasets' capability to resolve vertical moisture variability, which we investigate seperately in Sect. B.5.1.

AIRS on the other side shows significant biases in RH against the other three datasets. The mid-tropospheric peak in RH is shifted towards a significantly lower altitude while the lower RH peak of the boundary layer is shifted a bit upwards. This yields a moist bias of AIRS between about 600 to 800 hPa. In the upper troposphere, a dry bias is observed. Taking the plots of H_2O VMR (Fig. B.2a) and Θ (Fig. B.2b) into consideration, the mid-tropospheric bias in RH can be attributed to both a positive bias in humidity and a negative bias in temperature. The upper tropospheric dry bias in RH is mostly caused by a bias in humidity since Θ shows no clear bias against the other three datasets in the upper troposphere. AIRS also shows some unphysical RH and Θ variability in the upper troposphere. This is particularly apparent in static stability since vertical gradients associated with this variability are strong between vertical levels. We suggest that this variability may be caused by a numerical artifact that is described in the CLIMCAPS science application guide (Smith et al., 2021). There, the authors find an unphysical zigzag pattern in the temperature profile retrieval error that increases in magnitude with height and they attribute this pattern to their employed data compression methods.

We highlight differences in the vertical structure of potential temperature Θ between the datasets by subtracting a moist adiabat (Fig. B.2c). We adopt this methodology of comparing the tropical vertical temperature structure across different datasets from Keil et al. (2021),

who applied this to CMIP6 data, ERA5 and long-term tropical radiosonde data. It offers an interesting view since the moist adiabat estimates the thermal structure in the tropics set by moist convection quite well. As a difference to Keil et al. (2021), we subtract the same moist adiabat from all datasets and initiate it at the 800 hPa level of the GRUAN mean Θ profile instead of 700 hPa. This allows for a better assessment of biases between the datasets and a comparison at lower levels at the cost of losing some ability to assess the profiles' resemblance of a moist adiabat, which is fine for our purpose.

We find similar vertical structures in $\Theta - \Theta_{\text{moist}}$ as Keil et al. (2021) in their radiosonde and ERA5 results with negative deviations throughout the free troposphere and strongly increasing positive deviations towards the tropopause. We also reproduce the vertical bias structure between ERA5 and radiosonde data of Keil et al. (2021) with almost no bias up to 550 hPa and then an increase to an almost constant 0.6 K bias up to the tropopause. Taking a look at the static stability profiles (Fig. B.2d) of ERA5 and GRUAN we see that they are in good agreement, except for a distinct increase in stability of ERA5 around 550 hPa, which is not present in the radiosonde data and causes the bias in Θ of the two datasets aloft. The stability bump found in ERA5 at this level appears plausible due to diabatic cooling associated with melting of ice particles at this level. As outlined in Sect. B.1, previous studies showed that preferred detrainment of moist air from deep convection due to increased stability near the melting level are what causes the mid-tropospheric humidity peak beneath the stable layer (Johnson et al., 1996; Stevens et al., 2017; Villiger et al., 2022). Hence, it is surprising to find the stable layer at 550 hPa less pronounced in GRUAN than in the ERA5 data. The IASI L2 retrieval shows a slightly increased stability around 550 hPa compared to the radiosonde data, but not as strong of a bump as ERA5. On the other side, the AIRS CLIMCAPS retrieval shows a significant stability increase at around 650 hPa, which coincides with the lower mid-tropospheric RH maximum compared to the other datasets.

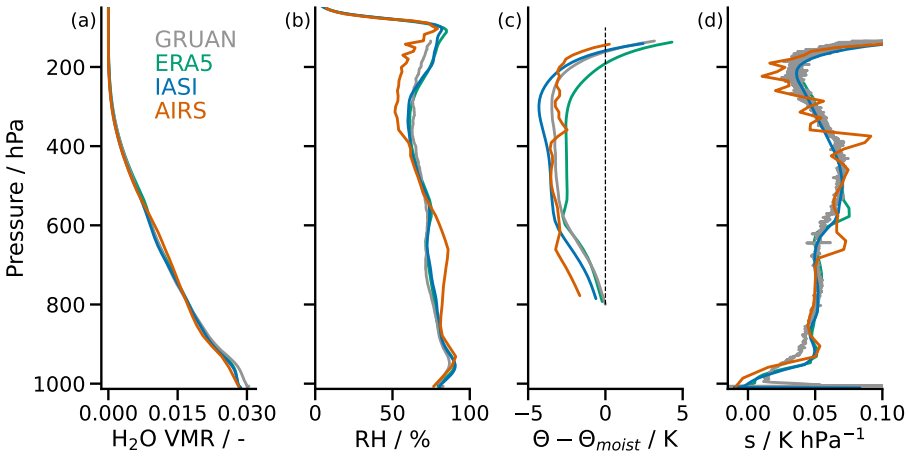

Figure B.2: Mean profiles of (a) H_2O volume mixing ratio (VMR), (b) relative humidity (RH), (c) deviation of potential temperature (Θ) from moist adiabat (Θ_{moist}) based on mean Θ at 700 hPa of GRUAN data and (d) the static stability s in the vicinity of Manus Island based on the four investigated datasets. Only collocated data with ERA5 is used. For the ERA5 profiles, collocated data with IASI is used.

B.4 MOISTURE ANOMALY IDENTIFICATION AND CHARACTERISATION

To assess vertical humidity structures in different datasets, comparing their mean profiles only gives limited information. Positive and negative anomalies can average out and sharp gradients are smoothed. Hence, we assess the representation of Elevated Moist Layers (EMLs) by identifying them in each dataset and characterising them on a case-by-case basis. We do so through metrics that describe the moist layer strength, vertical thickness and height. Quantifying these properties of vertical moisture structures in the different datasets before applying averaging operators yields more targeted information about vertical moisture variability than averaging directly.

Besides the moisture characteristics described above, we also link the moist layers to their impact on the radiative heating rate (Fig. B.3b), where local maxima in cooling are found at the positions of the moist layers. We calculate longwave radiative heating rates with the radiative transfer model RRTMG (Rapid Radiative Transfer Model for GCMs, Mlawer et al., 1997) through its implementation in the radiative convective equilibrium model *konrad* (Kluft and Dacie, 2020). The strong cooling of the moist layers can be translated into locally increased subsidence rates, which we quantify through the radiatively driven vertical velocity

$$\omega_{rad} = -\frac{Q}{s} \tag{B.2}$$

where s is the static stability defined in Eq. B.1. Since s stands in the denominator of ω_{rad} and fluctuates strongly on small vertical scales about values near zero, ω_{rad} also fluctuates strongly. To distill out the radiatively driven dynamical effects in Fig. B.3 on the vertical scale of the moist layers, we apply an evenly weighted 500 m moving average to s and Q and calculate ω_{rad} based on the smoothed profiles. This way, local maxima are clearly visible in ω_{rad} in the identified moist laysers. It is also apparent that the static stability within the moist layer is a key contributing factor for the magnitude of subsidence. Although the upper tropospheric moist layer is associated with weaker radiative cooling than the mid-tropospheric one, the lower stability in the upper tropospheric moist layer results in a stronger subsidence rate.

By calculating moist-layer-associated heating rates, static stabilities and ω_{rad} we estimate the dynamical effect of moist layers in the different datasets and characterise possible differences in Sect. B.6.

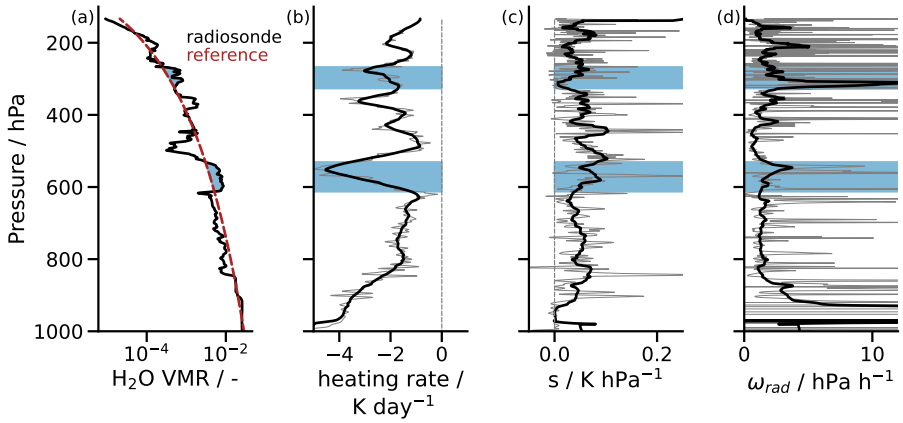

Figure B.3: GRUAN sounding from 2012-15-02 at 12 UTC of (a) H_2O volume mixing ratio (VMR), (b) longwave heating rate, (c) static stability and (d) radiatively driven vertical velocity. The dashed red line in (a) is the reference humidity profile against which moisture anomalies are identified, which are highlighted by blue shaded regions. Thin gray lines in (b), (c) and (d) indicate raw data and thick lines 500 m moving averages.

B.5 COMPARISON OF MOISTURE ANOMALY CHARACTERISTICS

We compare the distributions of moisture anomaly characteristics for the four collocation pairs. To start off, the comparison is based on all-sky scenes. In a next step, we distinguish clear-sky from cloudy cases to assess whether cloudiness affects the datasets' capability of capturing moisture anomalies. This is of particular interest for the satellite retrieval datasets, which employ different cloud handling schemes as described in Sect. B.2.

B.5.1 *All-sky*

The moisture anomaly identification and characterisation method introduced in Sect. B.4 is applied to the humidity profiles of the four collocation datasets. Fig. B.4 shows the resulting distributions of moisture anomaly characteristics for the four collocation pairs. In the following, we discuss what these results tell us about the different datasets' ability to capture EMLs. We start off with ERA5, then go to IASI and finally to AIRS.

As a first indicator of a dataset's ability to capture moisture anomalies, we compare the number of detected moisture anomalies to the reference dataset, i.e. the areas under the distributions depicted in Fig. B.4. ERA5 captures about 99 % as many anomalies as collocated GRUAN data, indicating a good amount of vertical water vapor variability in ERA5 (Fig. B.4, first row). Moisture anomalies in ERA5 are about 50 % weaker and 28 % thicker than moisture anomalies in the collocated GRUAN dataset. Moist layers that are less than 2 km in thickness are particularly underrepresented by ERA5 while moist layers with thickness > 3 km occur more often. These biases suggest that ERA5 is subject to some degree of smoothing due to limited vertical resolution, which we quantify in the following.

To investigate to what extent smoothing alone can explain the biases between the moisture anomaly characteristics of ERA5 and GRUAN, we apply a running mean with vertical window size of 1 km and constant weighting to the GRUAN profiles. The resulting distributions are shown as thick lines in the first row of Fig. B.4. They show that biases in all three moisture anomaly characteristics can mostly be eliminated through the artificial smoothing. This indicates an effective vertical resolution of the ERA5 humidity profiles in the free troposphere of about 1 km. We conclude that ERA5 captures vertical humidity structures on scales of 1 km and greater well as no systematic deviations from the GRUAN distributions are apparent. Hence, we argue that ERA5 is a suitable reference for assessing the satellite retrieval datasets.

We assess the IASI L2 CDR by comparing it to GRUAN data (Fig. B.4, row 2) and ERA5 data (Fig. B.4, row 3). The IASI L2 CDR captures about 75 % as many moisture anomalies as in collocated GRUAN data and about 79 % as many moisture anomalies as in collocated ERA5 data. This is a first indicator that the IASI L2 CDR captures less vertical water vapor variability than ERA5. In addition, the maximum in moisture anomaly thickness at around 2 km altitude detected in both GRUAN and ERA5 data is missing in the IASI L2 CDR. Instead, the anomaly thickness distribution is shifted towards significantly higher values with differences in the means of 85 % against GRUAN and 28 % against ERA5. Moisture anomalies are also significantly weaker in the IASI L2 CDR with mean differences of 53 % and

10 % against GRUAN and ERA5 data, respectively. At this point we want to highlight the added value of assessing the vertical moisture structures of a dataset through moisture characteristics opposed to just comparing the mean profiles (Fig. B.2). While we find a strikingly good agreement of the IASI, ERA5 and GRUAN humidity profiles on the mean, quite significant biases become apparent when applying the moist layer characterisation method and then taking a statistical look at how the resulting metrics compare.

As for ERA5, we investigate whether the found biases in anomaly strength and thickness against GRUAN can be explained by smoothing. We apply a 1 km moving average to the GRUAN profiles collocated with the IASI L2 CDR and obtain the moisture anomaly distributions represented by the thick lines (Fig. B.4, row 2). While the biases in anomaly strength and height against the IASI dataset are significantly reduced, a strong bias remains in the anomaly thickness. We also attempted to increase the smoothing window up to 5 km, but do not find the anomaly thickness distribution to approach the one of the IASI dataset much more (not shown). Hence, the bias in anomaly thickness originates from some other source of error in the IASI dataset than smoothing. We come back to this in the next subsection when concentrating on the clear-sky.

To assess the AIRS CLIMCAPS retrieval, we rely only on ERA5 as a reference as outlined in Sect. B.2.5. The AIRS CLIMCAPS retrieval captures about 92 % as many moisture anomalies as collocated ERA5 data, significantly more than the IASI L2 CDR. Moisture anomalies in the AIRS CLIMCAPS retrieval are on average 26 % stronger and 5 % less thick than those in collocated ERA5 data. Also, moist layers in the AIRS CLIMCAPS retrieval are typically found significantly lower in the troposphere compared to the three other datasets, in particular there are much more moist layer cases below 5 km compared to ERA5. The mean moist layer height is about 1.3 km lower in the AIRS CLIMCAPS retrieval compared to ERA5. We already saw this bias in terms of a shift of the mid-tropospheric humidity peak towards lower altitudes when comparing the dataset mean profiles in Fig. B.2. Moisture anomaly strength is a somewhat height dependent quantity with generally stronger anomalies in the lower troposphere than further up (Prange et al., 2021b). Hence, the increased strength of moist layers in the AIRS CLIMCAPS retrieval is to some degree also caused by a bias in moisture anomaly height. Nonetheless, the number of moisture anomalies in the AIRS CLIMCAPS retrieval speaks towards a good capability of the dataset to capture vertical moisture variability, more so than the IASI L2 CDR.

These findings are coherent with the notion of previous case studies that optimal estimation based retrievals are more capable of capturing vertical moisture structures than regression based retrievals (Calbet et al., 2006; Chazette et al., 2014; Prange et al., 2021a; Smith

and Weisz, 2018; Smith et al., 2012; Weisz et al., 2013; Zhou et al., 2009). A plausible explanation for the superiority of the optimal estimation based AIRS CLIMCAPS retrieval is that capturing EMLs is not sufficiently emphasized in the training of the regression-based IASI retrieval. The fact that the retrieval is trained based on ERA5 data may also set a somewhat upper limit in terms of resolvable vertical structure. The AIRS CLIMCAPS retrieval is constrained by a priori assumptions about mean and variability of the atmospheric state, but if the optimal estimation setup is tweaked well, deviations from the mean state can be captured well with this method.

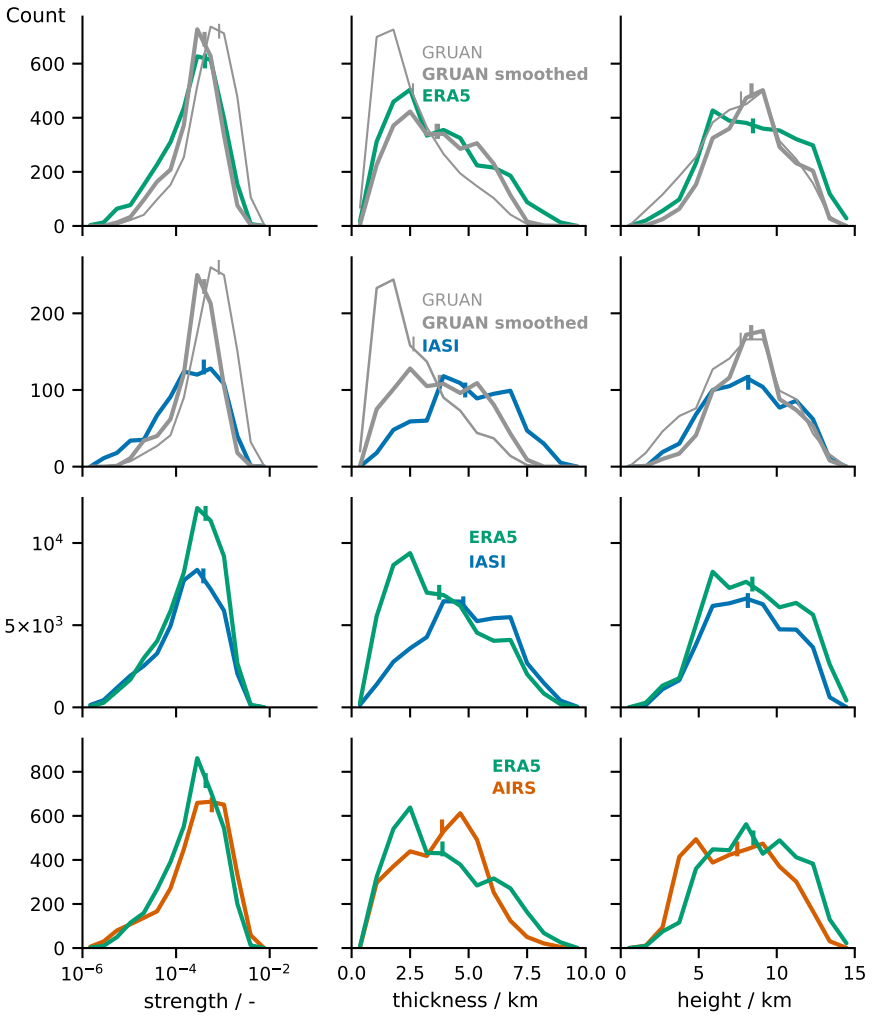

Figure B.4: Distributions of moist layer characteristics (columns) for the four collocation datasets (rows). Moist layer characteristics are defined by Prange et al. (2021b). The thin gray lines refer GRUAN profiles on 10 m vertical resolution while the thick gray lines represent GRUAN profiles with an applied running mean with a 1 km evenly weighed vertical window.

B.5.2 *Clear-sky*

The satellite retrieval products do operate in the presence of clouds, but information content is limited with increased cloudiness and cloud depth, in particular from the infrared instruments. Hence, we are interested whether our analysis of moisture anomaly characteristics yields different results when limited to clear-sky scenes compared to the previously investigated all-sky scenes. Possible differences could then potentially be linked to the different cloud handling schemes deployed by the retrieval products (Sect. B.2).

The AIRS CLIMCAPS and IASI L2 retrievals come with an estimate of total cloud fraction for each retrieval pixel, which are obtained based on quite different methods as outlined in Sect. B.2. ERA5 also provides a total cloud fraction variable, which we show in addition, but do not base our further analysis on since it appears quite biased against the satellite derived cloud fractions. As suggested in the CLIMCAPS science application guide, we use a cloud fraction threshold of 0.2 to distinguish clear-sky from cloudy scenes (Smith et al., 2021). For the two collocation datasets IASI/ERA5 and AIRS/ERA5 this leaves about 22 % of the all-sky amount of data. For the IASI/-GRUAN comparison, sampling becomes too limited, which is why we limit this analysis to the satellite collocations with ERA5.

Fig. B.5 shows the resulting cloud fraction distributions of the two collocation datasets. It is striking that when limiting satellite based cloud fractions to 0.2, ERA5 cloud fraction estimates show maxima near cloud fractions of 1. Without any applied thresholds, both satellite datasets also have their global maxima near cloud fractions of 1 (not shown). However, the secondary maximum near 0 found in both satellite datasets is not at all present in ERA5. We would have expected a stronger bimodality between high and low cloud fractions in ERA5 due to the higher spatial resolution of ERA5 of 31 km compared to about 50 km in the Nadir view of the two satellite products. However, since cloud fraction requires subgrid-scale knowledge it is a difficult to define this variable in a model framework. Hence, finding significant differences to satellite derived estimates is not completely surprising.

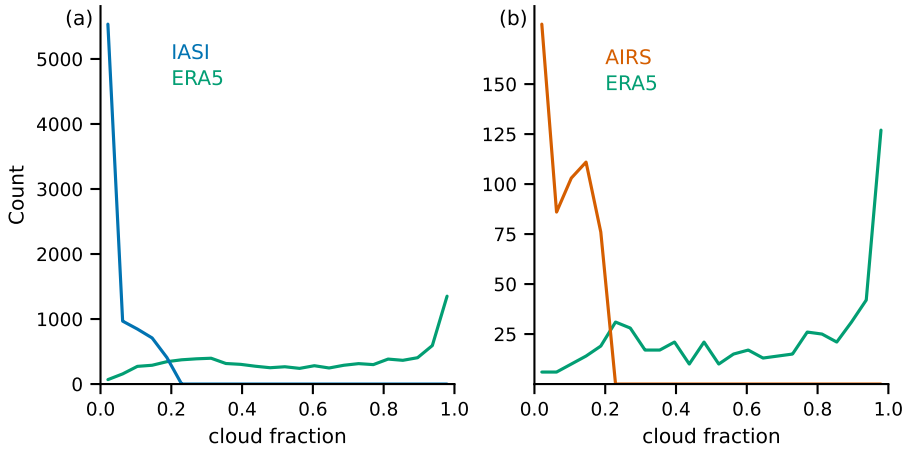

Figure B.5: Cloud fraction distributions of the two collocation datasets (a) IASI/ERA5 and (b) AIRS/ERA5 after applying a cloud fraction threshold of 0.2 based on the IASI and AIRS cloud fraction estimates.

Fig. B.6 shows the resulting moisture anomaly characteristics after application of the clear-sky filter. All datasets consistently show an increase in mean anomaly strength of about 20 % compared to the all-sky results. Note that our method for quantifying anomaly strength is designed to capture the magnitude of vertical moisture variability rather than absolute amount of humidity, which would be highest in case of clouds (Prange et al., 2021b). The found increase in anomaly strength in the clear-sky is in line with our expectations because in cloudy conditions vertical humidity variability is limited by the saturation humidity, leading to weaker moisture anomalies.

We also see a significant change in the shape of the anomaly height distributions when comparing clear-sky to all-sky. IASI and ERA5 both show a clear bimodal structure in anomaly height in the clear-sky, which was not the case in the all-sky data. Physically, we explain the position of the maxima near 5 km and 12 km by levels of preferred detrainment of moist air from mid-level or deep convective plumes into the clear-sky environment (Johnson et al., 1999; Romps, 2014). The mid-level detrainment is thought to be driven by enhanced stability near the melting level and the upper tropospheric detrainment is associated with increased stability towards the tropopause as the atmosphere goes into pure radiative equilibrium aloft. We hypothesize that the mid-tropospheric peak is more pronounced than the upper tropospheric peak in ERA5 and IASI anomaly height distributions because both deep (cumulo nimbuscumulonimbus) and mid-level (cumulus congestus) convection causes mid-level detrainment while only deep convection causes upper level detrainment. AIRS also shows peaks in anomaly height near 5 km and 12 km and another peak inbetween at around 7 km that we can not link to a physical mechanism in this height. However, when interpreting the detailed

shape of the distributions to this extend, we advice caution due to the limited number of AIRS/ERA5 collocations, which is only about 10 % of the number of IASI/ERA5 collocations.

We do not find significant changes in biases between satellite retrievals and ERA5 in anomaly strength or thickness when limiting our data to clear-sky. While we do see changes in the means of the distributions as described above, biases remain similar. Although biases do not change much, we see that the all-sky secondary maximum at large anomaly thickness values of IASI, which is not present in ERA5 (Fig. B.4), vanishes in the clear-sky, indicating better vertical resolution. However, going to clear-sky does not reduce the gap between satellite retrievals and ERA5 at anomaly thickness values below 3 km. We conclude that the retrievals' observing capability of moist layers is not significantly limited by clouds.

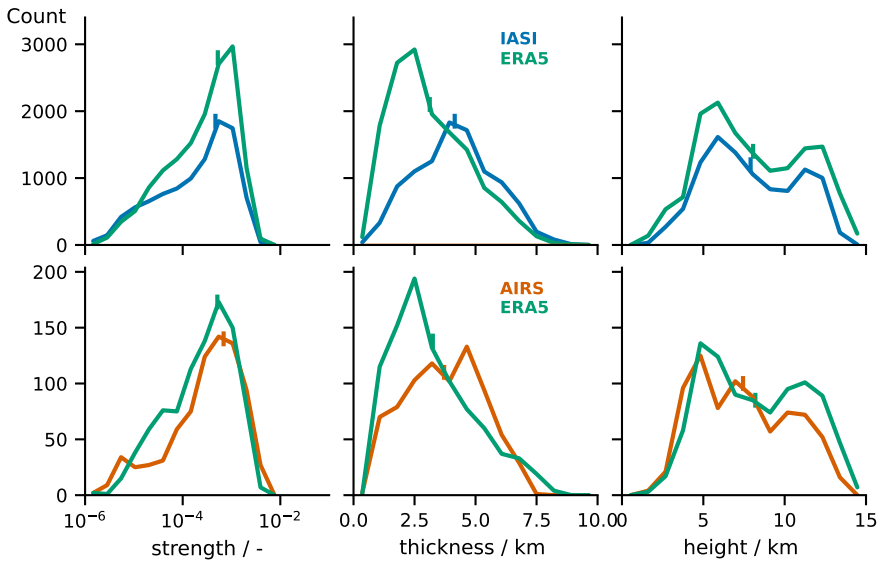

Figure B.6: Same as Fig. B.4 but with cloud fraction < 0.2 in AIRS and IASI datasets. Collocations with reference to GRUAN are omitted due to limited clear-sky sampling. Vertical dashes indicate the means.

B.6 MOIST LAYERS' RADIATIVE IMPLICATIONS ON THE DYNAMICS

In this section we want to translate the datasets' varying capabilites to resolve EMLs found in Sect. B.5.1 into estimates of the moist layers' effect on meso-scale dynamics. EMLs are thought to impact the mesoscale dynamics of the atmosphere through their effect on the spatial structure of radiative heating (Stevens et al., 2017). We attempt to draw a direct connection between EMLs and dynamics by translating their effect on the heating rates into radiatively driven vertical

velocities ω_{rad}, for which to a first order the static stability is another contributing factor (Sect. B.4).

Fig. B.7 shows distributions of moist-layer-associated longwave heating rates, static stabilities (s) and radiatively driven vertical velocities (Eq. B.2). The same moist layers identified as basis for Fig. B.4 are used here and the three additional quantities are calculated for each moist layer. This is done by calculating the vertical median heating rate across each identified moist layer (Fig. B.7, column 1). To calculate the moist layer averaged static stability s according to Eq. B.1, moist layer median temperatures, potential temperatures, and potential temperature gradients are used (Fig. B.7, column 2). The resulting moist-layer-associated heating rates and static stabilities are used to calculate the moist-layer-associated ω_{rad} (Fig. B.7, column 3).

The typical tropical free tropospheric heating rate is on the order of -2 K day^{-1} (Jeevanjee and Fueglistaler, 2020b). Moist-layer-associated heating rates depicted in the first column of Fig. B.7 show their peak at more negative values of around -3 K day^{-1} because of the locally enhanced infrared opacity of the moist layers that cause increased infrared absorption and cooling to space. However, a saddle point in the distributions is found at -2 K day^{-1} that is associated with particularly weak moisture anomalies that barely increase opacity. The fact that most heating rates are found at values lower than -2 K day^{-1} shows that our method does in fact filter for the moisture features we are interested in.

We expect biases in moist-layer-associated heating rates between the collocated datasets to reflect biases in moist layer strength and thickness, i.e. stronger and thinner moist layers go along with more pronounced cooling. We find this to generally be the case as GRUAN shows the strongest moist-layer-associated cooling, followed by only a slight bias to ERA5 and slightly more cooling in the IASI L2 retrieval than in the AIRS CLIMCAPS retrieval. Differences in heating rate distributions between ERA5 and GRUAN are small, indicating that the found biases in moisture anomaly strength and thickness that could mostly be eliminated by applying 1 km vertical smoothing to the radiosonde data are not very significant for the moist-layer-associated heating rates. However, we also find a 19 % difference in the means of static stability between ERA5 and GRUAN that adds to the slightly enhanced cooling in GRUAN to result in a 38 % difference in ω_{rad} means between the two datasets. Static stability values also showed to be increased in ERA5 compared to GRUAN in the comparison of the 4 year mean profiles in Fig. B.2.

For the IASI/GRUAN comparison similar biases are found as for ERA5. The ERA5/IASI comparison reveals that slightly stronger cooling rates found in ERA5 are balanced by slightly increased static stabilities in ERA5 yielding only a 0.7 % difference in ω_{rad} means between ERA5 and IASI.

Stronger biases are found between ERA5 and AIRS. Moist-layer-associated cooling is weakest in the AIRS dataset among all investigated datasets. In addition, AIRS shows significantly enhanced stability with a 44 % mean difference against ERA5, while ERA5 already showed enhanced stability compared to GRUAN. The moist-layer-associated weaker cooling and enhanced stability in AIRS yield a 43 % mean difference in ω_{rad} against ERA5 and an about 80 % mean difference to the GRUAN mean ω_{rad} obtained from collocations with ERA5 and IASI.

To put the found values of ω_{rad} and associated biases between the datasets into some perspective we compare our results to measurements of meso-scale vertical pressure velocities ω obtained from dropsonde measurements of the EUREC^{4}A field campaign. During EUREC^{4}A, the HALO aircraft flew 69 circles of about 200 km diameter launching 12 dropsondes per circle (George et al., 2021b; Konow et al., 2021b). Using the method of Bony and Stevens (2019), circle-integrated profiles of divergence allow for a deduction of ω, some first EUREC^{4}A averaged results of which are presented by Stevens et al. (2021). The campaign mean ranges between values of 1 to 2 hPa hour^{-1} throughout the free troposphere, while individual circles show maximum variations between -5 to 10 hPa hour^{-1}. The moist-layer-associated ω_{rad} values we find based on GRUAN with values between 1.5 to 4 hPa hour^{-1} are generally higher than the mean meso-scale ω measurements. We conclude that EMLs show a significant radiative impact on meso-scale dynamics when compared to meso-scale measurements of ω. With biases of moist-layer-associated ω_{rad} in ERA5, IASI and AIRS data ranging from 38 %to to 80 % compared to GRUAN and ω_{rad} means being on similar order as meso-scale ω measurements we conclude that these datasets have limited usability to assess the dynamical impact of EMLs.

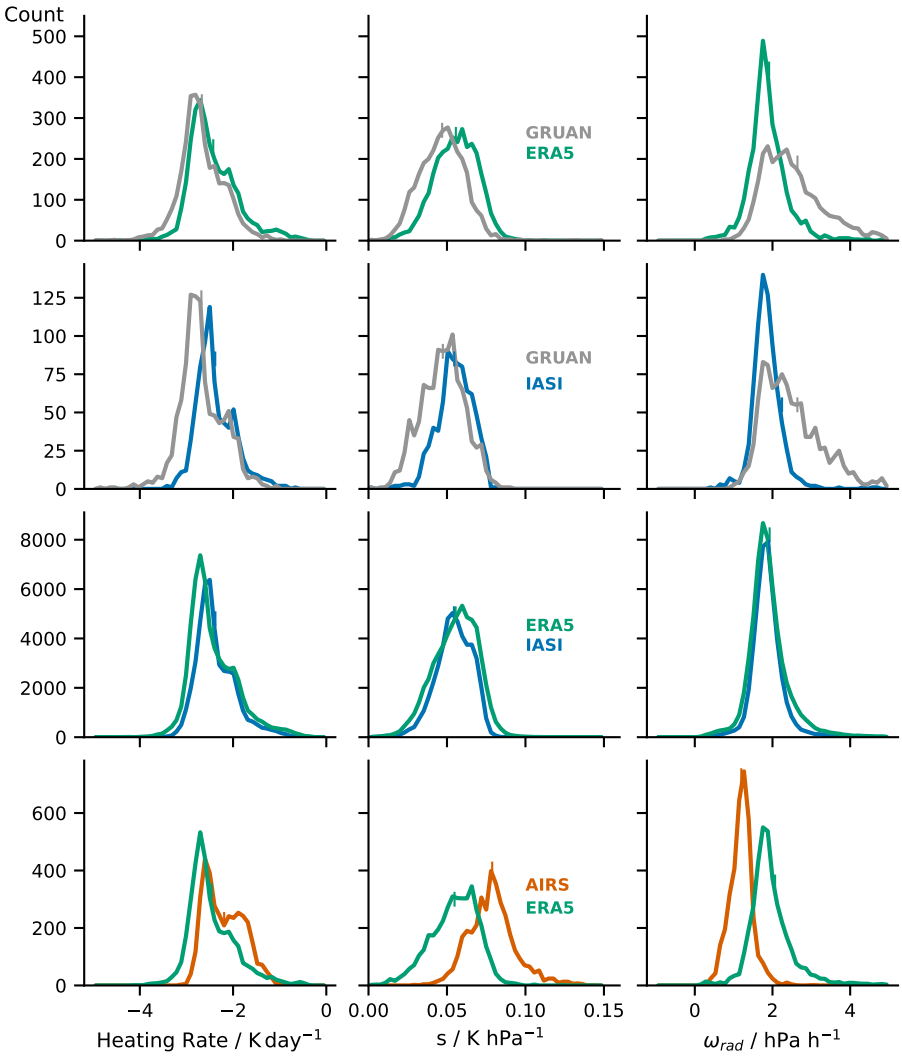

Figure B.7: Distributions of moist-layer-associated longwave heating rate, static stability (s) and radiatively driven vertical velocity ω_{rad} for the different collocation datasets. Averaging measure for heating rate is median. s is calculated based on moist layer median temperature, potential temperature and potential temperature gradient. ω_{rad} is calculated by division of moist-layer-associated heating rate and static stability. Vertical dashes indicate means.

We assessed ERA5 reanalysis data, the IASI Level 2 Climate Data Record (CDR) and the CLIMCAPS-Aqua Level 2 retrieval product in terms of their ability to capture vertical moisture structures, in particular EMLs. As reference, we use 2146 radiosonde soundings from Manus Island of the years 2011 to 2014 that are part of the quality controlled GRUAN network. We compared mean profiles of temperature, humidity and static stability, then identified and characterised collocated moist layers using the method of Prange et al. (2021a) as basis and assessed the moist layers' impact on the dynamics in terms of radiative heating and radiatively driven vertical velocities. In the

following we draw conclusions about our title main question, that is how adequately EMLs are represented in the different data products.

1. The four-year mean profiles show a clear mid-tropospheric maximum in relative humidity in all data products that is associated with EMLs. It is similarly pronounced in ERA5, IASI and GRUAN. Only the AIRS CLIMCAPS retrieval shows significant humidity biases against the other data products. The mid-tropospheric humidity peak is not located near the melting level as in the other datasets, but about 100 hPa lower causing a significant moist bias in the lower to mid free troposphere. A peak in mid-tropospheric static stability is also located about 100 hPa lower than in ERA5. In the upper troposphere between about 400to to 100 hPa the AIRS CLIMCAPS retrieval shows a dry bias against the other datasets.

2. The number of identified moist layers based on the method described in Sect. B.4 is almost equal between collocated ERA5 and GRUAN data, indicating a good amount of vertical water vapor variability in ERA5. Moist layers in ERA5 are about 50 % weaker and 28 % thicker than moist layers in GRUAN data. These biases can be completely negated by applying a 1 km moving average to GRUAN profiles, indicating 1 km effective vertical resolution of ERA5 humidity profiles. The AIRS retrieval shows about 92 % as many moist layers as ERA5 and the IASI retrieval only about 79 %, indicating slightly enhanced vertical moisture variability in the AIRS retrieval compared to IASI. In addition, the IASI retrieval shows about 53 % weaker and 85 % thicker moist layers than collocated GRUAN data. We find that these biases in IASI can not completely be negated by applying vertical smoothing to the GRUAN data, indicating other sources of error than pure smoothing. The AIRS retrieval shows stronger and similarly thick moist layers as ERA5. However, moist layers are generally found about 1.3 km lower in the troposphere than in ERA5, which limits the conclusiveness of comparing moist layer strength, since moist layers further down are typically stronger.

3. Reducing the investigated collocated scenes between the two retrieval datasets and ERA5 to clear-sky is found to not significantly change biases in moist layer strength and thickness, indicating that the cloud handling schemes are not the limiting factors for the retrievals' ability to resolve moist layers. While distributions of total cloud fractions are comparable between the two retrieval datasets, collocated ERA5 total cloud fractions show strong deviations towards cloud fractions of 1 while retrieval cloud fractions are limited to less than 0.2. These biases merit further study.

4. Moist-layer-associated heating rates are on average on the order of -3 K day^{-1}, showing enhanced cooling compared to the mean tropical free tropospheric cooling of about -2 K day^{-1} (Jeevanjee and Fueglistaler, 2020a). Slight biases in moist-layer-associated heating rates are found between the datasets that are representative of the found biases in moist layer strength, thickness and height. Consequently, we find strongest moist-layer-associated cooling in GRUAN data and weakest cooling in the AIRS CLIMCAPS retrieval, which we attribute to its significant bias towards lower moist layer heights where cooling to space is less effective due to the bigger column of water vapor above the moist layers.

5. We find that on average, the moist-layer-associated radiatively driven subsidence ω_{rad} at 1.5 to 4 hPa hour^{-1} is higher than mean meso-scale subsidence deduced from EUREC^{4}A field campaign measurements at about 1 to 2 hPa hour^{-1} (Stevens et al., 2021). Hence, EMLs are relevant for meso-scale atmospheric dynamics. According to Eq. B.2, ω_{rad} is controlled by both moist-layer-associated radiative cooling and static stability. Biases between datasets in both of those quantities are significant for the resulting biases in ω_{rad}, which is 38 % for both ERA5 and IASI with respect to GRUAN and 43 % for the AIRS CLIMCAPS retrieval with respect to ERA5. We conclude that due to these significant relative biases, all datasets have limited usefulness to assess the dynamical impact of EMLs.

Given the inherently limited vertical resolution of reanalysis and retrieval products compared to in-situ soundings, we find ERA5 to resolve EMLs well, while IASI and AIRS show some more significant biases that can not be explained purely by vertical smoothing. The IASI L2 CDR shows most significant biases in moist layer thickness that may be possible to improve by more strongly emphasizing EMLs in the retrieval's training or by introducing an optimal estimation step to the retrieval as for example found by Calbet et al. (2006), the downside of which would be the computational cost. We find the AIRS CLIMCAPS retrieval to be subject to significant humidity biases, in particular with respect to moist layer height. Studying the origins of these biases remains a future task, but we see no inherent reason why it would not be possible to eliminate them.

Data availability The collocation datasets are publically available on Zenodo (Prange et al., 2022b). These include only the data that is used to deduce our results, i.e. after quality control criteria and processing steps as described in Sect. B.2 have been applied.

Author contributions MP conducted the data analysis and prepared the manuscript. SAB and MB supervised the data analysis, contributed ideas to the manuscript and revised it.

Competing interests The authors declare that they have no conflict of interest.

Acknowledgements This work was funded by the German Research Foundation (DFG) in the project 'Elevated Moist Layers – Using HALO during EUREC4A to explore a blind spot in the global satellite observing system', project BU 2253/9-1, part of DFG priority programme HALO SPP 1294, project number 316646266. This work contributes to the Cluster of Excellence Climate, Climatic Change, and Society (CLICCS) and to the Center for Earth System Research and Sustainability (CEN) of Universität Hamburg.

The authors would like to thank the GRUAN community and the Atmospheric Radiation Measurement Program for making the sounding data from Manus Island freely available. The authors would like to thank EUMETSAT for their support in making the analysed IASI L2 CDR available to us. The authors would like to thank the AIRS community for making the analysed CLIMCAPS-Aqua Level 2 dataset freely available for download and providing helpful documentation in their science application guide.

BIBLIOGRAPHY

Ackerman, Thomas P. and Gerald M. Stokes (2003). "The Atmospheric Radiation Measurement Program." In: *Physics Today* 56.1, pp. 38–44. DOI: https://doi.org/10.1063/1.1554135.

Albright, Anna Lea, Benjamin Fildier, Ludovic Touzé-Peiffer, Robert Pincus, Jessica Vial, and Caroline Muller (2020). "Atmospheric radiative profiles during EUREC^{4}A." In: *Earth System Science Data*. DOI: https://doi.org/10.5194/essd-2020-269.

Ananthakrishnan, R. and R. N. Kesavamurthy (1972). "Some new features of the vertical distribution of temperature and humidity over Bombay, during the south-west monsoon season." In: *Journal of the Marine Biological Association of India* 14.2, pp. 732–742. URL: http://mbai.org.in/php/journaldload.php?id=681&bkid=45.

Anderson, G., Shepard Clough, F. Kneizys, J. Chetwynd, and Eric Shettle (May 1986). "AFGL Atmospheric Constituent Profiles (0.120km)." In: p. 46.

Berndt, Emily, Nadia Smith, Jason Burks, Kris White, Rebekah Esmaili, Arunas Kuciauskas, Erika Duran, Roger Allen, Frank LaFontaine, and Jeff Szkodzinski (2020). "Gridded Satellite Sounding Retrievals in Operational Weather Forecasting: Product Description and Emerging Applications." In: *Remote Sensing* 12.20, p. 3311. DOI: https://doi.org/10.3390/rs12203311.

Bony, Sandrine and Bjorn Stevens (2019). "Measuring Area-Averaged Vertical Motions with Dropsondes." In: *Journal of the Atmospheric Sciences* 76.3, pp. 767–783. DOI: 10.1175/JAS-D-18-0141.1.

Bony, Sandrine et al. (2015). "Clouds, circulation and climate sensitivity." In: *Nature Geoscience* 8.4, pp. 261–268. DOI: 10.1038/ngeo2398.

Bony, Sandrine et al. (2017). "EUREC4A: A Field Campaign to Elucidate the Couplings Between Clouds, Convection and Circulation." In: *Surveys in Geophysics* 38.6, pp. 1529–1568. DOI: https://doi.org/10.1007/s10712-017-9428-0.

Borger, Christian, Matthias Schneider, Benjamin Ertl, Frank Hase, Omaira E. García, Michael Sommer, Michael Höpfner, Stephen A. Tjemkes, and Xavier Calbet (2018). "Evaluation of MUSICA IASI tropospheric water vapour profiles using theoretical error assessments and comparisons to GRUAN Vaisala RS92 measurements." In: *Atmospheric Measurement Techniques* 11.9, pp. 4981–5006. DOI: https://doi.org/10.5194/amt-11-4981-2018.

Boukachaba, Niama, Vincent Guidard, and Nadia Fourrié (Sept. 2015). "Land surface temperature retrieval from IASI for assimilation over the AROME-France domain." In.

Brands, S., S. Herrera, J. Fernández, and J. M. Gutiérrez (2013). "How well do CMIP5 Earth System Models simulate present climate conditions in Europe and Africa?" In: *Climate Dynamics* 41.3-4, pp. 803–817. DOI: 10.1007/s00382-013-1742-8.

Buehler, Stefan A., Jana Mendrok, Patrick Eriksson, Agnès Perrin, Richard Larsson, and Oliver Lemke (2018). "ARTS, the Atmospheric Radiative Transfer Simulator – version 2.2, the planetary toolbox edition." In: *Geoscientific Model Development* 11.4, pp. 1537–1556. DOI: https://doi.org/10.5194/gmd-11-1537-2018.

Burgdorf, M. J., S. A. Buehler, and M. Prange (2021). "Calibration and Characterization of Satellite-Borne Microwave Sounders With the Moon." In: *Earth and Space Science* 8.7. DOI: 10.1029/2021EA001725.

Burgdorf, Martin J., Thomas G. Müller, Stefan A. Buehler, Marc Prange, and Manfred Brath (2020). "Characterization of the High-Resolution Infrared Radiation Sounder Using Lunar Observations." In: *Remote Sensing* 12.9, p. 1488. DOI: https://doi.org/10.3390/rs12091488.

Calbet, Xavier, Peter Schlüssel, Tim Hultberg, Pepe Phillips, and Thomas August (2006). "Validation of the operational IASI level 2 processor using AIRS and ECMWF data." In: *Advances in Space Research* 37.12, pp. 2299–2305. DOI: 10.1016/j.asr.2005.07.057.

Cao, Guangxia, Thomas W. Giambelluca, Duane E. Stevens, and Thomas A. Schroeder (2007). "Inversion Variability in the Hawaiian Trade Wind Regime." In: *Journal of Climate* 20.7, pp. 1145–1160. DOI: 10.1175/JCLI4033.1.

Cardinali, Carla (2009). "Monitoring the observation impact on the short-range forecast." In: *Quarterly Journal of the Royal Meteorological Society* 135.638, pp. 239–250. DOI: 10.1002/qj.366.

Chang, Shujie, Zheng Sheng, Huadong Du, Wei Ge, and Wei Zhang (2020). "A channel selection method for hyperspectral atmospheric infrared sounders based on layering." In: *Atmospheric Measurement Techniques* 13.2, pp. 629–644. DOI: https://doi.org/10.5194/amt-13-629-2020.

Chazette, P., F. Marnas, J. Totems, and X. Shang (2014). "Comparison of IASI water vapor retrieval with H&ltsub&gt2&lt/sub&gtO-Raman lidar in the framework of the Mediterranean HyMeX and ChArMEx programs." In: *Atmospheric Chemistry and Physics* 14.18, pp. 9583–9596. DOI: 10.5194/acp-14-9583-2014.

Clerbaux, C. et al. (2009). "Monitoring of atmospheric composition using the thermal infrared IASI/MetOp sounder." In: *Atmospheric Chemistry and Physics* 9.16, pp. 6041–6054. DOI: https://doi.org/10.5194/acp-9-6041-2009.

Collard, A. D. (2007). "Selection of IASI channels for use in numerical weather prediction." In: *Quarterly Journal of the Royal Meteorological Society* 133.629, pp. 1977–1991. DOI: https://doi.org/10.1002/qj.178.

Coppens, Dorothee, Robert Meyer, Dieter Klaes, and Francois Montagner (2019). "IASI Level 1: Product Guide." In: URL: https://www-cdn.eumetsat.int/files/2020-04/pdf_iasi_pg.pdf.

Dahoui, Mohamed, L. Isaksen, and Gabor Radnoti (2017). "Assessing the impact of observations using observation-minus-forecast residuals." In: DOI: 10.21957/51j3sa.

Dingley, Beth, Guy Dagan, and Philip Stier (2021). "Forcing Convection to Aggregate Using Diabatic Heating Perturbations." In: *Journal of Advances in Modeling Earth Systems* 13.10. DOI: 10.1029/2021MS002579.

Dirksen, R. J., M. Sommer, F. J. Immler, D. F. Hurst, R. Kivi, and H. Vömel (2014). "Reference quality upper-air measurements: GRUAN data processing for the Vaisala RS92 radiosonde." In: *Atmospheric Measurement Techniques* 7.12, pp. 4463–4490. DOI: 10.5194/amt-7-4463-2014.

ECMWF (2016). "IFS Documentation CY41R2 - Part III: Dynamics and Numerical Procedures." In: DOI: 10.21957/83wouv80.

ECMWF (2018). "IFS Documentation - Cy45r1." In: ECMWF. Chap. Part IV : Physical processes, p. 203. URL: https://www.ecmwf.int/node/18714.

EUMETSAT (2017). "IASI Level 2: Product Guide." In: URL: https://www.eumetsat.int/media/45982.

EUMETSAT (2022). "IASI All Sky Temperature and Humidity Profiles - Climate Data Record Release 1.1 - Metop-A and -B." en. In: DOI: 10.15770/EUM_SEC_CLM_0063.

Eresmaa, Reima and Anthony McNally (Oct. 2014). *Diverse profile datasets from the ECMWF 137-level short-range forecasts*. DOI: 10.13140/2.1.4476.8963.

Eriksson, P., S.A. Buehler, C.P. Davis, C. Emde, and O. Lemke (2011). "ARTS, the atmospheric radiative transfer simulator, version 2." In: *Journal of Quantitative Spectroscopy and Radiative Transfer* 112.10, pp. 1551–1558. DOI: 10.1016/j.jqsrt.2011.03.001.

Eyring, Veronika, Sandrine Bony, Gerald A. Meehl, Catherine A. Senior, Bjorn Stevens, Ronald J. Stouffer, and Karl E. Taylor (2016). "Overview of the Coupled Model Intercomparison Project Phase 6 (CMIP6) experimental design and organization." In: *Geoscientific Model Development* 9.5, pp. 1937–1958. DOI: https://doi.org/10.5194/gmd-9-1937-2016.

Ferraro, Robert, Duane E. Waliser, Peter Gleckler, Karl E. Taylor, and Veronika Eyring (2015). "Evolving Obs4MIPs to Support Phase 6 of the Coupled Model Intercomparison Project (CMIP6)." In: *Bulletin of the American Meteorological Society* 96.8, ES131–ES133. DOI: 10.1175/BAMS-D-14-00216.1.

Fourrié, Nadia and Florence Rabier (2004). "Cloud characteristics and channel selection for IASI radiances in meteorologically sensitive areas." In: *Quarterly Journal of the Royal Meteorological Society*

130.600, pp. 1839–1856. DOI: https://doi.org/10.1256/qj.03.27.

Fourrié, Nadia and Jean-Noël Thépaut (2003). "Evaluation of the AIRS near-real-time channel selection for application to numerical weather prediction." In: *Quarterly Journal of the Royal Meteorological Society* 129.592, pp. 2425–2439. DOI: https://doi.org/10.1256/qj.02.210.

George, Geet et al. (2021a). "JOANNE: Joint dropsonde Observations of the Atmosphere in tropical North atlaNtic meso-scale Environments." In: *Earth System Science Data* 13.11, pp. 5253–5272. DOI: 10.5194/essd-13-5253-2021.

George, Geet et al. (2021b). "JOANNE: Joint dropsonde Observations of the Atmosphere in tropical North atlaNtic meso-scale Environments." In: *Earth System Science Data* 13.11, pp. 5253–5272. DOI: https://doi.org/10.5194/essd-13-5253-2021.

Gordon, I.E. et al. (2017). "The HITRAN2016 molecular spectroscopic database." In: *Journal of Quantitative Spectroscopy and Radiative Transfer* 203, pp. 3–69. DOI: https://doi.org/10.1016/j.jqsrt.2017.06.038.

Haraguchi, Paul Y. (1968). "Inversions over the tropical eastern pacific ocean." In: *Monthly Weather Review* 96.3, pp. 177 –185. DOI: 10.1175/1520-0493(1968)096<0177:IOTTEP>2.0.CO;2. URL: https://journals.ametsoc.org/view/journals/mwre/96/3/1520-0493_1968_096_0177_iottep_2_0_co_2.xml.

Hariharan, P. (2007). *Basics of Interferometry*. 2nd ed. Elsevier. ISBN: 9780123735898. DOI: https://doi.org/10.1016/B978-0-12-373589-8.X5000-7.

Hersbach, Hans et al. (2020). "The ERA5 global reanalysis." In: *Quarterly Journal of the Royal Meteorological Society* 146.730, pp. 1999–2049. DOI: 10.1002/qj.3803.

Irion, Fredrick W., Brian H. Kahn, Mathias M. Schreier, Eric J. Fetzer, Evan Fishbein, Dejian Fu, Peter Kalmus, R. Chris Wilson, Sun Wong, and Qing Yue (2018). "Single-footprint retrievals of temperature, water vapor and cloud properties from AIRS." In: *Atmospheric Measurement Techniques* 11.2, pp. 971–995. DOI: https://doi.org/10.5194/amt-11-971-2018.

Jeevanjee, Nadir and Stephan Fueglistaler (2020a). "On the Cooling-to-Space Approximation." In: *Journal of the Atmospheric Sciences* 77.2, pp. 465–478. DOI: 10.1175/JAS-D-18-0352.1.

Jeevanjee, Nadir and Stephan Fueglistaler (2020b). "Simple Spectral Models for Atmospheric Radiative Cooling." In: *Journal of the Atmospheric Sciences* 77.2, pp. 479–497. DOI: 10.1175/JAS-D-18-0347.1.

Jiang, Jonathan H. et al. (2012). "Evaluation of cloud and water vapor simulations in CMIP5 climate models using NASA "A-Train"

satellite observations." In: *Journal of Geophysical Research: Atmospheres* 117.D14, n/a–n/a. DOI: 10.1029/2011JD017237.

Johnson, Richard H., Paul E. Ciesielski, and Kenneth A. Hart (1996). "Tropical Inversions near the 0°C Level." In: *Journal of the Atmospheric Sciences* 53.13, pp. 1838–1855. DOI: 10.1175/1520-0469(1996)053<1838:TINTL>2.0.CO;2.

Johnson, Richard H., Thomas M. Rickenbach, Steven A. Rutledge, Paul E. Ciesielski, and Wayne H. Schubert (Aug. 1999). "Trimodal Characteristics of Tropical Convection." In: *Journal of Climate* 12.8, pp. 2397–2418. ISSN: 0894-8755. DOI: 10.1175/1520-0442(1999)012<2397:TCOTC>2.0.CO;2. eprint: https://journals.ametsoc.org/jcli/article-pdf/12/8/2397/3775124/1520-0442(1999)012_2397_tcotc_2_0_co_2.pdf. URL: https://doi.org/10.1175/1520-0442(1999)012<2397:TCOTC>2.0.CO;2.

Keil, P., H. Schmidt, B. Stevens, and J. Bao (2021). "Variations of Tropical Lapse Rates in Climate Models and their Implications for Upper Tropospheric Warming." In: *Journal of Climate*, pp. 1–50. DOI: 10.1175/JCLI-D-21-0196.1.

Kluft, Lukas and Sally Dacie (2020). "atmtools/konrad." In: DOI: http://doi.org/10.5281/zenodo.3899702.

Konow, Heike, Marek Jacob, Felix Ament, Susanne Crewell, Florian Ewald, Martin Hagen, Lutz Hirsch, Friedhelm Jansen, Mario Mech, and Bjorn Stevens (2019). "A unified data set of airborne cloud remote sensing using the HALO Microwave Package (HAMP)." In: *Earth System Science Data* 11.2, pp. 921–934. DOI: https://doi.org/10.5194/essd-11-921-2019.

Konow, Heike et al. (2021a). "EUREC4A's HALO." In: *Earth System Science Data* 13.12, pp. 5545–5563. DOI: 10.5194/essd-13-5545-2021.

Konow, Heike et al. (2021b). "EUREC&ampltsup&ampgt4&amplt/sup&ampgtA's &amplti&ampgtHALO&amplt/i&ampgt." In: *Earth System Science Data* 13.12, pp. 5545–5563. DOI: https://doi.org/10.5194/essd-13-5545-2021.

Lacour, J.-L., C. Risi, L. Clarisse, S. Bony, D. Hurtmans, C. Clerbaux, and P.-F. Coheur (2012). "Mid-tropospheric D observations from IASI/MetOp at high spatial and temporal resolution." In: *Atmospheric Chemistry and Physics* 12.22, pp. 10817–10832. DOI: 10.5194/acp-12-10817-2012.

Lang, Theresa, Ann Kristin Naumann, Bjorn Stevens, and Stefan A. Buehler (2021). "Tropical Free-Tropospheric Humidity Differences and Their Effect on the Clear-Sky Radiation Budget in Global Storm-Resolving Models." In: *Journal of Advances in Modeling Earth Systems* 13.11. DOI: 10.1029/2021MS002514.

Lerner, Jeffrey A. (2002). "Temperature and humidity retrieval from simulated Infrared Atmospheric Sounding Interferometer (IASI)

measurements." In: *Journal of Geophysical Research* 107.D14. DOI: 10.1029/2001JD900254.

Levenberg, Kenneth (1944). "A method for the solution of certain non-linear problems in least squares." In: *Quarterly of Applied Mathematics* 2.2, pp. 164–168. DOI: 10.1090/qam/10666.

Manabe, Syukuro and Richard T. Wetherald (1967). "Thermal Equilibrium of the Atmosphere with a Given Distribution of Relative Humidity." In: *Journal of the Atmospheric Sciences* 24.3, pp. 241–259. DOI: 10.1175/1520-0469(1967)024<0241:TEOTAW>2.0.CO;2.

Mapes, Brain E. and Paquita Zuidema (1996). "Radiative-Dynamical Consequences of Dry Tongues in the Tropical Troposphere." In: *Journal of the Atmospheric Sciences* 53.4, pp. 620–638. DOI: 10.1175/1520-0469(1996)053<0620:RDCODT>2.0.CO;2.

Marquardt, Donald W. (1963). "An Algorithm for Least-Squares Estimation of Nonlinear Parameters." In: *Journal of the Society for Industrial and Applied Mathematics* 11.2, pp. 431–441. DOI: 10.1137/0111030.

Martinet, P., L. Lavanant, N. Fourrié, F. Rabier, and A. Gambacorta (2013). "Evaluation of a revised IASI channel selection for cloudy retrievals with a focus on the Mediterranean basin." In: *Quarterly Journal of the Royal Meteorological Society* 140.682, pp. 1563–1577. DOI: https://doi.org/10.1002/qj.2239.

Matricardi, Marco, Manuel López-Puertas, and Bernd Funke (2018). "Modeling of Nonlocal Thermodynamic Equilibrium Effects in the Classical and Principal Component-Based Version of the RTTOV Fast Radiative Transfer Model." In: *Journal of Geophysical Research: Atmospheres* 123.11, pp. 5741–5761. DOI: https://doi.org/10.1029/2018JD028657.

Mauritsen, Thorsten and Bjorn Stevens (2015). "Missing iris effect as a possible cause of muted hydrological change and high climate sensitivity in models." In: *Nature Geoscience* 8.5, pp. 346–351. DOI: 10.1038/NGEO2414.

Merchant, Christopher J. et al. (2019). "Satellite-based time-series of sea-surface temperature since 1981 for climate applications." In: *Scientific Data* 6.1. DOI: https://doi.org/10.1038/s41597-019-0236-x.

Mlawer, Eli J., Vivienne H. Payne, Jean-Luc Moncet, Jennifer S. Delamere, Matthew J. Alvarado, and David C. Tobin (2012). "Development and recent evaluation of the MT_CKD model of continuum absorption." In: *Philosophical Transactions of the Royal Society A: Mathematical, Physical and Engineering Sciences* 370.1968, pp. 2520–2556. DOI: https://doi.org/10.1098/rsta.2011.0295.

Mlawer, Eli J., Steven J. Taubman, Patrick D. Brown, Michael J. Iacono, and Shepard A. Clough (1997). "Radiative transfer for inhomogeneous atmospheres: RRTM, a validated correlated-k model for the longwave." In: *Journal of Geophysical Research: Atmospheres*

102.D14, pp. 16663–16682. DOI: https://doi.org/10.1029/97JD00237.

Muller, Caroline and Sandrine Bony (2015). "What favors convective aggregation and why?" In: *Geophysical Research Letters* 42.13, pp. 5626–5634. DOI: 10.1002/2015GL064260.

Muller, Caroline et al. (2022). "Spontaneous Aggregation of Convective Storms." In: *Annual Review of Fluid Mechanics* 54.1, pp. 133–157. DOI: https://doi.org/10.1146/annurev-fluid-022421-011319.

Müller, T. G., M. Burgdorf, V. Ali-Lagoa, S. A. Buehler, and M. Prange (2021). "The Moon at thermal infrared wavelengths: a benchmark for asteroid thermal models." In: *Astronomy and Astrophysics* 650, A38. DOI: https://doi.org/10.1051/0004-6361/202039946.

Naumann, Ann Kristin, Bjorn Stevens, and Cathy Hohenegger (2019). "A Moist Conceptual Model for the Boundary Layer Structure and Radiatively Driven Shallow Circulations in the Trades." In: *Journal of the Atmospheric Sciences* 76.5, pp. 1289–1306. DOI: 10.1175/JAS-D-18-0226.1.

Pincus, Robert et al. (2020). "Benchmark Calculations of Radiative Forcing by Greenhouse Gases." In: *Journal of Geophysical Research: Atmospheres* 125.23. DOI: https://doi.org/10.1029/2020JD033483.

Posselt, D. J., S. C. van den Heever, and G. L. Stephens (2008). "Trimodal cloudiness and tropical stable layers in simulations of radiative convective equilibrium." In: *Geophysical Research Letters* 35.8. DOI: https://doi.org/10.1029/2007GL033029.

Prange, Marc, Manfred Brath, and Stefan A. Buehler (2021a). "Are elevated moist layers a blind spot for hyperspectral infrared sounders? A model study." In: *Atmospheric Measurement Techniques* 14.11, pp. 7025–7044. DOI: https://doi.org/10.5194/amt-14-7025-2021.

Prange, Marc, Manfred Brath, and Stefan Alexander Buehler (2021b). "Supplementary data for "Are elevated moist layers a blind spot for hyperspectral infrared sounders? - a model study"." en. In: DOI: 10.5281/zenodo.4501184.

Prange, Marc, Stefan A. Buehler, and Manfred Brath (2022a). "How adequately are elevated moist layers represented in reanalysis and satellite observations?" In: *Atmospheric Chemistry and Physics*. DOI: https://doi.org/10.5194/egusphere-2022-755.

Prange, Marc, Stefan A. Buehler, and Manfred Brath (2022b). "Supplementary data for "How adequately are elevated moist layers represented in reanalysis and satellite observations?"" en. In: DOI: 10.5281/zenodo.6940500.

Prange, Marc, Max Ringel, Geet George, Lutz Hirsch, Tobias Kölling, Heike Konow, Theresa Lang, and Theresa Mieslinger (2020). "EUREC4A: HALO flight phase separation: Awesome Albatross." en. In: DOI: 10.5281/zenodo.3906507.

Razavi, A., C. Clerbaux, C. Wespes, L. Clarisse, D. Hurtmans, S. Payan, C. Camy-Peyret, and P. F. Coheur (2009). "Characterization of methane retrievals from the IASI space-borne sounder." In: *Atmospheric Chemistry and Physics* 9.20, pp. 7889–7899. DOI: https://doi.org/10.5194/acp-9-7889-2009.

Rodgers, Clive D (2000). "Inverse Methods for Atmospheric Sounding." In: *Oceanic and Planetary Physics* 2. DOI: https://doi.org/10.1142/3171.

Romps, David M. (2014). "An Analytical Model for Tropical Relative Humidity." In: *Journal of Climate* 27.19, pp. 7432–7449. DOI: https://doi.org/10.1175/JCLI-D-14-00255.1.

Schmidt, Gavin A., Reto A. Ruedy, Ron L. Miller, and Andy A. Lacis (2010). "Attribution of the present-day total greenhouse effect." In: *Journal of Geophysical Research* 115.D20. DOI: doi:10.1029/2010JD014287.

Schneider, M. and F. Hase (2011). "Optimal estimation of tropospheric H2O and &deltaD with IASI/METOP." In: *Atmospheric Chemistry and Physics* 11.21, pp. 11207–11220. DOI: 10.5194/acp-11-11207-2011.

Schulz, Hauke, Ryan Eastman, and Bjorn Stevens (2021). "Characterization and Evolution of Organized Shallow Convection in the Downstream North Atlantic Trades." In: *Journal of Geophysical Research: Atmospheres* 126.17. DOI: https://doi.org/10.1029/2021JD034575.

Schulz, Hauke and Bjorn Stevens (2018). "Observing the Tropical Atmosphere in Moisture Space." In: *Journal of the Atmospheric Sciences* 75.10, pp. 3313–3330. DOI: 10.1175/JAS-D-17-0375.1.

Seidel, Dian J. et al. (2009). "Reference Upper-Air Observations for Climate: Rationale, Progress, and Plans." In: *Bulletin of the American Meteorological Society* 90.3, pp. 361–369. DOI: https://doi.org/10.1175/2008BAMS2540.1.

Sherwood, S. C. et al. (2020). "An Assessment of Earth's Climate Sensitivity Using Multiple Lines of Evidence." In: *Reviews of Geophysics* 58.4. DOI: https://doi.org/10.1029/2019RG000678.

Smith, Nadia and Christopher D. Barnet (2019). "Uncertainty Characterization and Propagation in the Community Long-Term Infrared Microwave Combined Atmospheric Product System (CLIMCAPS)." In: *Remote Sensing* 11.10, p. 1227. DOI: https://doi.org/10.3390/rs11101227.

Smith, Nadia and Christopher D. Barnet (2020). "CLIMCAPS observing capability for temperature, moisture, and trace gases from AIRS/AMSU and CrIS/ATMS." In: *Atmospheric Measurement Techniques* 13.8, pp. 4437–4459. DOI: https://doi.org/10.5194/amt-13-4437-2020.

Smith, Nadia, Rebekah Esmaili, and Chris D. Barnet (2021). "Community Long-term Infrared Microwave CombinedAtmospheric

Product System (CLIMCAPS) Science Application Guides." In: URL: https://docserver.gesdisc.eosdis.nasa.gov/public/project/Sounder/CLIMCAPS_V2_L2_science_guides.pdf.

Smith, W.L. and E. Weisz (2018). "Dual-Regression Approach for High-Spatial-Resolution Infrared Soundings." In: pp. 297–311. DOI: https://doi.org/10.1016/B978-0-12-409548-9.10394-X.

Smith, William L., Elisabeth Weisz, Stanislav V. Kireev, Daniel K. Zhou, Zhenglong Li, and Eva E. Borbas (2012). "Dual-Regression Retrieval Algorithm for Real-Time Processing of Satellite Ultraspectral Radiances." In: *Journal of Applied Meteorology and Climatology* 51.8, pp. 1455–1476. DOI: 10.1175/JAMC-D-11-0173.1.

Sobel, Adam H. and Christopher S. Bretherton (Dec. 2000). "Modeling Tropical Precipitation in a Single Column." In: *Journal of Climate* 13.24, pp. 4378–4392. ISSN: 0894-8755. DOI: 10.1175/1520-0442(2000)013<4378:MTPIAS>2.0.CO;2. eprint: https://journals.ametsoc.org/jcli/article-pdf/13/24/4378/3766524/1520-0442(2000)013_4378_mtpias_2_0_co_2.pdf. URL: https://doi.org/10.1175/1520-0442(2000)013<4378:MTPIAS>2.0.CO;2.

Stevens, B. et al. (2021). "EUREC^{4}A." In: *Earth System Science Data Discussions* 2021, pp. 1–78. DOI: 10.5194/essd-2021-18. URL: https://essd.copernicus.org/preprints/essd-2021-18/.

Stevens, Bjorn, Hélène Brogniez, Christoph Kiemle, Jean-Lionel Lacour, Cyril Crevoisier, and Johannes Kiliani (2017). "Structure and Dynamical Influence of Water Vapor in the Lower Tropical Troposphere." In: *Surveys in Geophysics* 38.6, pp. 1371–1397. DOI: https://doi.org/10.1007/s10712-017-9420-8.

Susskind, Joel, John M. Blaisdell, and Lena Iredell (2014). "Improved methodology for surface and atmospheric soundings, error estimates, and quality control procedures: the atmospheric infrared sounder science team version-6 retrieval algorithm." In: *Journal of Applied Remote Sensing* 8.1, p. 084994. DOI: https://doi.org/10.1117/1.JRS.8.084994.

Sussmann, R. and T. Borsdorff (2007). "Technical Note: Interference errors in infrared remote sounding of the atmosphere." In: *Atmospheric Chemistry and Physics* 7.13, pp. 3537–3557. DOI: 10.5194/acp-7-3537-2007.

Teixeira, Joao, Duane Waliser, Robert Ferraro, Peter Gleckler, Tsengdar Lee, and Gerald Potter (2014). "Satellite Observations for CMIP5: The Genesis of Obs4MIPs." In: *Bulletin of the American Meteorological Society* 95.9, pp. 1329–1334. DOI: 10.1175/BAMS-D-12-00204.1.

Villiger, Leonie, Heini Wernli, Maxi Boettcher, Martin Hagen, and Franziska Aemisegger (2022). "Lagrangian formation pathways of moist anomalies in the trade-wind region during the dry season: two case studies from EUREC&ltsup&gt4&lt/sup&gtA." In:

Weather and Climate Dynamics 3.1, pp. 59–88. DOI: 10.5194/wcd-3-59-2022.

Weisz, Elisabeth, William L. Smith, and Nadia Smith (2013). "Advances in simultaneous atmospheric profile and cloud parameter regression based retrieval from high-spectral resolution radiance measurements." In: *Journal of Geophysical Research: Atmospheres* 118.12, pp. 6433–6443. DOI: 10.1002/jgrd.50521.

Wing, Allison A., Kerry Emanuel, Christopher E. Holloway, and Caroline Muller (2017). "Convective Self-Aggregation in Numerical Simulations: A Review." In: *Surveys in Geophysics* 38.6, pp. 1173–1197. DOI: https://doi.org/10.1007/s10712-017-9408-4.

Wing, Allison A. et al. (2020). "Clouds and Convective Self-Aggregation in a Multimodel Ensemble of Radiative-Convective Equilibrium Simulations." In: *Journal of Advances in Modeling Earth Systems* 12.9. DOI: https://doi.org/10.1029/2020MS002138.

Yoneyama, Kunio, Chidong Zhang, and Charles N. Long (2013). "Tracking Pulses of the Madden–Julian Oscillation." In: *Bulletin of the American Meteorological Society* 94.12, pp. 1871–1891. DOI: https://doi.org/10.1175/BAMS-D-12-00157.1.

Zelinka, Mark D., David A. Randall, Mark J. Webb, and Stephen A. Klein (2017). "Clearing clouds of uncertainty." In: *Nature Climate Change* 7.10, pp. 674–678. DOI: https://doi.org/10.1038/nclimate3402.

Zhou, D. K., W. L. Smith, A. M. Larar, X. Liu, J. P. Taylor, P. Schlüssel, L. L. Strow, and S. A. Mango (2009). "All weather IASI single field-of-view retrievals: case study – validation with JAIVEx data." In: *Atmospheric Chemistry and Physics* 9.6, pp. 2241–2255. DOI: https://doi.org/10.5194/acp-9-2241-2009.

Zuidema, Paquita (June 1998). "The 600–800-mb Minimum in Tropical Cloudiness Observed during TOGA COARE." In: *Journal of the Atmospheric Sciences* 55.12, pp. 2220–2228. ISSN: 0022-4928. DOI: 10.1175/1520-0469(1998)055<2220:TMMITC>2.0.CO;2. eprint: https://journals.ametsoc.org/jas/article-pdf/55/12/2220/3433626/1520-0469(1998)055_2220_tmmitc_2_0_co_2.pdf. URL: https://doi.org/10.1175/1520-0469(1998)055<2220:TMMITC>2.0.CO;2.

DECLARATION

Hiermit erkläre ich an Eides statt, dass ich die vorliegende Dissertationsschrift selbst verfasst und keine anderen als die angegebenen Quellen und Hilfsmittel benutzt habe.

Hamburg, den 11.10.2022

Marc Prange